

**HIGH TEMPERATURE, PERMANENT MAGNET BIASED,
MAGNETIC BEARINGS**

A Thesis

by

VARUN RAJESH GANDHI

Submitted to the Office of Graduate Studies of
Texas A&M University
in partial fulfillment of the requirements for the degree of

MASTER OF SCIENCE

May 2009

Major Subject: Mechanical Engineering

**HIGH TEMPERATURE, PERMANENT MAGNET BIASED,
MAGNETIC BEARINGS**

A Thesis

by

VARUN RAJESH GANDHI

Submitted to the Office of Graduate Studies of
Texas A&M University
in partial fulfillment of the requirements for the degree of

MASTER OF SCIENCE

Approved by:

Chair of Committee,	Alan B. Palazzolo
Committee Members,	Bryan P. Rasmussen
	Srinivas Vadali
Head of Department,	Dennis O'Neal

May 2009

Major Subject: Mechanical Engineering

ABSTRACT

High Temperature, Permanent Magnet Biased, Magnetic Bearings. (May 2009)

Varun Rajesh Gandhi, B.E., Rashtriya Vidyalaya College of Engineering

Chair of Advisory Committee: Dr. Alan B. Palazzolo

The Electron Energy Corporation (EEC) along with the National Aeronautics and Space Administration (NASA) is researching magnetic bearings. The purpose of this research was to design and develop a high-temperature (1000°F) magnetic bearing system using High Temperature Permanent Magnets (HTPM), developed by the EEC. The entire system consisted of two radial bearings, one thrust bearing, one motor and 2 sets of catcher bearings.

This high temperature magnetic bearing system will be used in high performance, high speed and high temperature applications like space vehicles, jet engines and deep sea equipment. The bearing system had a target design to carry a load equal to 500 lb-f (2225N). Another objective was to design and build a test rig fixture to measure the load capacity of the designed high temperature radial magnetic bearing (HTRMB) called Radial Bearing Force Test Rig (RBFTR).

A novel feature of this high temperature magnetic bearing is its homopolar construction which incorporates state of the art high temperature, 1000 °F, permanent magnets. A second feature is its fault tolerance capability which provides the desired control forces even if half the coils have failed.

The permanent magnet bias of the radial magnetic bearing reduces the amount of current required for magnetic bearing operation. This reduces the power loss due to the coil current resistance and also increases the system efficiency because magnetic field of the HTPM is used to take up the major portion of the static load on the bearing. The bias flux of the homopolar radial bearing is produced by the EEC HTPM to reduce the related ohmic losses of an electromagnetic circuit significantly.

An experimental procedure was developed using the Radial Bearing Force Test Rig (RBTFR) to measure actual load capacity of the designed bearing at the test rig. All the results obtained from the experiment were compiled and analyzed to determine the relation between bearing force, applied current and temperature.

DEDICATION

To my grandparents

ACKNOWLEDGEMENTS

I would like to express my deepest gratitude to my committee chair Dr. Alan B. Palazzolo for his enthusiasm, encouragement and patience throughout the course of my research. I would also like to thank Dr. Bryan P. Rasmussen and Dr. Srinivas Vadali for being on my thesis committee and their support.

Special thanks go to Mr. Randall Tucker for his guidance in getting the test rig together and for the 3D solid model of the test rig concept. Thanks are extended to Kyungdae Kang, Junyoung Park, Zhengxin Zhang, Zhiyang Wang, Shawn Hagler and others who shared time with me in the Vibration Control and Electromechanics Laboratory and for their patience and help. I would also like to thank Mr. Andrew Provenza of NASA Glenn Research Center for the design specifications, Dr. Andrew Kenny for the 3D magnetic field simulation of the bearings, Dr. Jinfang Liu and Dr. Heeju Choi from the Electron Energy Corporation (EEC) for providing the permanent magnets and support in this project.

Thanks also go to my friends and colleagues and the department faculty and staff for making my time at Texas A&M University a great experience. Finally, thanks to my mother and father for their encouragement and to my sister for all her support and valuable input.

NOMENCLATURE

HT – High Temperature

HTRMB – High Temperature Radial Magnetic Bearing

PM – Permanent Magnet

HTPMRMB – High Temperature Permanent Magnet Radial Magnetic Bearing

OD – Outer Diameter

ID – Inner Diameter

RBTFR – Radial Bearing Force Test Rig

HTPM – High Temperature Permanent Magnet

HTPMCMB – High Temperature Permanent Magnet Combo Magnetic Bearing

TABLE OF CONTENTS

	Page
ABSTRACT	iii
DEDICATION	v
ACKNOWLEDGEMENTS	vi
NOMENCLATURE	vii
TABLE OF CONTENTS	viii
LIST OF FIGURES	x
LIST OF TABLES	xvi
1. INTRODUCTION	1
1.1 Overview	1
1.2 Advantages and Disadvantages of Magnetic Rotor Bearings	2
1.3 Objectives	3
1.4 Contribution	3
1.5 Significance	4
1.6 Literature Review	4
2. DESIGN OF HTRMB	7
2.1 HTRMB Magnetic Design	7
2.2 HTRMB Mechanical Design	13
3. HTRMB FORCE TEST RIG	17
3.1 Design of RBFTR	17
3.2 Assembly of Test Setup	21
4. TESTING OF HTRMB	35
4.1 High Potting Test Results	35
4.2 Control and Bias Flux in HTRMB	42
4.3 Radial Bearing Force Test Results	47
4.3.1 Experimental procedure	48

	Page
4.3.2 Test results and correlation	49
4.3.3 Radial bearing test results from rig with 4 load cells	54
4.3.4 Bearing position and current stiffness	56
5. FULL MAGNETIC BEARING TEST RIG	57
5.1 Axial Thrust Bearing Design.....	58
5.2 High Temperature Motor Design	60
5.3 Shaft Design	62
5.4 Stress Analysis and Interference Fits	63
5.5 High Temperature Displacement Sensor Calibration.....	69
5.6 Heating and Insulation Setup	78
5.7 Principle of Fault Tolerant Control	86
5.7.1 Decoupling choke design	87
5.7.2 Prediction of self inductance	88
5.7.3 Testing of self and mutual inductance.....	89
6. INTEGRATION AND ASSEMBLY OF ALL COMPONENTS.....	102
6.1 Assembly of Motor-Bearing System.....	106
7. CONCLUSION AND FUTURE WORK	112
7.1 Future Work	113
REFERENCES	114
VITA	117

LIST OF FIGURES

	Page
Figure 2-1 Solid model of radial bearing	9
Figure 2-2 Results of FEA calculations with bias and control flux	10
Figure 2-3 Segmented back-irons	11
Figure 2-4 Flux contours and vectors.....	11
Figure 2-5 Properties of EEC T550C permanent magnets [Source: EEC]	12
Figure 2-6 Magnetization curves for Hiperco-50 alloy [Source: NASA]	13
Figure 2-7 Model of permanent magnets	14
Figure 2-8 Solid model of the stator.....	14
Figure 2-9 Rotor laminate stack	15
Figure 2-10 Dummy shaft for rotor	15
Figure 2-11 Solid model of back-iron	16
Figure 3-1 Radial bearing force test rig.....	18
Figure 3-2 Base plates	19
Figure 3-3 Stator support ring plates.....	19
Figure 3-4 Stator sub-assembly.....	20
Figure 3-5 Rotor sub-assembly	20
Figure 3-6 Schematic of the test setup	21
Figure 3-7 Hiperco-50 stator laminates.....	22
Figure 3-8 Fixture for laminate alignment	23
Figure 3-9 Stator made using laminates.....	23

	Page
Figure 3-10 Assembled magnet.....	24
Figure 3-11 Magnet to stator fixture	24
Figure 3-12 Stator with support rings and dummy shaft.....	25
Figure 3-13 Stator and support ring alignment	26
Figure 3-14 Rotor laminates and shaft	26
Figure 3-15 Shaft-Bearing assembly.....	27
Figure 3-16 Dial indicators	28
Figure 3-17 Metal shims between shaft and stator.....	28
Figure 3-18 Zircar insulation plates	29
Figure 3-19 Zircar insulation on the rig	29
Figure 3-20 Entire test setup	30
Figure 3-21 Dummy load cells.....	31
Figure 3-22 Actual load cells	31
Figure 3-23 Monolithic shaft support.....	32
Figure 3-24 Stator ring support.....	32
Figure 3-25 Side view of test rig	33
Figure 3-26 Band heaters at 1000 °F.....	33
Figure 3-27 Metal shims	34
Figure 4-1 Stator-1 (horizontal)	35
Figure 4-2 Stator-1 (vertical).....	36
Figure 4-3 View of inner face of stator	36

	Page
Figure 4-4 View of outer form of stator	37
Figure 4-5 Combined bias and control flux in HTRMB	43
Figure 4-6 Flux density vs. amp-turns	44
Figure 4-7 Test setup to measure control flux density	45
Figure 4-8 Measured control flux density	46
Figure 4-9 Schematic of the two load cell setup	47
Figure 4-10 Measured force vs. position with zero current	49
Figure 4-11 Force vs. current with position fixed, at room temperature	50
Figure 4-12 Force vs. current 1	51
Figure 4-13 Force vs. current 2	52
Figure 4-14 Force vs. current 3	52
Figure 4-15 Force vs. current 4	53
Figure 4-16 Force vs. current 5	53
Figure 4-17 Force vs. current 6	54
Figure 4-18 Radial bearing test rig with four load cells installed	55
Figure 4-19 Force vs. current at room temperature	55
Figure 5-1 Schematic of universal magnetic bearing test rig	57
Figure 5-2 Thrust bearing components	58
Figure 5-3 Graph-alloy catcher bearings	59
Figure 5-4 Axial thrust bearing	59
Figure 5-5 Buried poles in motor	60

	Page
Figure 5-6 EEC high temperature permanent magnet motor	61
Figure 5-7 Solid model of the shaft.....	62
Figure 5-8 Cross-section of shaft assembly	63
Figure 5-9 Locations with interference fits on shaft	63
Figure 5-10 Schematic of the analysis	64
Figure 5-11 Radial interference vs. speed at 1000 °F	65
Figure 5-12 Stress vs. radial position for disk.....	66
Figure 5-13 Stress vs. radial position for the shaft.....	67
Figure 5-14 Shaft test piece.....	68
Figure 5-15 Torque vs. temperature	68
Figure 5-16 Test setup	69
Figure 5-17 Clamping mechanism for sensor	70
Figure 5-18 High temperature sensors after and before heat test.....	70
Figure 5-19 Channel 1	72
Figure 5-20 Channel 2	72
Figure 5-21 Channel 3	73
Figure 5-22 Channel 4	73
Figure 5-23 Channel 5	74
Figure 5-24 Channel 6	74
Figure 5-25 Channel 7	75
Figure 5-26 Channel 8	75

	Page
Figure 5-27 Channel 9	76
Figure 5-28 Channel 1 in operating range	77
Figure 5-29 Channel 1 in full range	77
Figure 5-30 Estimates of power requirements for the system	80
Figure 5-31 Estimation of heat loss	81
Figure 5-32 Power delivered with respect to temperature	82
Figure 5-33 Estimated time taken to heat the system using only band heaters	84
Figure 5-34 Radiant heater test	85
Figure 5-35 Model of the radiant heating setup	85
Figure 5-36 Radial bearing and decoupling choke	87
Figure 5-37 Equivalent electrical circuit of the bearing coils	89
Figure 5-38 Expected output plot to determine the inductance	90
Figure 5-39 Schematic diagram of the experimental setup	91
Figure 5-40 Test Setup to measure the inductance	92
Figure 5-41 Decoupling choke along with the radial bearing	92
Figure 5-42 Mutual inductance in coil 4 due to coil 1	94
Figure 5-43 Mutual inductance in coil 5 due to coil 1	94
Figure 5-44 Mutual inductance in coil 6 due to coil 1	95
Figure 5-45 Mutual inductance in coil 1 due to coil 4	95
Figure 5-46 Mutual inductance in coil 5 due to coil 4	96
Figure 5-47 Mutual inductance in coil 6 due to coil 4	96

	Page
Figure 5-48 Self inductance of coil 1	98
Figure 5-49 Self inductance of coil 2	98
Figure 5-50 Self inductance of coil 3	99
Figure 5-51 Self inductance of coil 4	99
Figure 5-52 Self inductance of coil 5	100
Figure 5-53 Self inductance of coil 6	100
Figure 6-1 Floor mounted housing	103
Figure 6-2 Support structure and spin pit lid	104
Figure 6-3 Motor system components	105
Figure 6-4 Full motor system	106
Figure 6-5 Section of motor system	107
Figure 6-6 Side view radial bearing subsystem	107
Figure 6-7 Radial bearing subsystem	108
Figure 6-8 Band heater mounted on the outer cylinder	109
Figure 6-9 Heater controller cabinet and the controller (inset)	110
Figure 6-10 Zircar insulation and radiant heaters mounted	111

LIST OF TABLES

	Page
Table 2-1 New HTPMRMB dimensions.....	8
Table 2-2 Comparison between new and original HTPMRMB.....	9
Table 4-1 HTRMB-1, stator-1 high-pot results.....	38
Table 4-2 HTRMB-1, stator-2 high-pot results.....	39
Table 4-3 HTRMB-2, stator-1 high-pot results.....	40
Table 4-4 HTRMB-2, stator-2 high-pot results.....	41
Table 4-5 Control flux density	43
Table 4-6 Measured control flux density	45
Table 4-7 Position and current stiffness.....	56
Table 5-1 Sensor channel sets	71
Table 5-2 Parameters used to determine heat requirements.....	79
Table 5-3 Values of measured mutual inductance	93
Table 5-4 Values of self inductance	97

1. INTRODUCTION

1.1 Overview

Magnetic bearings are one of the biggest advancements in the area of bearings for rotary machinery. The major need for study in this area is because magnetic bearings have found their application in extreme environment. This has hence introduced new ideas that are being conceptualized in the application of magnetic bearings for rotating machinery because of its unique properties. Some of its properties include the absence of contact between rotating members and active control of the dynamic parameters. Recent research and application has increased its application in the high temperature environment [1]. Magnetic bearing is one cutting edge technology that will allow engines to operate at speeds and temperature well beyond the limits of current technologies. Magnetic bearings are well suited to operate at elevated temperature, higher rotational speeds, and extreme altitudes and are a promising solution to current limitations [2] [3].

Along with the aforementioned benefits of such a bearing systems of no contact between the rotor and stator, higher speed capabilities, the elimination of the lubrication systems is a big plus [4]. The absence of lubrication and contaminating wear make the magnetic bearing system exceptional for use in clean rooms, sterile rooms, or vacuum rooms.

This thesis follows the style and format of Journal of Mechanical Design.

Magnetic bearing losses are less than conventional bearings resulting in lower operating costs. Magnetic bearings are being implemented into turbo-machinery because of their lower maintenance costs and higher life span. It is also possible to adapt the stiffness and the damping of the bearing to absorb any vibration that might occur [5]. In addition to supporting loads, magnetic bearings directly measure bearing reaction forces. This enhances their application as engineering tools by providing a diagnostic and measurement tool for rotating machines. In order to obtain these loads the force as a function of current, air gap, operating frequency, and alignment must be known [6].

Recent research and application has increased its application in the high temperature environment. The objective of this research was to design and develop a high temperature permanent magnet biased bearing system, which will run at high rpm and high temperature environment.

1.2 Advantages and Disadvantages of Magnetic Rotor Bearings

Some of the *advantages* of magnetic bearings are listed below:

- Free of contact and absence of lubrication and contamination.
- High rotation speeds can be achieved.
- Low bearing losses at high operation speeds resulting in lower operating costs.
- Lower maintenance costs and higher life due to absence of mechanical wear.
- The precision with which the rotor can be controlled.
- Vibration isolation.

Some of the *disadvantages* are:

- The bearings are usually expensive due to its complexity.
- Resources needed to provide the desired currents to improve load carrying capacity.
- Complexity in design for application in high temperature environments.

1.3 Objectives

- Design and build a permanent magnet biased, radial magnetic bearing that can operate at 1000° F while supplying 500 lb-f load capacity.
- Test the radial bearing at high potential for breakdown at room and high temperature (1000 °F). This will also provide a means of measurement of the effective resistance.
- Testing of the radial bearing to determine the force to current relationship and correlate with the predicted relation.
- To experimentally measure the position and current stiffness of the radial bearing.
- Design and build a full magnetic bearing test rig broadly consisting of 2 permanent magnet biased radial bearings, 1 axial thrust bearing, 1 motor and 2 catcher bearings that can be used to test magnetic bearings at high speeds and at high temperatures nearing 1000° F .

1.4 Contribution

- Prove that the application of *Permanent Magnet Biased* magnetic bearings in *high temperature* applications is feasible.

- The novelty of this research is the use of permanent magnets to provide the bias flux. The use of *permanent magnets for bias at high temperatures* in magnetic bearings.
- Another unique nature is that it will provide a basis for future research with permanent magnet biased and *fault tolerant* magnetic bearings.

1.5 Significance

Due to the inherent advantages of magnetic rotor bearings, the application of these bearings is increasing. Some of the current applications include vacuum and clean-room techniques, machine tools and turbomachinery. This research and future research from these findings will help better understand and apply such magnetic bearings in high temperature and high speed environments. Due to permanent magnet bias used in these bearings they reduce the resources required in terms of the current required to carry the static loads. This can hence be used in applications where bearings need to operate near the heat source such as Air Turbines or in places where the natural conditions are very hot such as Deep Ocean drilling.

1.6 Literature Review

The idea of suspending or also known as levitation of a rotating shaft using magnetic bearing has been around since 1842. Successful magnetic levitation bearing was successfully demonstrated around midway through the 1800's. In the late 1930s applications on magnetic levitation were being proposed by researchers with Kemper

who patented the idea of a hovering suspension and Beams and Holmes were working on electromagnetic suspension [7].

The use of permanent magnets to levitate objects had a few problems wherein you could not levitate in all six directions. Later, in 1939, it was discovered that materials with diamagnetic properties could allow a suitable permanent magnet to hover an object with stability [5]. This is when the electromagnetic bearing concepts came into existence because of the short comings in the force generated by the permanent magnets and rendering it not suitable for practical use [1].

A permanent magnet biased magnetic bearing that has the characteristics of the coplanar geometry is usually known as a homopolar design. As described by Meeks et al. [8], such geometry was found in electromagnetic bearings with permanent magnet bias. Homopolar bearing designs generally have a permanent magnet in the back-iron to provide the bias flux. Electric coils can also be used in place of permanent magnets to provide for this bias flux to the stators. The supply of bias flux leads to advantages in the form of reduced electrical power requirements and also as a consequence power lost due to coil current is decreased. Sortore et al. [9] released experimental data that showed significant reduction in power consumption by permanent magnet biased Homopolar bearings. Lee, Hsio, and Ko [10] described various equations and developed advanced circuit models to predict and calculate the flux paths and other parameters for bearings using permanent magnets. A comparison between the predicted and measured force and stiffness characteristics of bearing were performed by Imlach, Blair, and Allaire [11].

The study of the important factor called hysteresis effect was published by Fittro, Baun, Maslen, and Allaire [12].

Palazzolo and Kenny [13] of TAMU-VCEL described the single plane magnetic bearing with permanent magnet that has lower coil resistance. Provenza, Palazzolo, Hansen et al. [3] described the open loop, experimental force and power measurements of a radial, redundant-axis, magnetic bearing at temperatures to 1000 °F and rotor speeds to 15,000 rpm. Mohiuddin [1] described and demonstrated the working of a high speed and high temperature electromagnetic axial bearing. Hossain [2], experimentally showed the results of a radial bearing that uses poles with permanent magnets which was designed for supplying 500 lb-f at 1000°F and permanent magnets only provide the bias flux.

2. DESIGN OF HTRMB

2.1 HTRMB Magnetic Design

Initially a HTRMB was designed and built, but due to certain factors like weight and the linearity of the load capacity in the design there was need to improve on the original design [2]. The following sections discuss the new *Improved Design of the High Temperature, PM Biased Radial Magnetic Bearing (HTPMRMB) in comparison with the original design.*

The dimensions for a lighter weight high temperature radial bearing with Hiperco-50 components were calculated. This weighed 46.8 lb including the wire coils, magnets, and stator, back-iron, and rotor laminates. The Finite Element Analysis (FEA) model of the bearing confirmed the weight without the coils to be 42.4 lb. The FEA calculation of the load capacity with 15 Amp current was 656 lb at 1000°F in the direction halfway between two coils separated by sixty degrees. The bias flux density in the air gap was 0.53 Tesla. The dimensions of this radial bearing are given in Table 2-1.

A comparison between several key parameters of the original radial bearing and the new design of the radial bearing are shown in Table 2-2. The new and original bearings have a similar outer diameter. The weight of the new design is predicted to be lower, although the actual weight of the new design may be a little heavier due to the weight of the coil potting, etc. The main benefit of the new design, is that for a comparable weight it has a better linear load capacity which is over 600 lb with 15 A. This is due to the new design possessing a higher bias flux in the air gap.

Table 2-1 New HTPMRMB dimensions

Rotor Laminate ID	2 x .75 in
Rotor Laminate OD	2 x 1.6 in
Stator Laminate ID	2 x 1.62 in
Stator Slot Dia.	2 x 2.794 in
Stator Laminate OD	2 x 3.447 in
Stator Thickness	1.138 in
Distance Between Stators	0.569 in
Magnet ID	2 x 3.447 in
Magnet Covered Angle	55 degrees
Magnet Thickness	1.138 in
Magnet OD	2 x 4.167 in
Back-iron ID	2 x 4.167 in
Back-iron OD	2 x 4.674 in
Number Turns/Coil	36
Inductance/Coil	.00206 H

Table 2-2 Comparison between new and original HTPMRMB

Key Parameter	New Design	Original Design
Bearing OD	9.35 in.	9.10 in.
Bearing Length	3.22 in.	3.97 in.
Bearing Weight	46.8 lb	60 lb
Load capacity at 1000 °F	656 lb (15 A linear)	330 lb (13 A nonlinear limit)
Air gap bias flux density	0.53 T	0.45 T

Figure 2-1 Solid model of radial bearing shows the solid model of the new design for the **HTPMRMB** and Figure 2-2 shows the flux density with both the permanent magnet flux and 15 amp coil current applied. The two top poles have bias flux with control flux added, while the poles on bottom have bias flux and the control flux is subtracted.

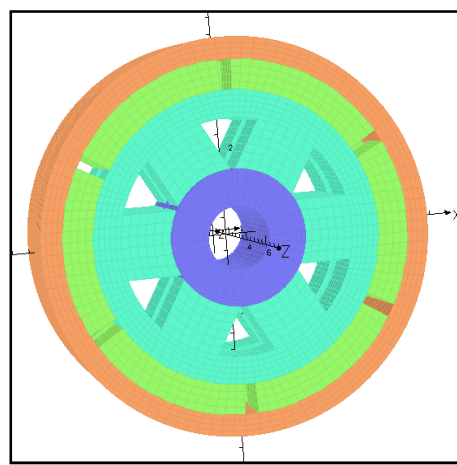


Figure 2-1 Solid model of radial bearing

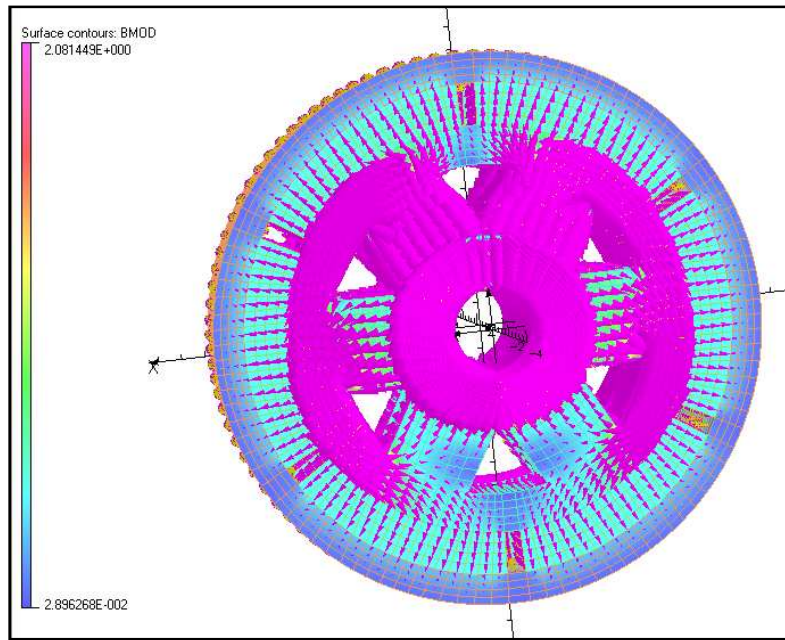


Figure 2-2 Results of FEA calculations with bias and control flux

An FEA model was made for the high temperature EEC radial bearing with a segmented back-iron. Segmenting the back-iron makes the bearing much easier to manufacture and assemble. The back-iron segments were separated by 0.1 in. gaps. This is the same as a separation angle of 1.375 degrees. The force, according to the finite element analysis, was 656 lb with the conventional cylinder back-iron and 602 lb with the segments. This force is with 15 A current applied to the coils on the four poles on top and -15 A current applied to the four poles on bottom. Figure 2-3 shows the segmented parts of the back-iron and Figure 2-4 shows the flux contours and vectors of the bearing due to 15 amps current applied to the radial bearing with segmented back-iron. It is observed that the flux vectors are parallel to the segmented slots. The magnetic design

was done by Dr. Kenny using material data provided by EEC and NASA. The Electron Energy Plot in Figure 2-5 shows a decrease in permanent magnet strength as temperature increases.

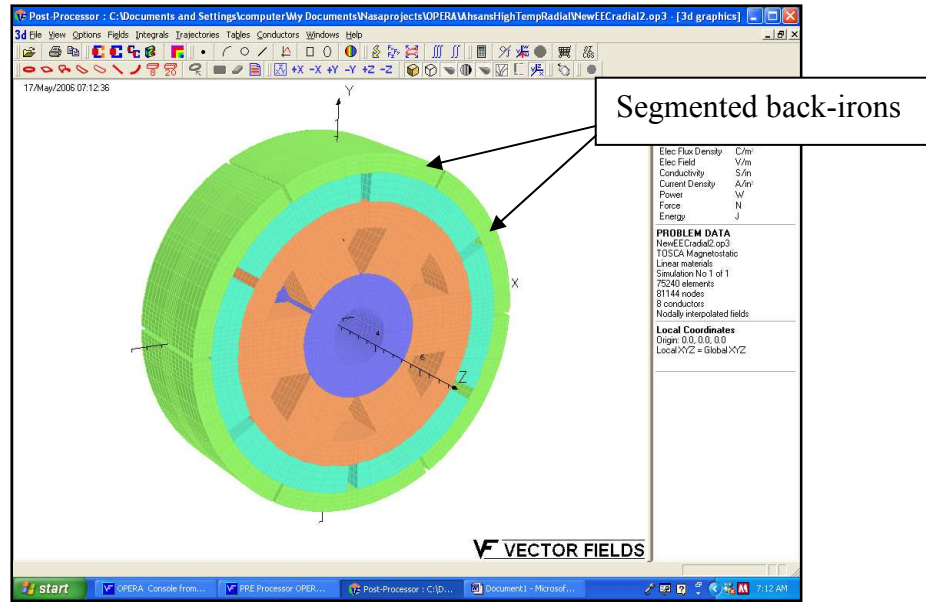


Figure 2-3 Segmented back-irons

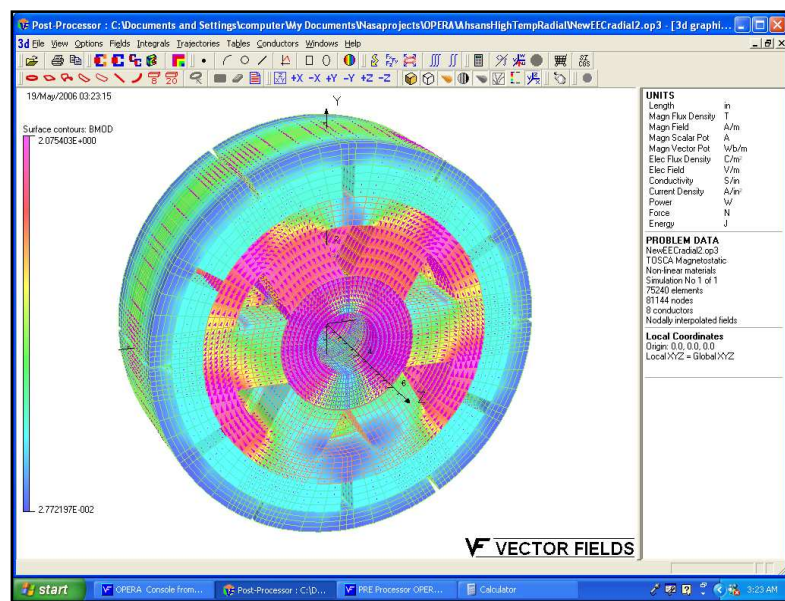


Figure 2-4 Flux contours and vectors

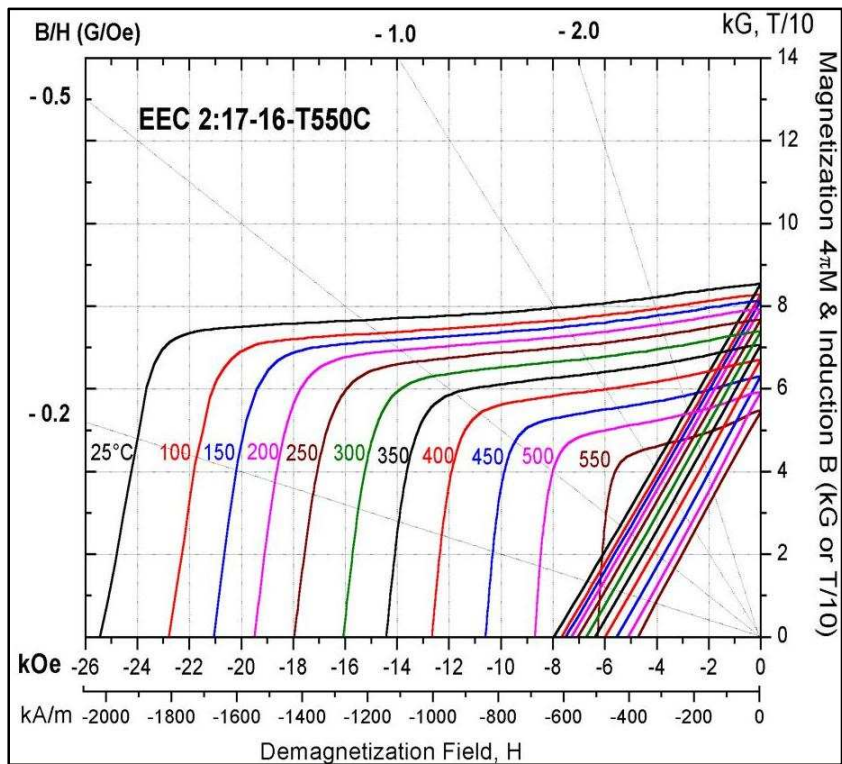


Figure 2-5 Properties of EEC T550C permanent magnets [Source: EEC]

The bearing laminates are made using Hiperco-50 alloy which is a high-permeability cobalt-iron-vanadium alloy. The different properties of Hiperco-50 were provided by NASA in their materials handbook. Figure 2-6 shows the direct magnetization curves for Hiperco-50 0.004in laminations at different test conditions.

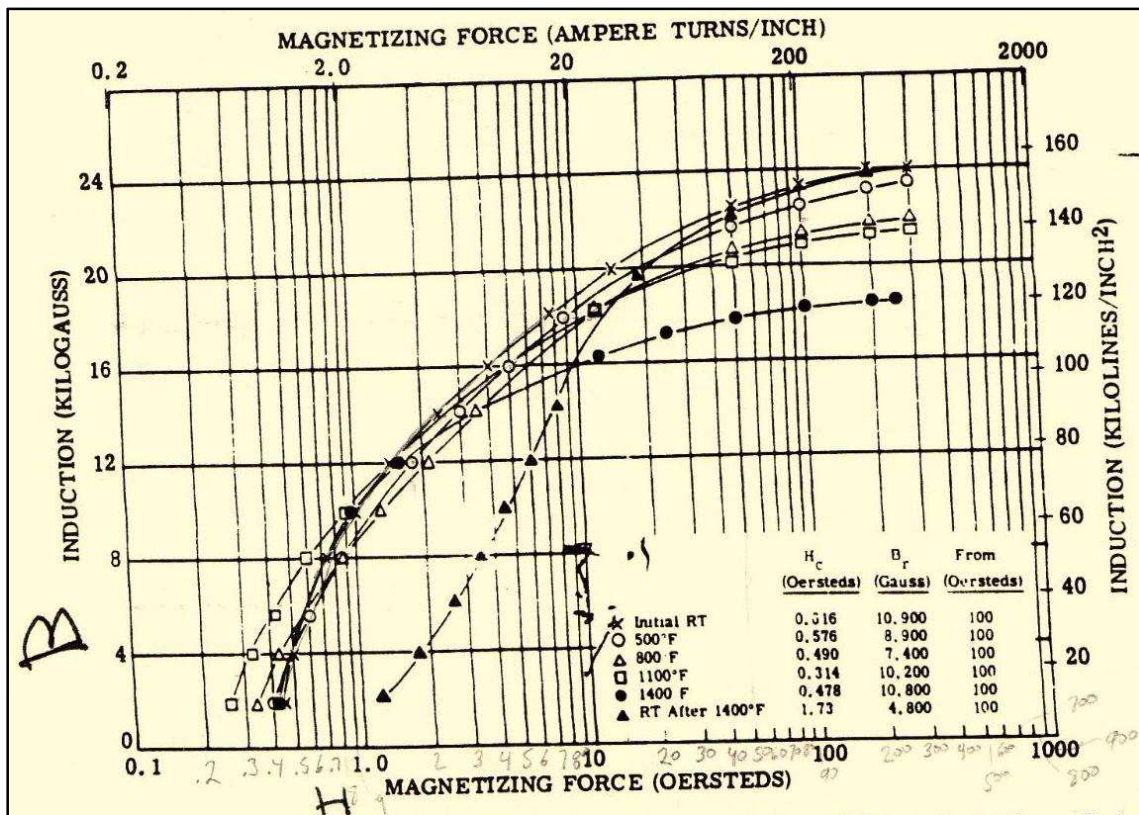


Figure 2-6 Magnetization curves for Hiperco-50 alloy [Source: NASA]

2.2 HTRMB Mechanical Design

After studying a number of designs with different considerations of size, weight, cost and most importantly the magnetic design feasibility as discussed above, the final design of the radial bearing stator was chosen. This section clearly explains the designs for all the parts that were used in the radial bearing fabrication.

The magnets that were finalized were made by EEC to serve as a high temperature source of magnetic flux for bias. Figure 2-7 shows the model of the magnets that were made by EEC. Orientation of magnetic field is such that O.D. is a north pole

and I.D. a south pole. Six magnets were made with such pole orientation for stator-1 and another six magnets with reversed polarity for stator-2. Each of these magnets consisted of five small segments that were cemented together with high temperature glue to get the arc shape shown in the Figure 2-7.

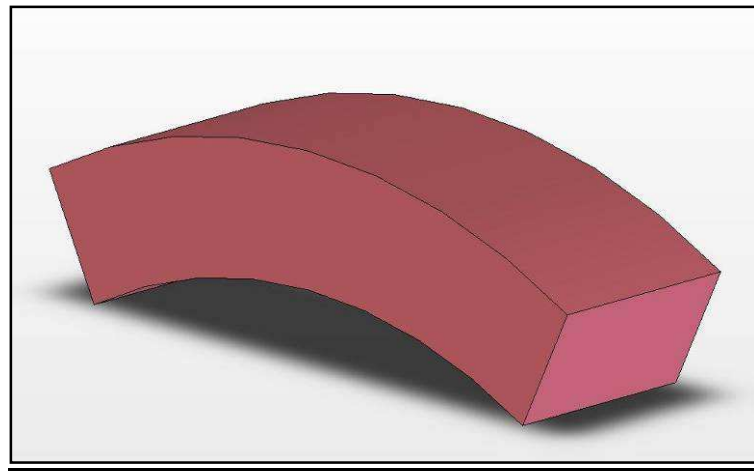


Figure 2-7 Model of permanent magnets

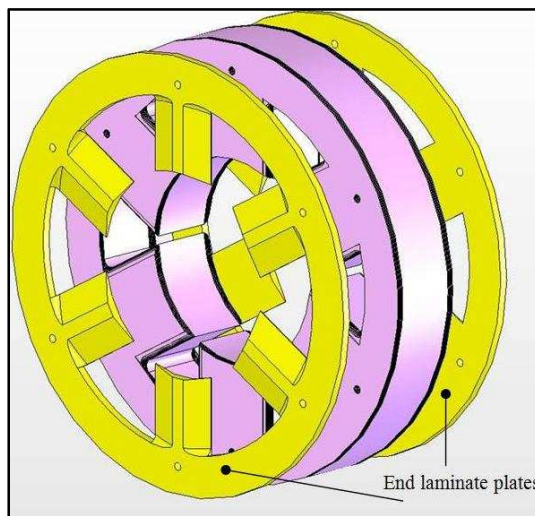


Figure 2-8 Solid model of the stator

Figure 2-8 shows the stator solid model with the end stator sandwich plates (yellow), which prevent flatness of the lamination stack. The laminates are made from Hiperco-50 and are stacked together. Figure 2-9 shows the model of the rotor laminate stack which was made of Hiperco-50 material and Figure 2-10 shows a dummy shaft that is used to position the rotor laminate stack in the stator laminate stack. The dummy shaft is made of non-magnetic Titanium Ti-4AL-6V alloy.

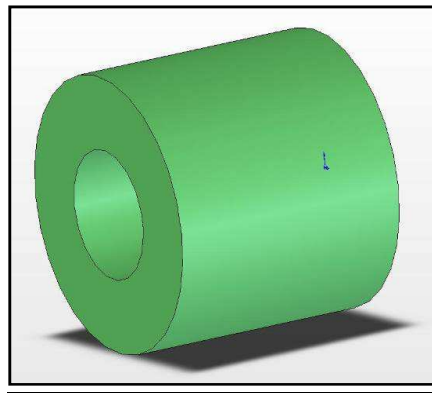


Figure 2-9 Rotor laminate stack

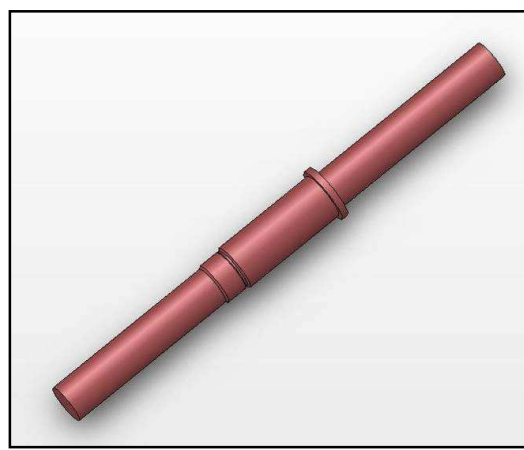


Figure 2-10 Dummy shaft for rotor

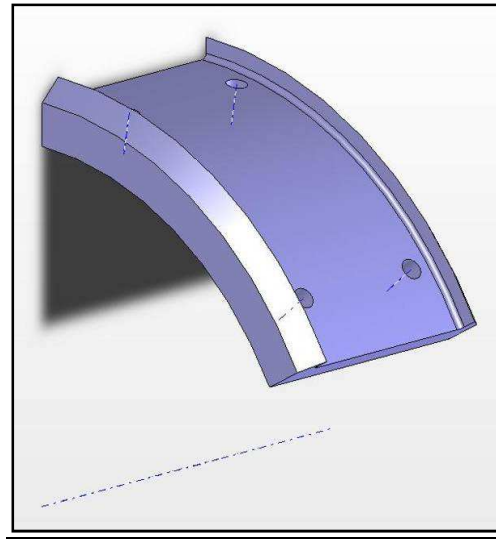


Figure 2-11 Solid model of back-iron

Figure 2-11 shows the solid model of the actual segmented back-irons that were finally made. The back-irons serve as a means to transmit bias flux along the axial direction from one stator to the other. They are also made from Hiperco-50 material.

3. HTRMB FORCE TEST RIG

3.1 Design of RBFTR

The apparatus shown in Figure 3-1 was fabricated and employed to provide accurate measurements of the radial forces produced by the radial bearings vs. temperature, current and relative position of the rotor in the bearing clearance between the stator and rotor laminate stacks. A previous build of this apparatus [2] exhibited excessive flexibility which caused the test results to possess a high uncertainty. This new design possesses the following improvements:

- Higher stiffness load cells.
- Increased resolution on load cells due to internal amplification feature.
- Better quality dial gauges to indicate the radial gap and rotor/stator relative position at all temperature conditions.
- High stiffness bearing supports provided by solid ring plates that provide high load capacity and act as a thermal barrier. These plates may be easily modified to accommodate thermal expansions if required.

A cooling base plate was employed to provide heat sink to maintain acceptable temperatures for the load cells. The base consists of two base plates made of steel that are sandwiched and sealed together for cooling water to be passed in between them as shown in Figure 3-2. The ring plates shown in Figure 3-3 provide support for the bearings and serve as a load transmission path from bearings to the load cells. The plates are manufactured from a special Titanium alloy material (Ti4Al6V) which provides a

thermal barrier to keep the bearings hot and the load cells cool. The monolithic shaft support blocks were designed to provide both vertical and horizontal displacement to rotor shaft at both of its ends, with minimal support deflection due to high stiffness. Four Load cells with internal amplifiers were used which had an upper loading capacity of 500 lb. Figure 3-4 shows the entire exploded view of the stator sub assembly and Figure 3-5 shows the rotor sub-assembly that was put through the stator. Figure 3-6 shows the schematic diagram of the complete test setup which consists of heater controls and power supply to the stator coils.

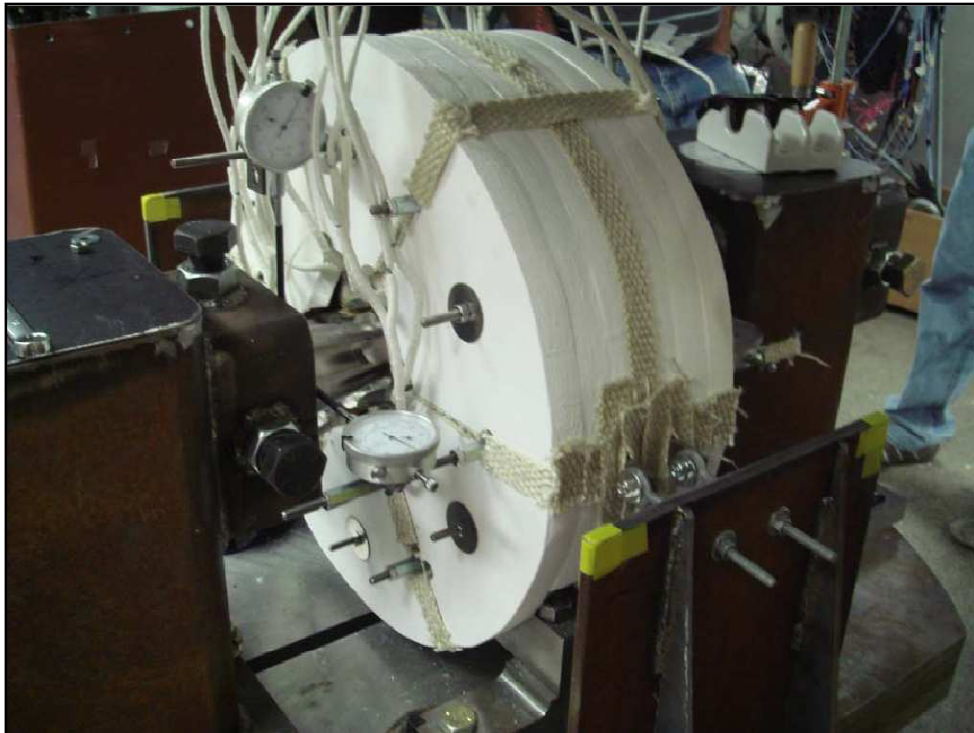


Figure 3-1 Radial bearing force test rig

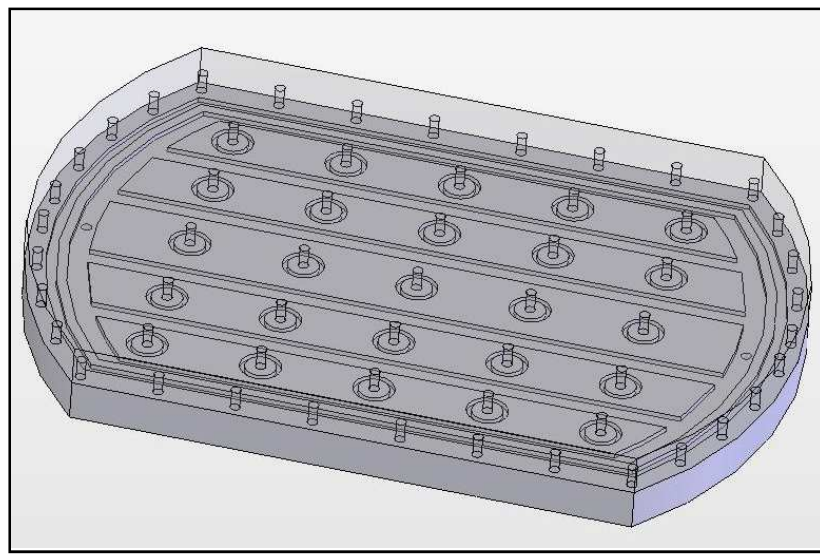


Figure 3-2 Base plates

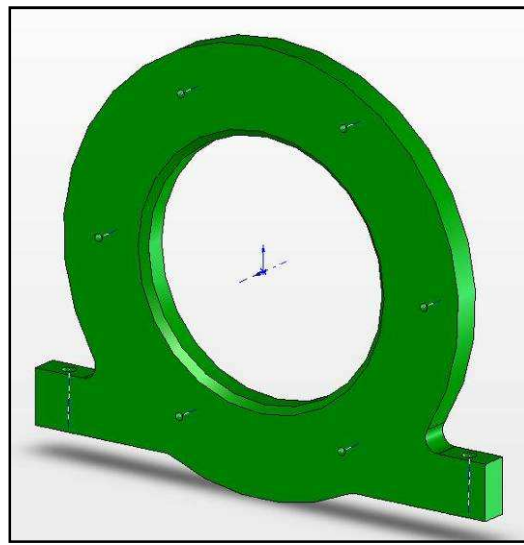


Figure 3-3 Stator support ring plates

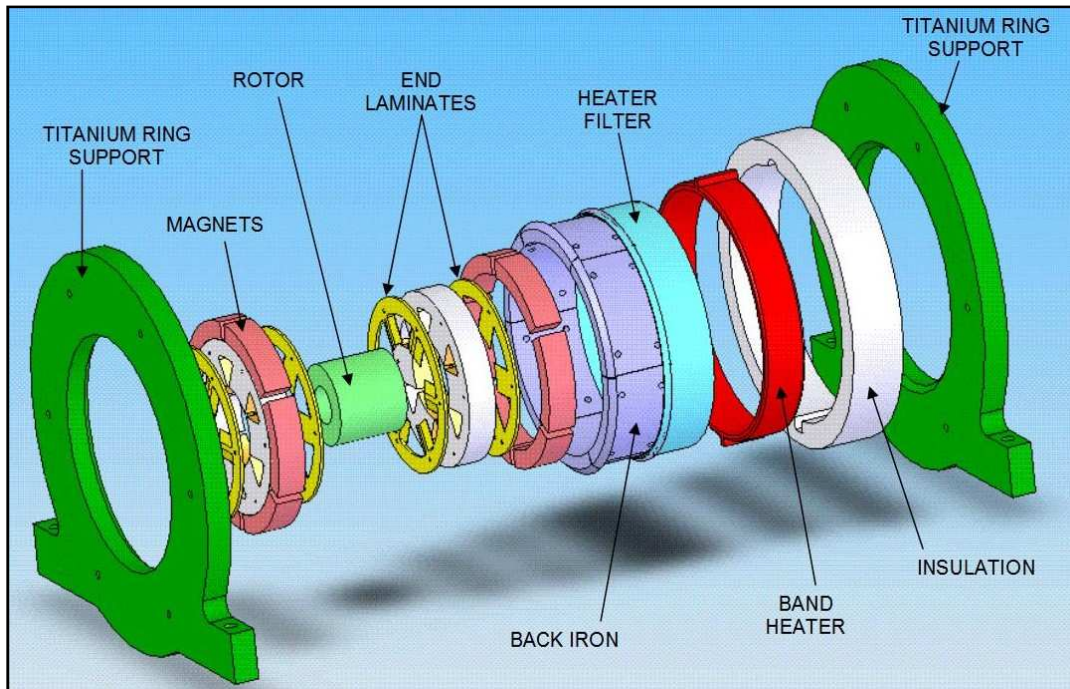


Figure 3-4 Stator sub-assembly

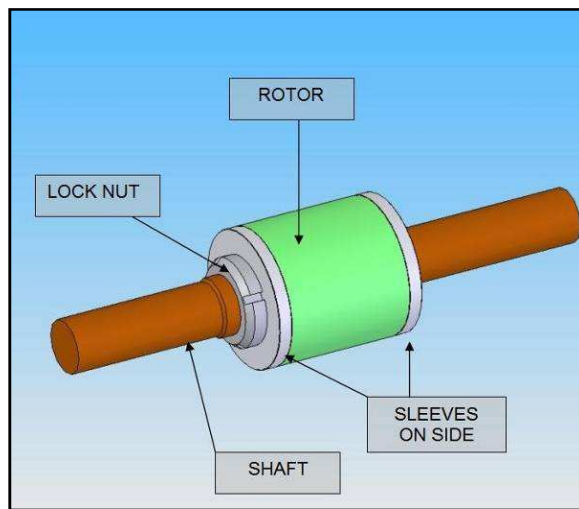


Figure 3-5 Rotor sub-assembly

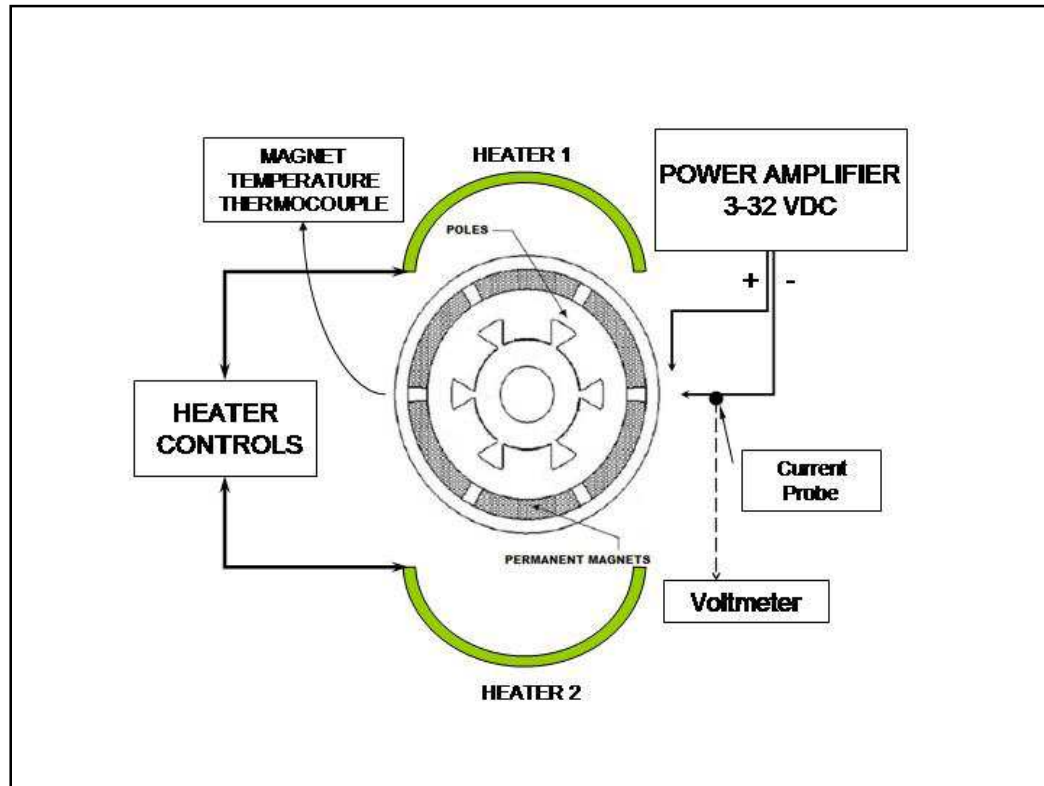


Figure 3-6 Schematic of the test setup

3.2 Assembly of Test Setup

First the stator was fabricated at the lab. The Hiperco-50 laminates used in the stator and rotor were to be heat treated according to the following schedule:

- Hold for 2 hour at 740°C in dry hydrogen
- Slow cool down at 85°C per hour

The next step was to insulate the laminations by oxidation. The inter-laminar resistance was increased in order to reduce the eddy current losses between the laminations of the rotor and stator. The Hiperco-50 laminates were heated in the oven. As a result a coating of oxidation formed on the laminates. This coating greatly increases resistance between laminations and reduces the eddy current loss. Figure 3-7 shows the stator laminates that were used. Figure 3-8 is the fixture that was designed and machined for proper alignment of the stator laminates. Figure 3-9 shows the stator that was made using the laminates and the alignment fixture.



Figure 3-7 Hiperco-50 stator laminates



Figure 3-8 Fixture for laminate alignment



Figure 3-9 Stator made using laminates

A special assembly tool was designed and machined to cement the segmented magnets. Five segmented magnets of 11 degree arc are cemented to get the desired dimension of 55 degree arc magnet. Then the magnets are cured at 204°C ($\pm 1^\circ\text{C}$) for 15 minutes. The magnet after assembly and curing is shown in Figure 3-10.



Figure 3-10 Assembled magnet

The stator was then prepared for coil winding. Each pole on the stator was first coated to provide for insulation and then wound with the wire. There are four layers of winding with each layer having 11, 11, 8 and 6 turns from the inner layer to the outer layer respectively. Once the coils are wound, then the molding process was carried out to form the potting cement on the each stator. After this the stators are baked in the oven and once ready the magnets and back-irons are put onto the stator. Shown below in Figure 3-11 is an assembly tool designed and used to lower all six pole magnets at once around each stator.



Figure 3-11 Magnet to stator fixture

The bearing assembly, which includes the stator, permanent magnets and the back-irons, was taken and then mounted onto the stator support rings. The bearing and its support rings were then carried onto the test rig and mounted at one end of the table. Throughout the assembly process a lot of care had to be taken so as to avoid damaging of the permanent magnets, stator and its coils. Figure 3-12 shows the Stator support assembly. It consists of the stator-1 and stator-2 put together along with a dummy aluminum shaft through them. The support rings are held together with $\frac{1}{4}$ in. studs and 1 in. dowels to provide proper alignment and to keep the plates parallel.



Figure 3-12 Stator with support rings and dummy shaft



Figure 3-13 Stator and support ring alignment



Figure 3-14 Rotor laminates and shaft

The next step was to fix up the alignment of the stator axis along with the support rings axes. This was done using two alignment plates as shown in the Figure 3-13. 1in. dowels were used to align the shaft, stator and the support ring axes.

After alignment, the next step was to insert the Rotor laminates and the shaft shown in Figure 3-14, into the bearing. This was done using plastic shims and the trolley mechanism to align the shaft in the X and Y directions as the shaft gets drawn into the stator. Figure 3-15 shows the mechanism that was used to insert the shaft into the bearing assembly.

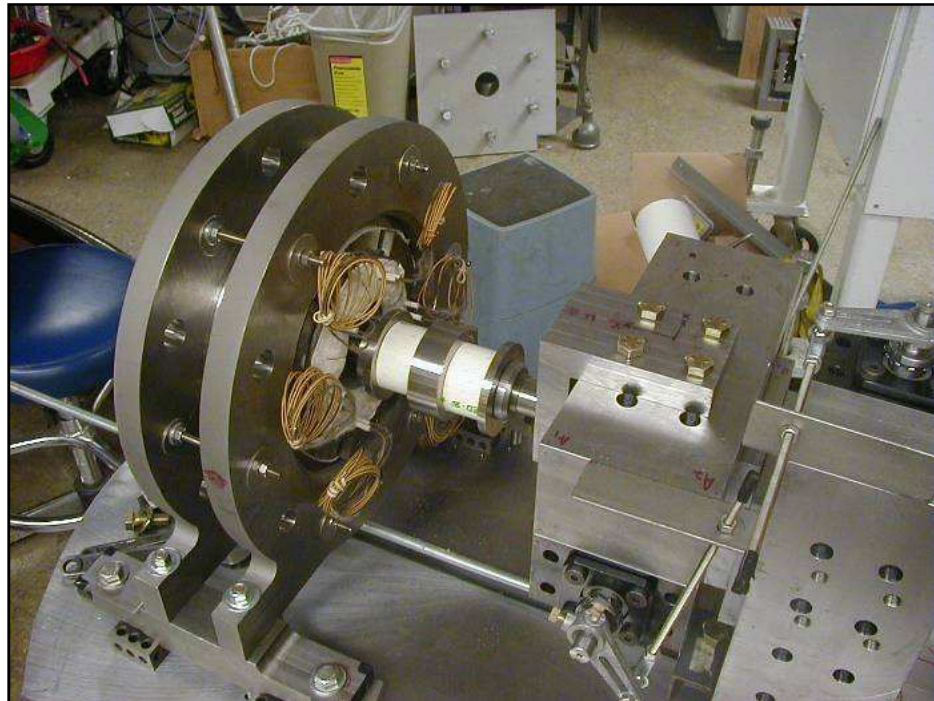


Figure 3-15 Shaft-Bearing assembly

Shown below are some of the pictures of the HTRMB test rig that was used for testing and measurements of various bearing properties. Figure 3-16 shows the dial indicators used to measure the shaft position relative to the stator. Figure 3-17 shows the metal shims that were used between the stator and the rotor to determine the position of the shaft in the bearing.

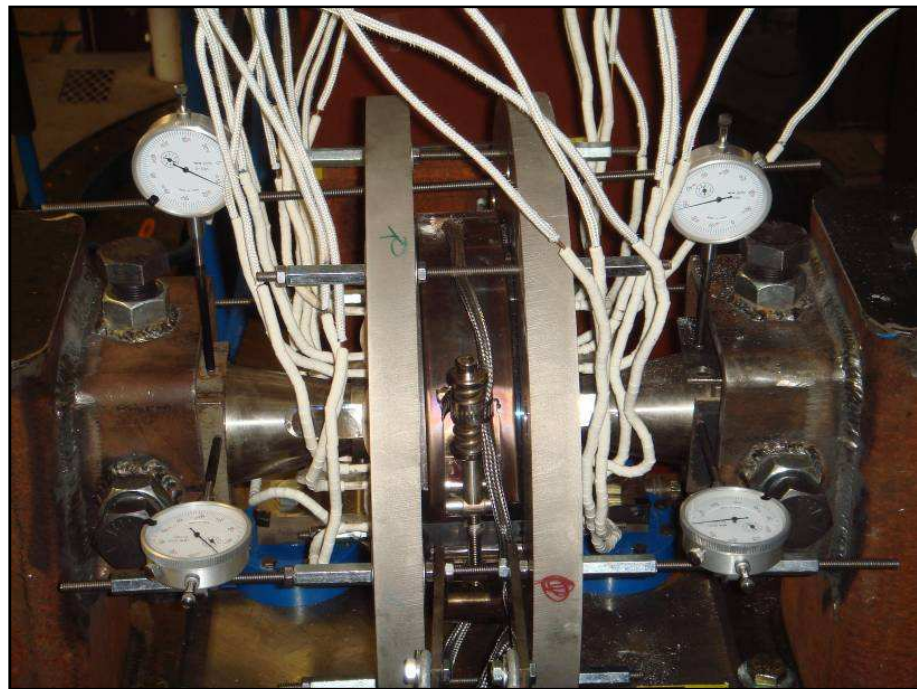


Figure 3-16 Dial indicators

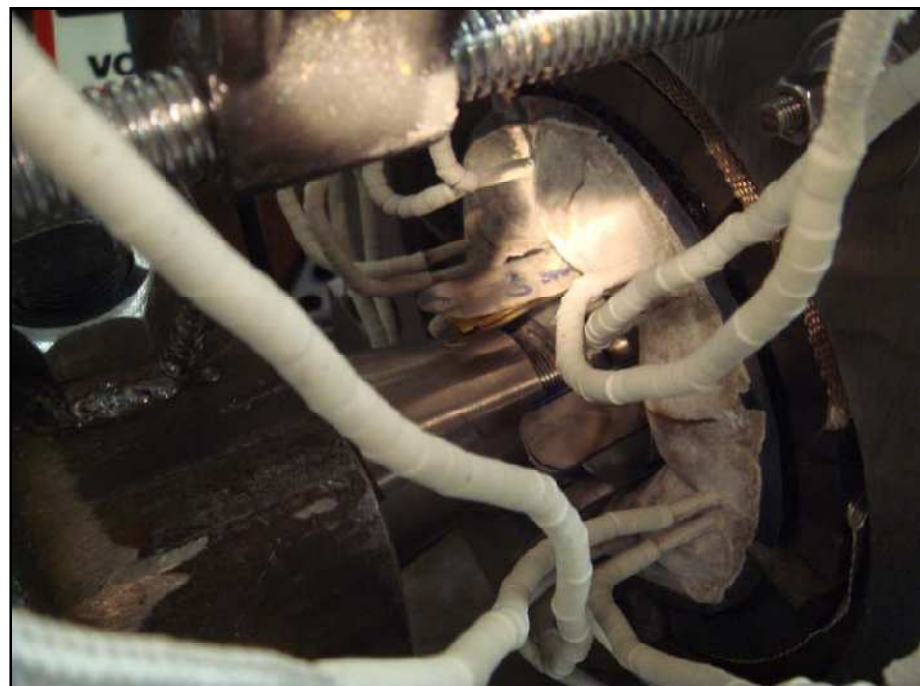


Figure 3-17 Metal shims between shaft and stator

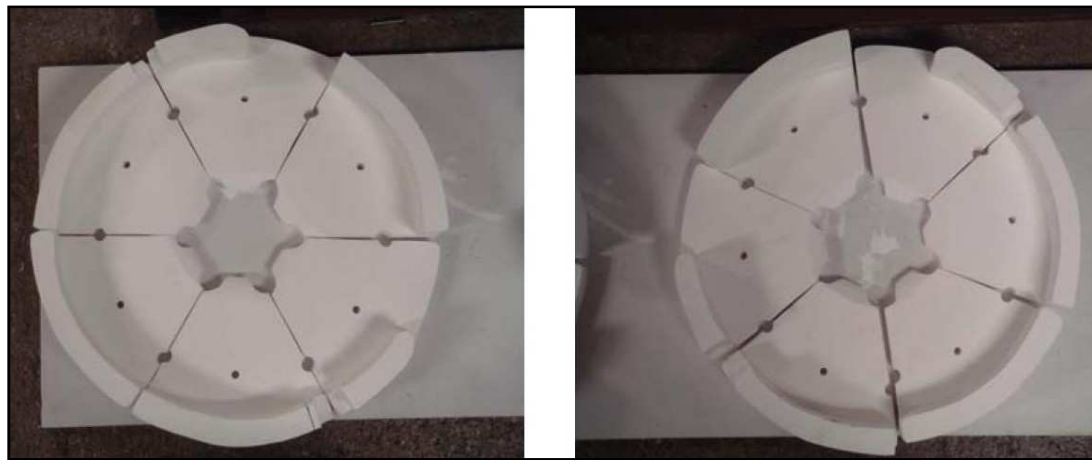


Figure 3-18 Zircar insulation plates



Figure 3-19 Zircar insulation on the rig

Figure 3-18, Figure 3-19 are the insulation plates that are used to provide a thermal barrier to efficiently heat the system. The pictures that follow illustrate various aspects to the experimental procedure. Figure 3-20 shows the entire test setup along with the ventilation systems that were installed to remove the fumes that were emitted at high temperature.

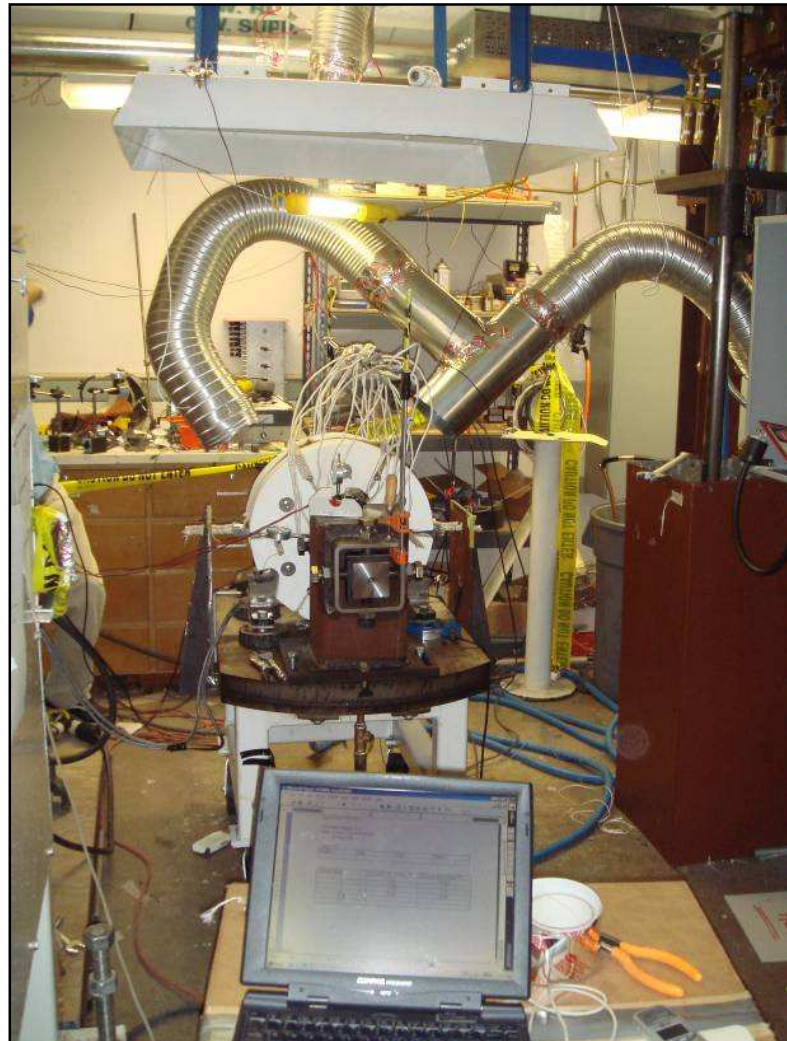


Figure 3-20 Entire test setup



Figure 3-21 Dummy load cells



Figure 3-22 Actual load cells

Figure 3-21 and Figure 3-22 show the 2 dummy solid steel load cells and the 2 actual load cells that were used respectively. Figure 3-23 and Figure 3-24 show the monolithic shaft support member and the additional support members to improve the rigidity and stiffness of the system.



Figure 3-23 Monolithic shaft support



Figure 3-24 Stator ring support



Figure 3-25 Side view of test rig

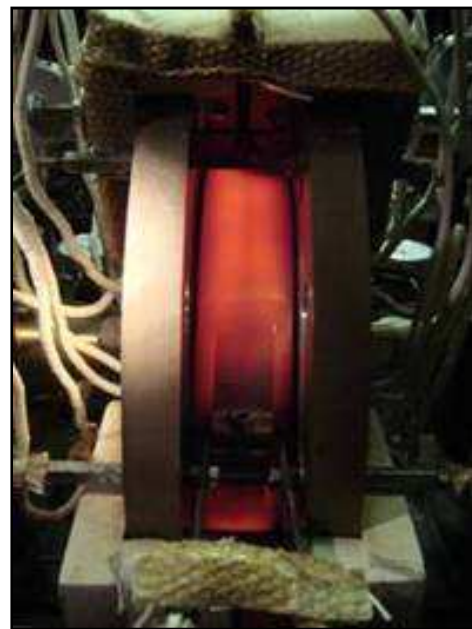


Figure 3-26 Band heaters at 1000 °F



Figure 3-27 Metal shims

Figure 3-25 shows another view of the test rig from the side. The band heaters used to heat the stator turn red hot at a 1000 °F temperature. This is shown in Figure 3-26 where the insulation on the stator is removed to reveal the heaters. Figure 3-27 shows the metal shims that were used to determine the position of the rotor shaft with respect to the stator and this also prevents the shaft from directly impacting the inner surface of the stator.

4. TESTING OF HTRMB

4.1 High Potting Test Results

The “High Potting” test is utilized to check for breakdown voltage and effective resistance. Stator-1 is shown in front of the high potting instrument in Figure 4-1. Figure 4-2, Figure 4-3, Figure 4-4 show views of the stator following a 30 minute exposure to 1000 °F.



Figure 4-1 Stator-1 (horizontal)



Figure 4-2 Stator-1 (vertical)



Figure 4-3 View of inner face of stator



Figure 4-4 View of outer form of stator

Table 4-1, Table 4-2, Table 4-3 and Table 4-4 show measurements of current with 500V applied between the magnetic bearing stator lamination stack and the individual coils on the stators. This “High Potting” procedure is utilized to check for breakdown voltage and effective resistance. *The results appear excellent even at 1000 °F since the actual maximum operating voltage will not exceed 180V. The results showed the best insulation results of all high temperature magnetic bearings ever made at the VCEL.* No signs of breakdown occurred during all of the High Pot testing. The trend surely shows a very significant increase in current between the room temperature and 1000 °F states. This verifies that high potting must be performed at high temperature in order to check the integrity of the insulation at high temperature.

Table 4-1 HTRMB-1, stator-1 high-pot results

	Temp degrees °F	Pole No.	V_{DC} volts	I_{DC} amps $\times 10^{-6}$	R_{eff} Mega- Ohms	V_{AC} volts	I_{AC} amps $\times 10^{-6}$
HIGH TEMPERATURE	1000	1	500	25	20.0	500	400
	1000	2	500	140	3.6	500	520
	1000	3	500	120	4.2	500	480
	1000	4	500	180	2.8	500	520
	1000	5	500	200	2.5	500	580
	1000	6	500	200	2.5	500	560
ROOM TEMPERATURE	76	1	500	0	∞	500	28
	76	2	500	0	∞	500	30
	76	3	500	0	∞	500	30
	76	4	500	0	∞	500	30
	76	5	500	0	∞	500	30
	76	6	500	0	∞	500	30

Table 4-2 HTRMB-1, stator-2 high-pot results

	Temp degrees °F	Pole No.	V_{DC} volts	I_{DC} amps $\times 10^{-6}$	R_{eff} Mega- Ohms	V_{AC} volts	I_{AC} amps $\times 10^{-6}$
HIGH TEMPERATURE	1000	1	500	50	10	500	420
	1000	2	500	100	5	500	400
	1000	3	500	150	3.3	500	420
	1000	4	500	180	2.8	500	450
	1000	5	500	180	2.8	500	420
	1000	6	500	150	3.3	500	460
ROOM TEMPERATURE	76	1	500	0	∞	500	32
	76	2	500	0	∞	500	35
	76	3	500	0	∞	500	34
	76	4	500	0	∞	500	34
	76	5	500	0	∞	500	28
	76	6	500	0	∞	500	30

Table 4-3 HTRMB-2, stator-1 high-pot results

	Temp degrees °F	Pole No.	V_{DC} volts	I_{DC} amps $\times 10^{-6}$	R_{eff} Mega- Ohms	V_{AC} volts	I_{AC} amps $\times 10^{-6}$
HIGH TEMPERATURE	1000	1	500	740	-	500	-
	1000	2	500	320	-	500	580
	1000	3	200	1000	-	150	1000
	1000	4	500	800	-	500	1000
	1000	5	200	1000	-	150	1000
	1000	6	400	1000	-	300	1000
ROOM TEMPERATURE	76	1	500	0	∞	500	40
	76	2	500	0	∞	500	40
	76	3	500	0	∞	500	40
	76	4	500	0	∞	500	40
	76	5	500	0	∞	500	38
	76	6	500	0	∞	500	40

Table 4-4 HTRMB-2, stator-2 high-pot results

	Temp degrees °F	Pole No.	V_{DC} volts	I_{DC} amps $\times 10^{-6}$	R_{eff} Mega- Ohms	V_{AC} volts	I_{AC} amps $\times 10^{-6}$
HIGH TEMPERATURE	1000	1	500	340	-	500	560
	1000	2	500	800	-	450	1000
	1000	3	200	380	-	500	620
	1000	4	500	300	-	500	520
	1000	5	500	520	-	500	750
	1000	6	400	1000	-	300	1000
ROOM TEMPERATURE	76	1	500	0	∞	500	36
	76	2	500	0	∞	500	36
	76	3	500	0	∞	500	35
	76	4	500	0	∞	500	36
	76	5	500	0	∞	500	34
	76	6	500	0	∞	500	36

4.2 Control and Bias Flux in HTRMB

The Homopolar radial magnetic bearing has the following components:

- Back-iron for conducting the bias flux in axial direction
- Rotor and Stator lamination stacks for circulation of the control flux
- HTPM for permanent magnet biased operation
- Specially insulated magnet wire encapsulated in ceramic housing

In case of HTRMB, there are two planes of stator with permanent magnets. The permanent magnets in all the poles in one plane of the bearing are oriented to push the bias flux into the rotor. The flux returns out through the rotor to the other plane of stator-magnets which is reversely polarized. And the control flux circulates radially. The coils on the control poles can add or subtract a control flux to the bias flux. This way the control flux can add to the bias flux on one side of the rotor and subtract from the bias flux on the other side. Thus a controllable net force on the rotor is produced in the magnetic bearing. The flux direction in the bearing is shown in Figure 4-5. Figure 4-6 and Table 4-5 show the Control flux density in air gap when all twelve coils have equal current. Further calculation (by Dr. Kenny) gave the following results:

- Bias flux density in air gap at 70 °F = 0.98 T average
- Bias flux density in air gap at 1000 °F = 0.6 T average

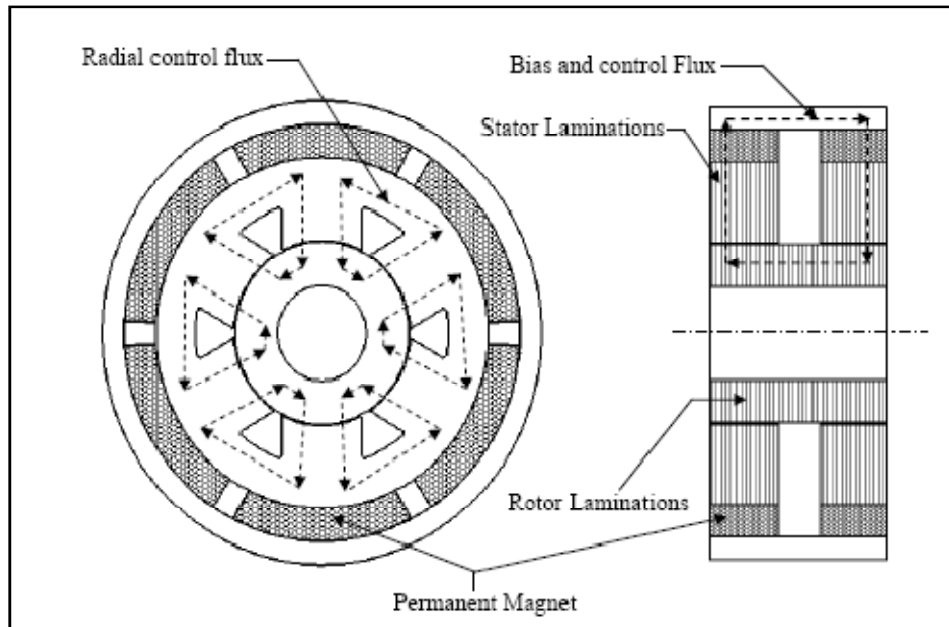


Figure 4-5 Combined bias and control flux in HTRMB

Table 4-5 Control flux density

Amp-Turns	Average Gap	
	Control Flux (TESLA)	
	1000 °F	70 °F
0	0.00	0.00
135	0.20	0.23
270	0.31	0.40
405	0.37	0.45
540	0.42	0.50

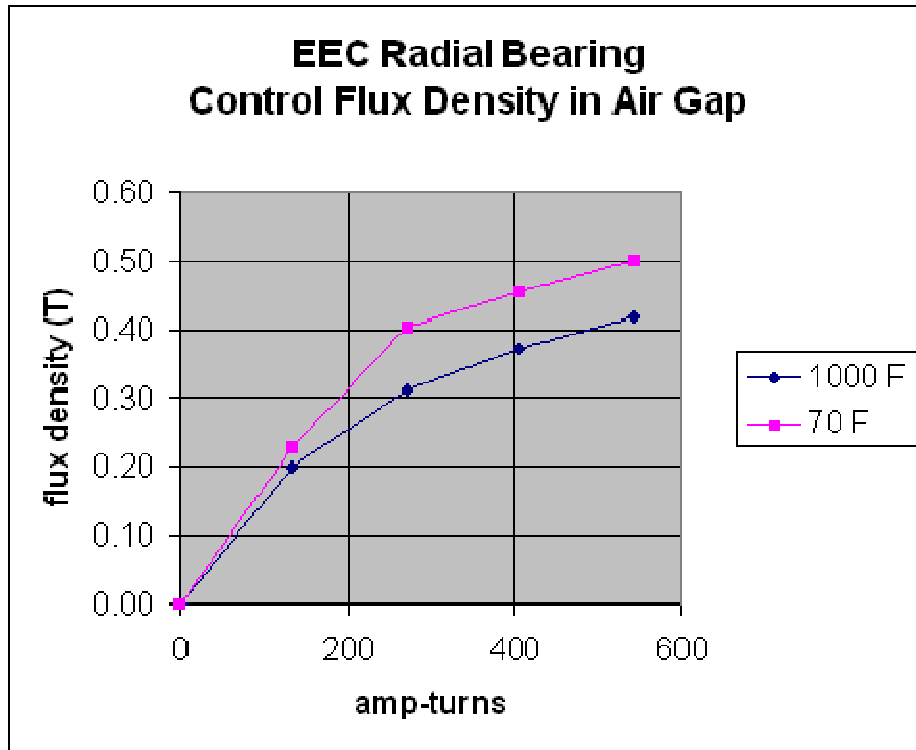


Figure 4-6 Flux density vs. amp-turns

The bias flux density was experimentally checked at room temperature. High temperature tests of the bias flux and the control flux were not possible because of unavailability of high temperature hall probes and flux meters. *The bias flux density was measured to be 0.914 Tesla.* Figure 4-7 shows the test setup used to measure the control flux density of the radial bearing. A DC power supply is used to power the coils and provide the required current. The flux density is measured using a hall probe.



Figure 4-7 Test setup to measure control flux density

Table 4-6 Measured control flux density

Amp-Turns	Average Gap Control Flux at Room Temp (70F) (TESLA)		
	Predicted	Measured 1	Measured 2
0	0.00	0	0
135	0.23	0.09	0.074
270	0.40	0.167	0.147
405	0.45	0.255	0.219
540	0.50	0.349	0.299

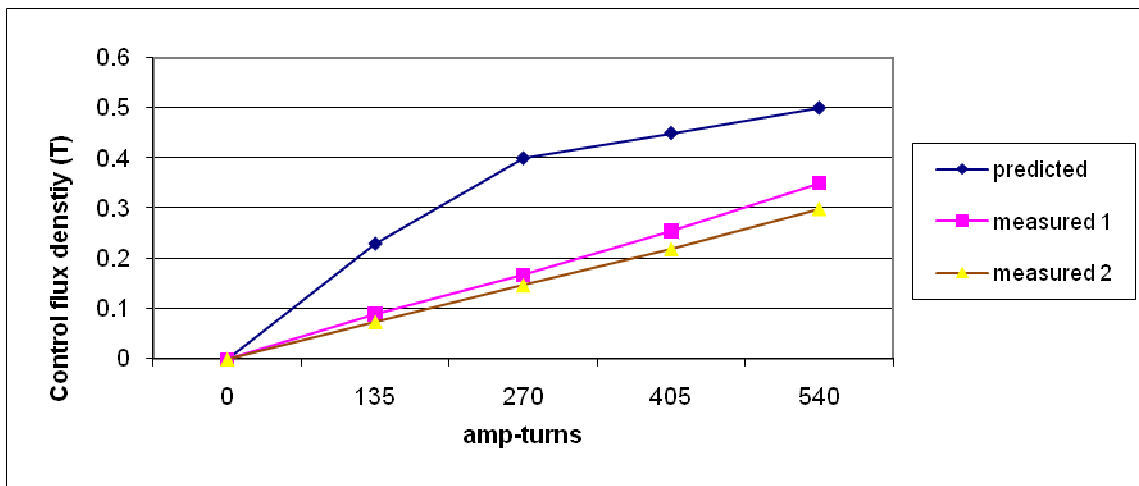


Figure 4-8 Measured control flux density

The Table 4-6 and Figure 4-8 show a comparison of the predicted values of the control flux density and the measured value. Only a couple of measurements are plotted here. Multiple readings were taken in order to check for repeatability.

The actual values of the control flux measured here showed very good repeatability. The flux density is also linear with respect to the current (amp-turns). Although, the values are slightly less than expected there could be two reasons for this discrepancy:

- The predicted values were calculated using a model with constant 20 mil air gap. There is a 15 mil uncertainty in the air gap during the testing. This is due to the shaft not being perfectly centered at the time of testing. Hence, increase in Air-gap might be causing a reduction in the control flux density.
- The second reason to explain the difference would be due to the positioning of the hall sensor. The sensor is not long enough to reach a point under the pole where the flux density is highest.

4.3 Radial Bearing Force Test Results

The Radial Bearing Force was measured to be 629 lb at a magnet temperature of 920 F and a current of 13.3 amps. This value is considered to be conservative (low) for the following reason:

Two of the four load cells failed due to excessive loading. These were replaced with solid steel “dummy” load cells of dimension similar to the actual load cells.

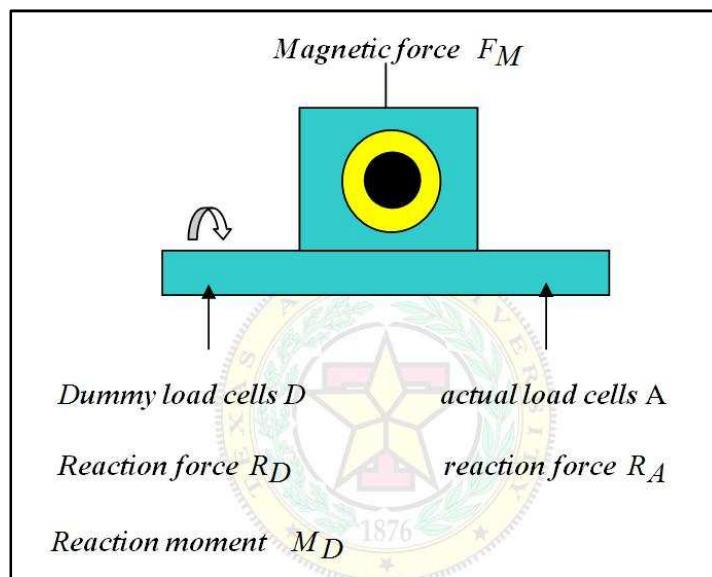


Figure 4-9 Schematic of the two load cell setup

The moment M_D results from the bolted connection of the dummy load cell and the stator support stand. This moment reduces the load on the actual load cell A . The moment M_D is neglected and moments are summed about D to obtain a conservative

(low) estimate of the magnetic force F_M has twice the measured force R_A as shown in Figure 4-9.

4.3.1 *Experimental procedure*

The Experiment on the test rig was carried out at Room temperature and at higher temperatures. The steps below explain how the data was taken for the test rig.

1. First the shaft is brought to its center by adjusting the bolts on the shaft support tower and checking if the shims are free.
2. Then the through bolts for the stator and the stator support rings are loosened so as to allow for thermal growth during the heating.
3. The heaters are then powered up and the desired temperature is set using the controllers.
4. Once the desired temperature is reached we tighten all the bolts at this steady state.
5. Again the shaft is centered to free the shims.
6. Then the current is supplied through the magnetic coils and at every data point the shims are made free and the force data is measured.

4.3.2 Test results and correlation

A significant effort was made to obtain force vs. current and temperature for the radial bearing. This resulted in a measurement methodology that yields quite repeatable and reasonable results. Figure 4-10 shows measured force vs. position with zero current for the radial bearing. *The total force is twice that shown as explained above in the Summary.* The position stiffness calculated from the plot given below is 33 lb/amp.

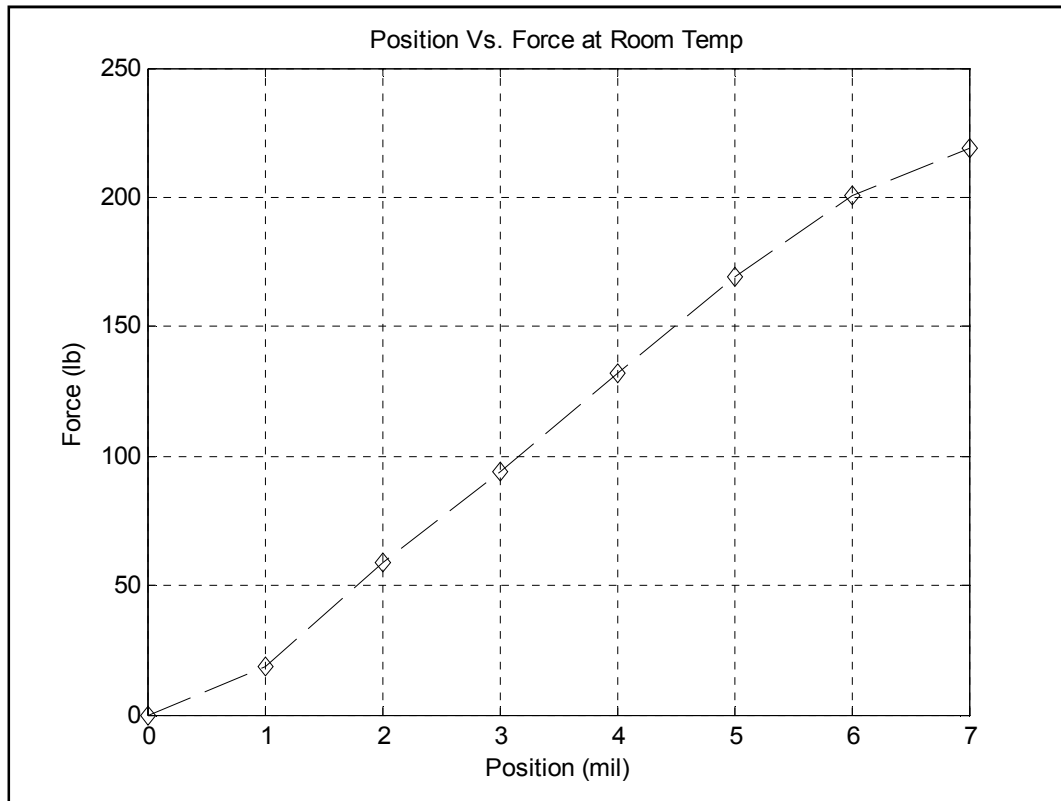


Figure 4-10 Measured force vs. position with zero current

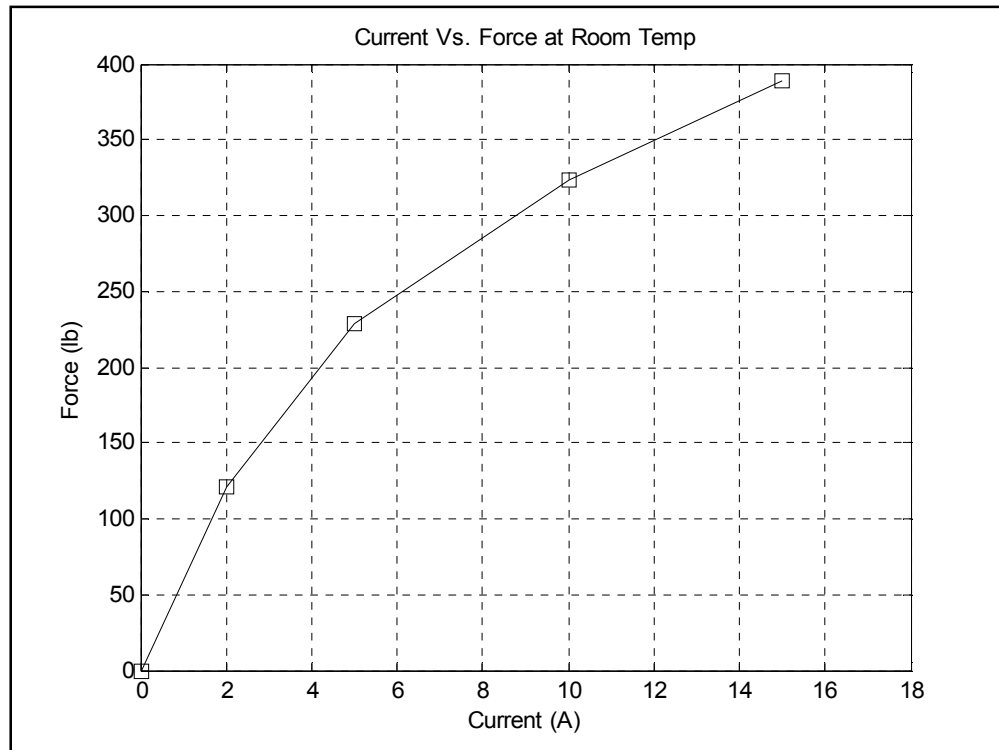


Figure 4-11 Force vs. current with position fixed, at room temperature

The position stiffness is approximately 66 lb/mil (twice that of the value seen in Figure 4-10 due to 2 load cell measurement) for this room temperature test. For comparison, Dr. Kenny predicted position stiffness equal to 66 lb/mil at 1000°F. The current stiffness is approximately 50 lb/amp for this room temperature test. For comparison, we predicted position stiffness equal to 40 lb/amp at 1000 °F. A high temperature test was performed and the results are given below:

- Temperature of permanent magnets = 920 °F
- Temperature of shaft = 660 °F

- Temperature of ceramic layer covering the poles = 690 °F
- Force at 13.3 amps = 629 lb.

For comparison the measured room temperature force at this current level was 720 lb as shown in Figure 4-11. Figure 4-12, Figure 4-13, Figure 4-14, Figure 4-15, Figure 4-16 and Figure 4-17 show plots of Force Vs Current from the data gathered from different tests that were carried out.

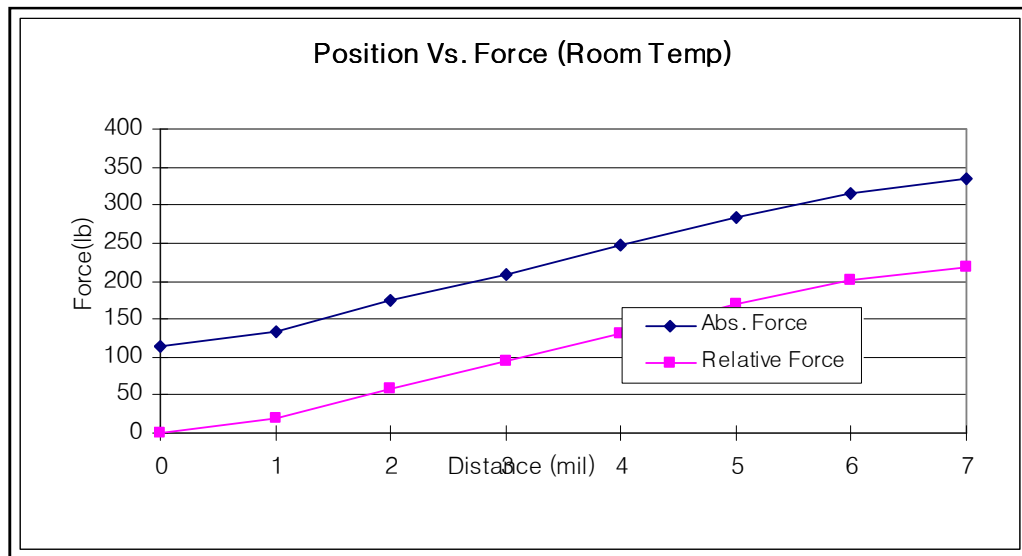


Figure 4-12 Force vs. current 1

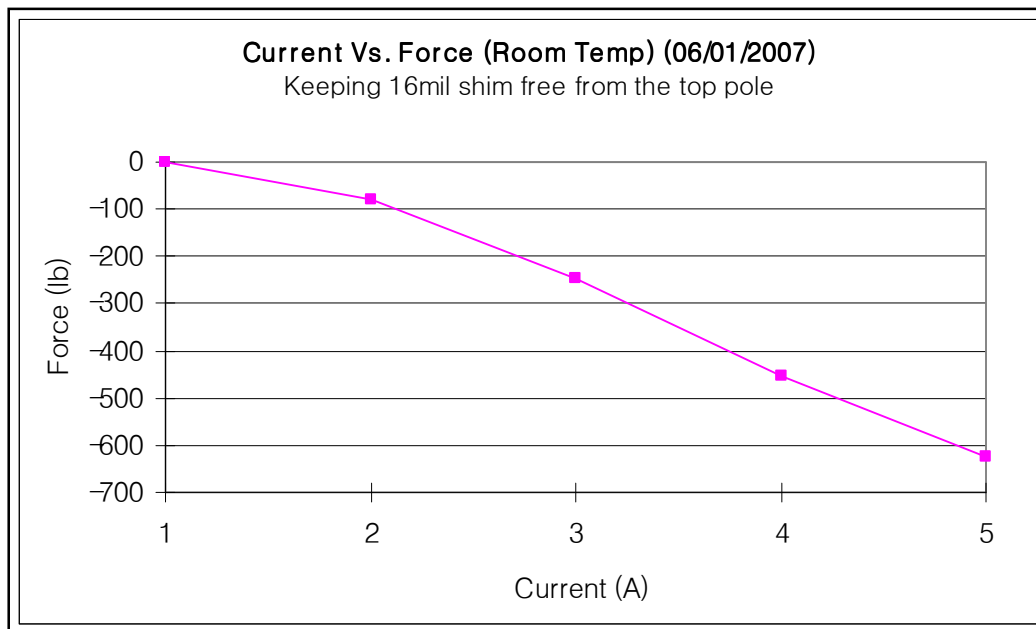


Figure 4-13 Force vs. current 2

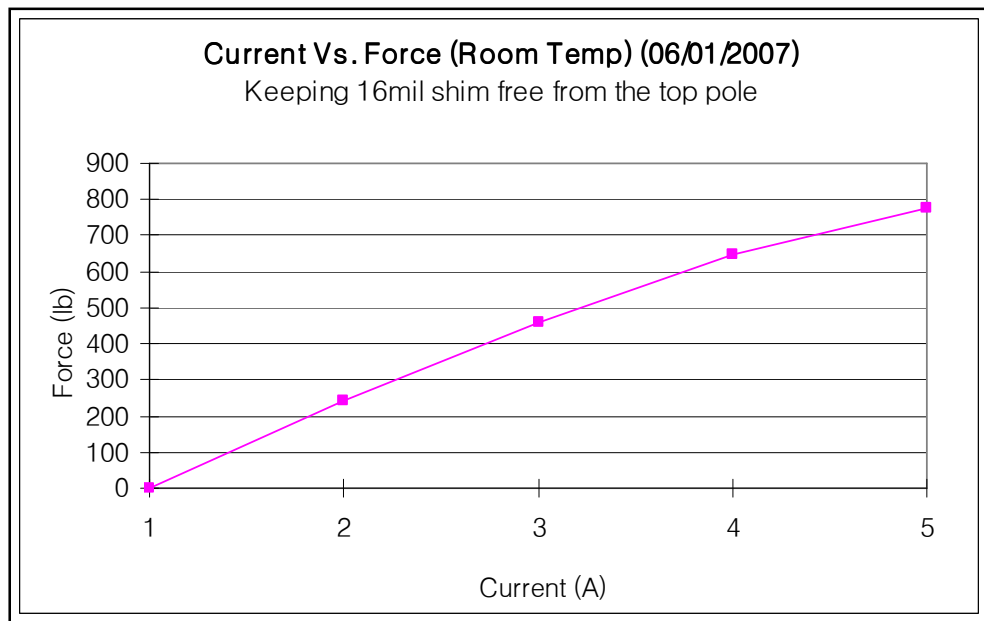


Figure 4-14 Force vs. current 3

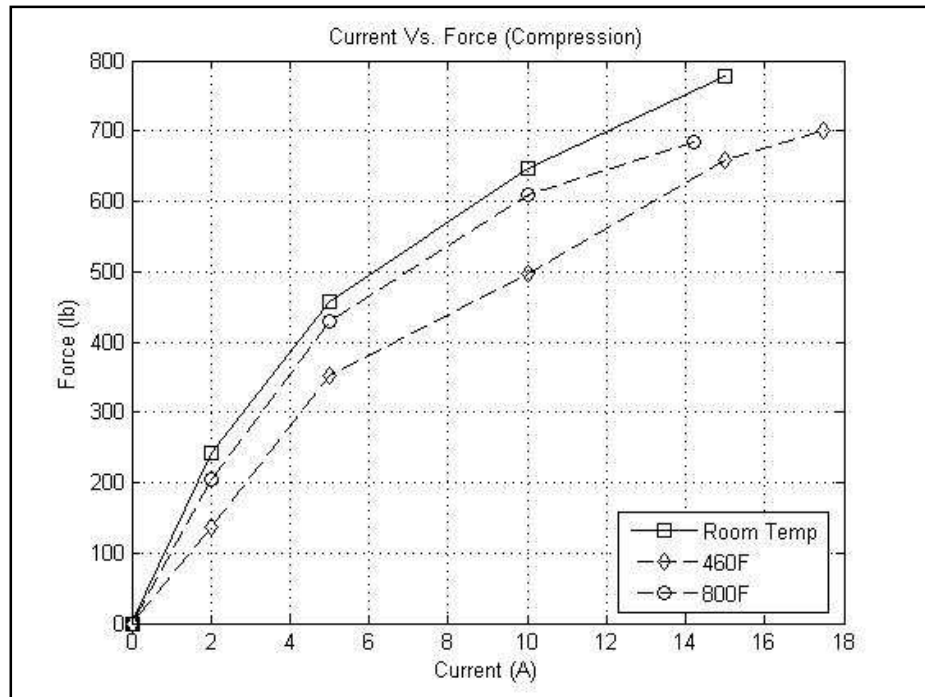


Figure 4-15 Force vs. current 4

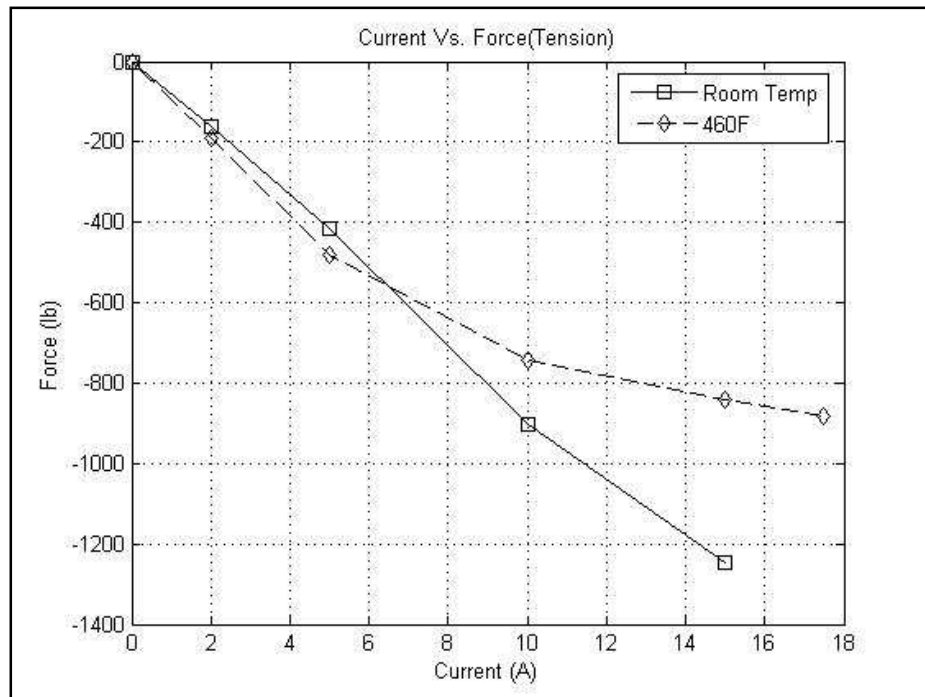


Figure 4-16 Force vs. current 5

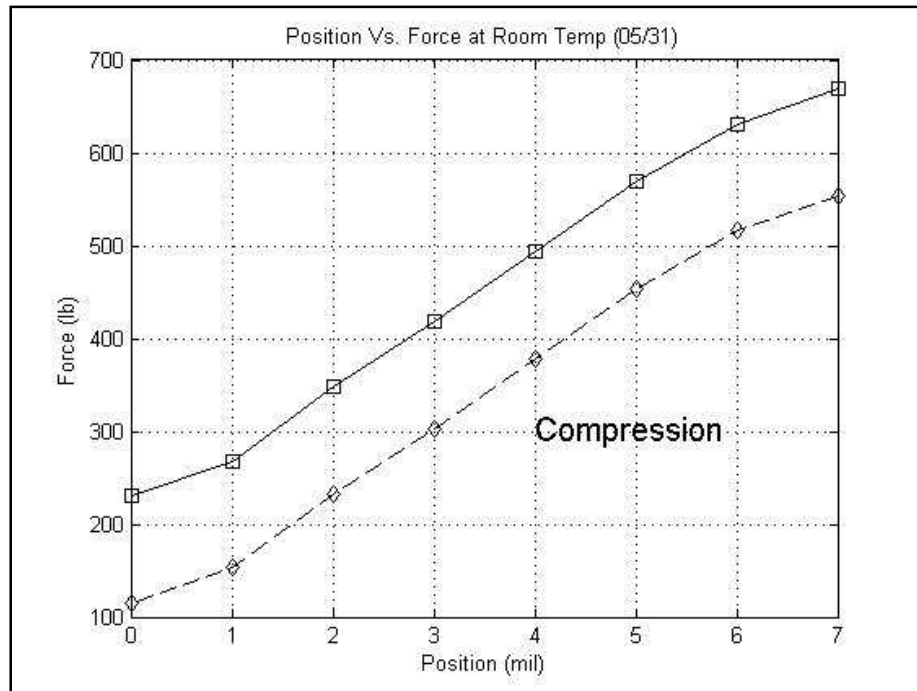


Figure 4-17 Force vs. current 6

4.3.3 *Radial bearing test results from rig with 4 load cells*

Comparison of test results with predictions and with the 2 load cell rig results are discussed in this section. Forces are measured with various current for the radial bearing at room temperature. Four load cells shown in Figure 4-18 are utilized to measure the radial bearing force. All twelve coils on two stators are energized with equal current, but the opposite polarity is given to the groups of top three coils and bottom three ones. 16 mil shims which are put in the gaps between the top / bottom poles and the shaft are kept free while forces are read from the four load cells. For the rest four gaps between the poles and the shaft, 13 mil shims are checked to be free.

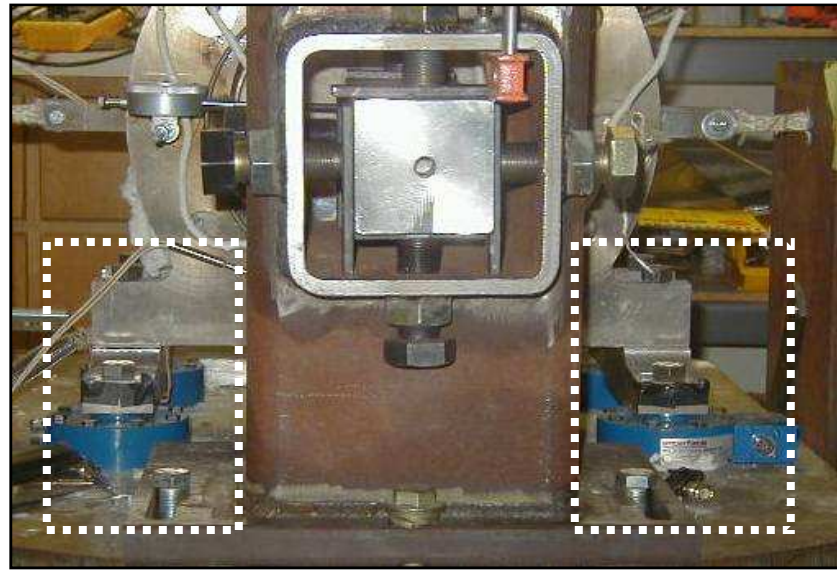


Figure 4-18 Radial bearing test rig with four load cells installed

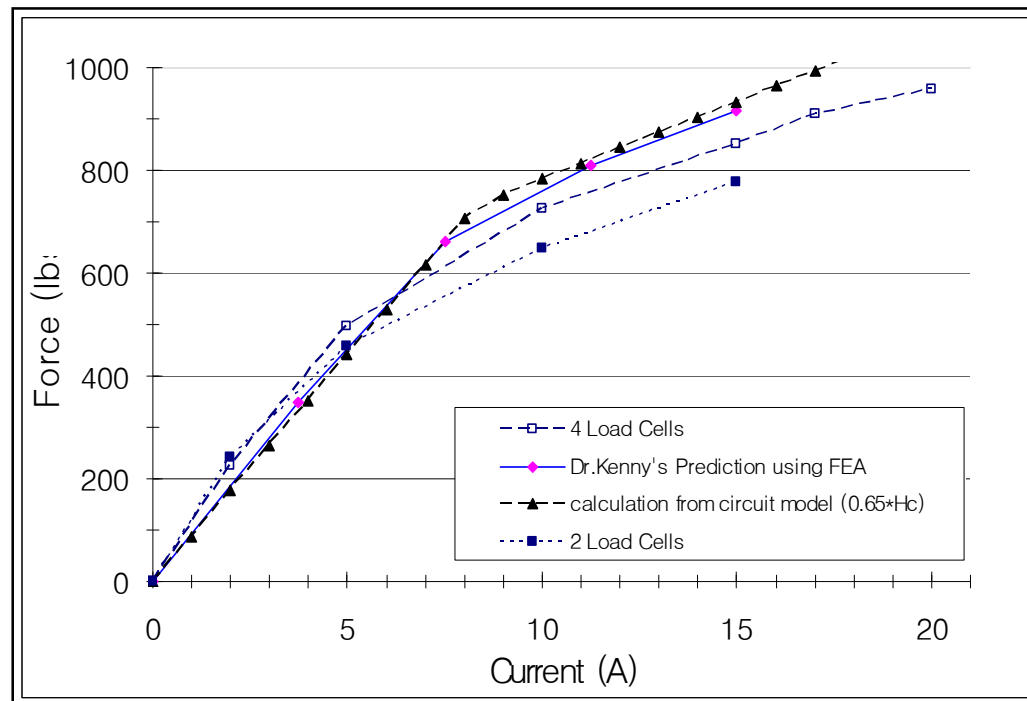


Figure 4-19 Force vs. current at room temperature

Figure 4-19 shows the comparison among the measured data, FEA, and the calculation from magnetic circuit modeling. The reduction of the force generated by the bearing with increasing temperature is due to:

- At higher temperatures the Air Gap between the rotor and the stator has increased. This causes the flux density, which is inversely proportional to gap, to decrease and consequently the force to decrease as it is a quadratic function of the flux density.
- The demagnetization of the magnet starts at higher temperatures. Hence, as the temperatures rise the magnets start to lose their magnetic strength.
- Changes in the properties of the magnetic flux path material (Hiperco-50).

4.3.4 *Bearing position and current stiffness*

For 1000 °F, the theoretical, 3D Finite Element, load capacity is 602 lb., position stiffness is 66 lb/mil and current stiffness is 40 lb/amp. Room temperature force vs. current with the shaft fixed and force vs. position with the current equal to zero yielded the stiffness shown below in Table 4-7.

Table 4-7 Position and current stiffness

Approach	Radial Bearing Position Stiffness lb / mil	Radial Bearing Current Stiffness lb/ amp
Measurement	66.0	50

5. FULL MAGNETIC BEARING TEST RIG

The EEC Universal Magnetic Bearing System will consist of 2 radial bearings, an axial thrust bearing and a high temperature motor. Figure 5-1 shows the schematic diagram of the main components off the test rig.

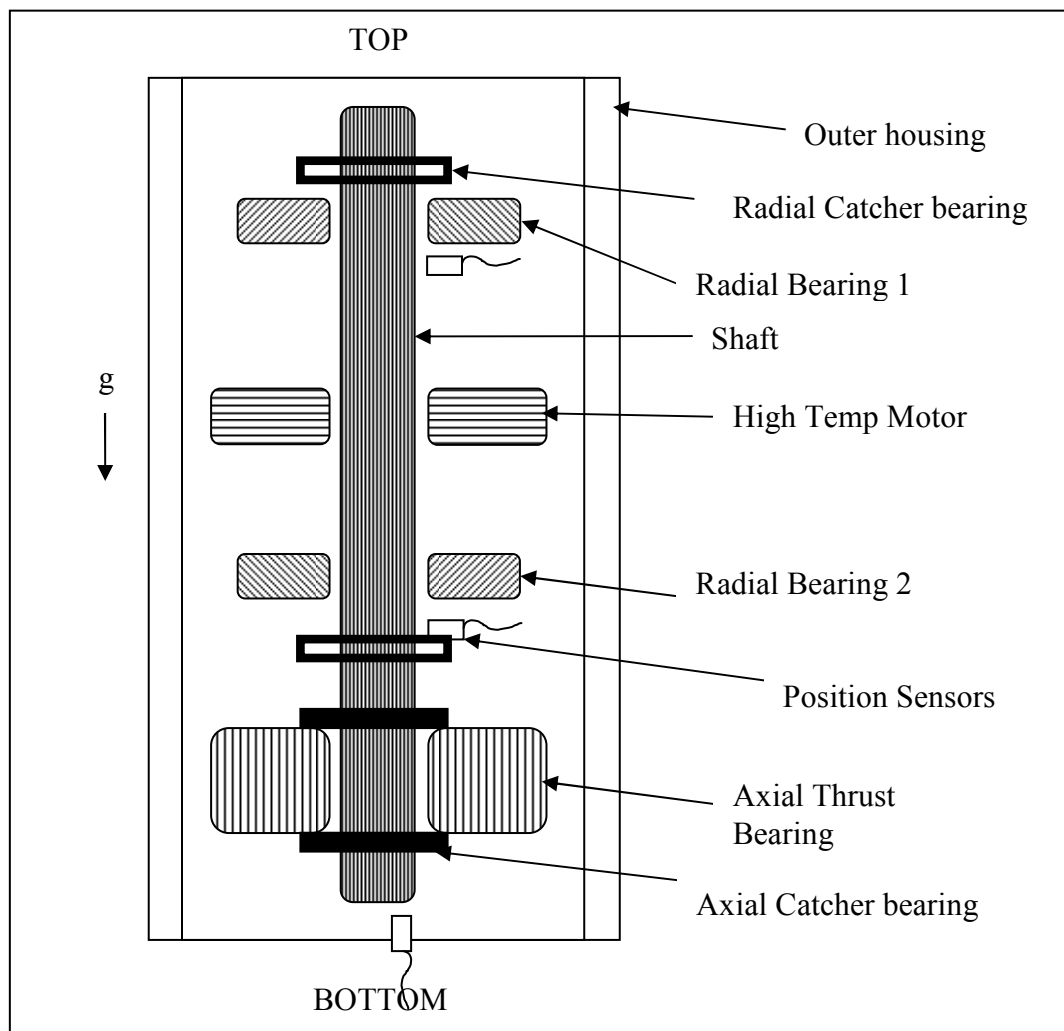


Figure 5-1 Schematic of universal magnetic bearing test rig

5.1 Axial Thrust Bearing Design

The thrust bearing has high temperature permanent magnets for bias flux. The major components are shown in Figure 5-2 below. It mainly consists of the following:

- Coils
- Magnets
- Thrust Rotor
- Thrust Poles
- Back-iron.

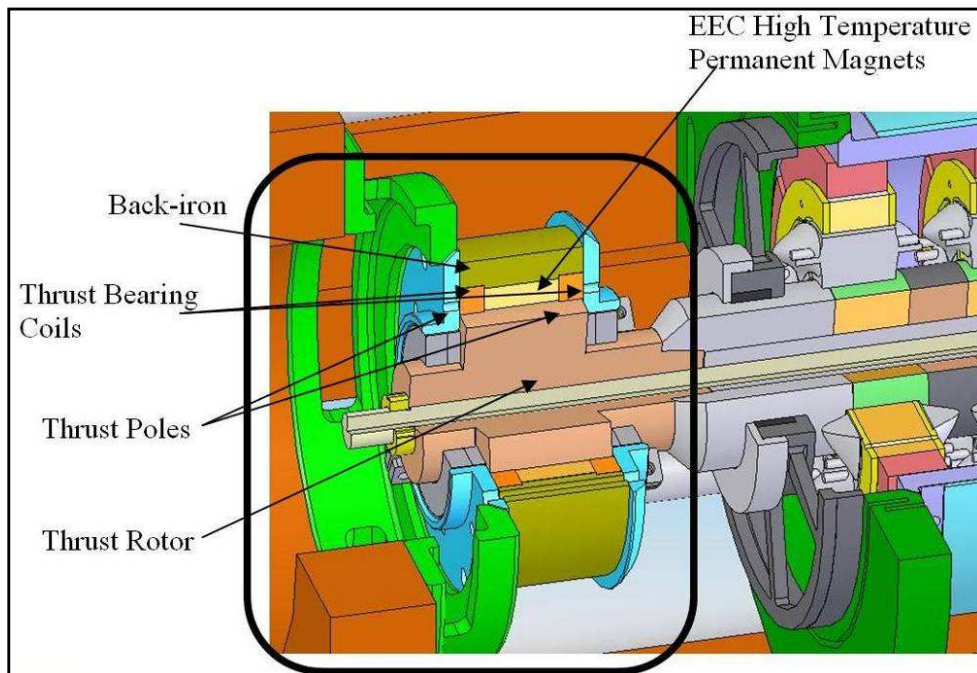


Figure 5-2 Thrust bearing components

The back-iron, rotor, and thrust disks are all produced from Hiperco-50. The end thrust poles and the back-iron is bolted together using holes in the back-iron. This assembly is

held on to the support structure using a hat flange. The catcher bearings are located on either side of the thrust poles. The Graph-alloy catcher bearings and their housing are shown in Figure 5-3. Figure 5-4 shows the actual Thrust bearing after potting.

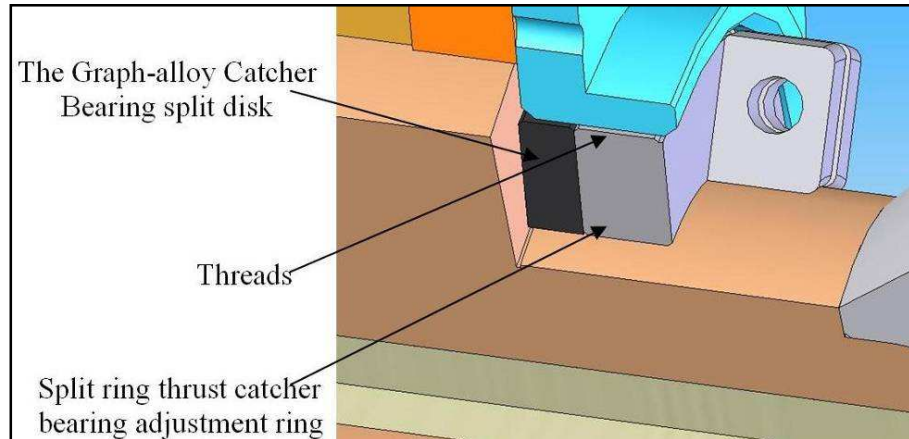


Figure 5-3 Graph-alloy catcher bearings



Figure 5-4 Axial thrust bearing

5.2 High Temperature Motor Design

The EEC motor is designed to produce power in the range of five to ten horsepower (3.75 KW to 7.5 KW). The top running speed is twenty thousand rpm. It is designed to be self starting with a standard three phase controller. Peak current and voltage drawn by the motor are ten amps and two hundred and thirty-five volts.

The EEC motor is compatible with the same rotating system as the EEC radial and axial bearings. It is a high temperature motor utilizing EEC high temperature T550 magnets capable of operating at one thousand degrees (538 C) and VCEL high temperature electric coils. The motor system is a PM brushless DC three phase 6 pole. Figure 5-5 shows the buried poles and the stator poles used in the brushless DC motor. The coils will be produced using the same techniques as were utilized in the radial bearings. The stator laminate stacks production will also be similar to the radial bearing laminate stacks.

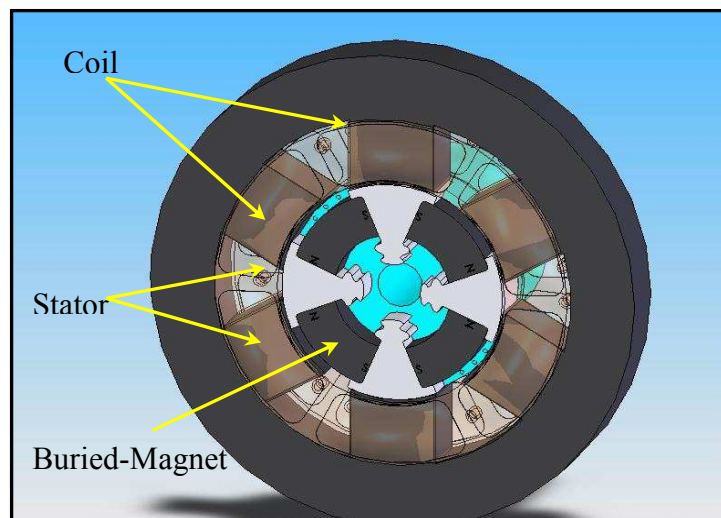


Figure 5-5 Buried poles in motor

The permanent magnets are located inside the rotor to prevent the magnets from being destroyed at the high temperature as well as during initial testing. Experience has shown that the magnets need to be protected as much as possible to prevent early failure. The rotor outer diameter has been kept small as possible to further reduce the stresses from rotation. Figure 5-6 shows the actual high temperature motor being tested.

The EEC axial thrust bearing and high temperature motor are being developed at TAMU-VCEL by Zhengxin Zhang. He is working on the control issues, reliability and power requirements of motor.

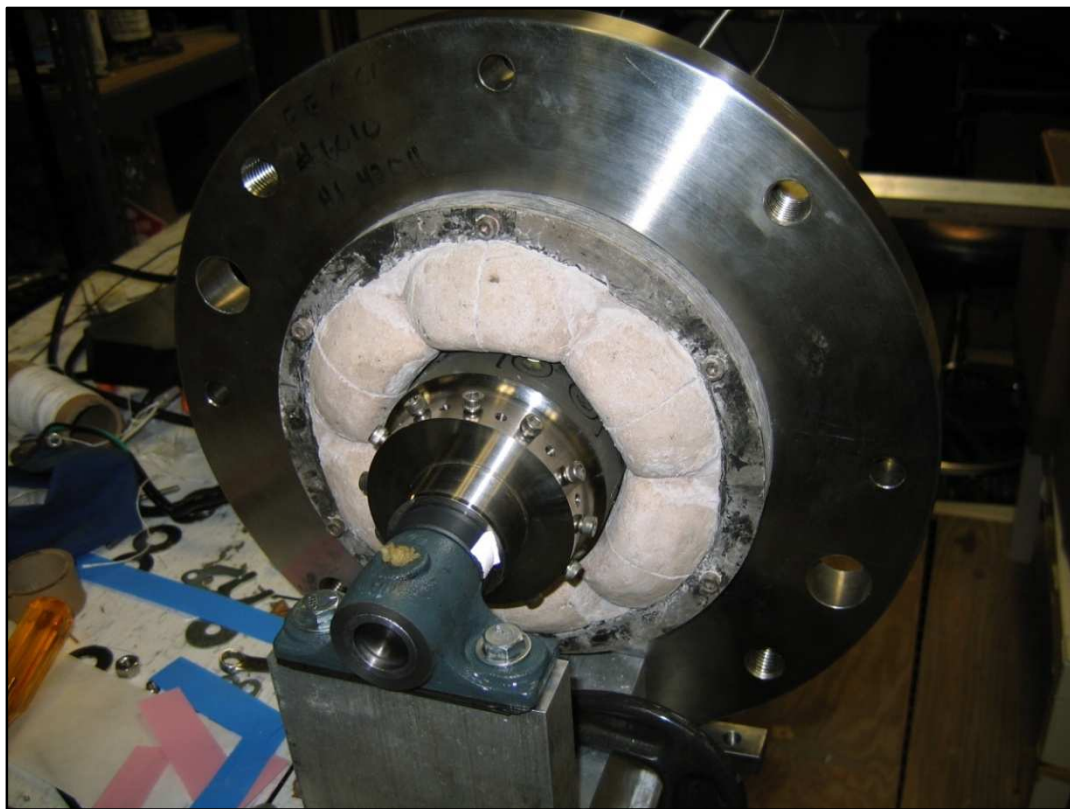


Figure 5-6 EEC high temperature permanent magnet motor

5.3 Shaft Design

The shaft assembly is comprised of 4 sub-assemblies – Axial thrust bearing, two radial bearings and the motor mounted of the shaft over different sleeves. The shaft is stepped at different locations to provide axial thrust and hence restrict the axial displacements. Relief grooves are incorporated in the design at the step locations to ensure mating of the faces during assembly. Shaft lock nuts are provided at the two shaft ends. A solid model and the cross sectional view of the shaft assembly is shown in Figure 5-7 and Figure 5-8 respectively.

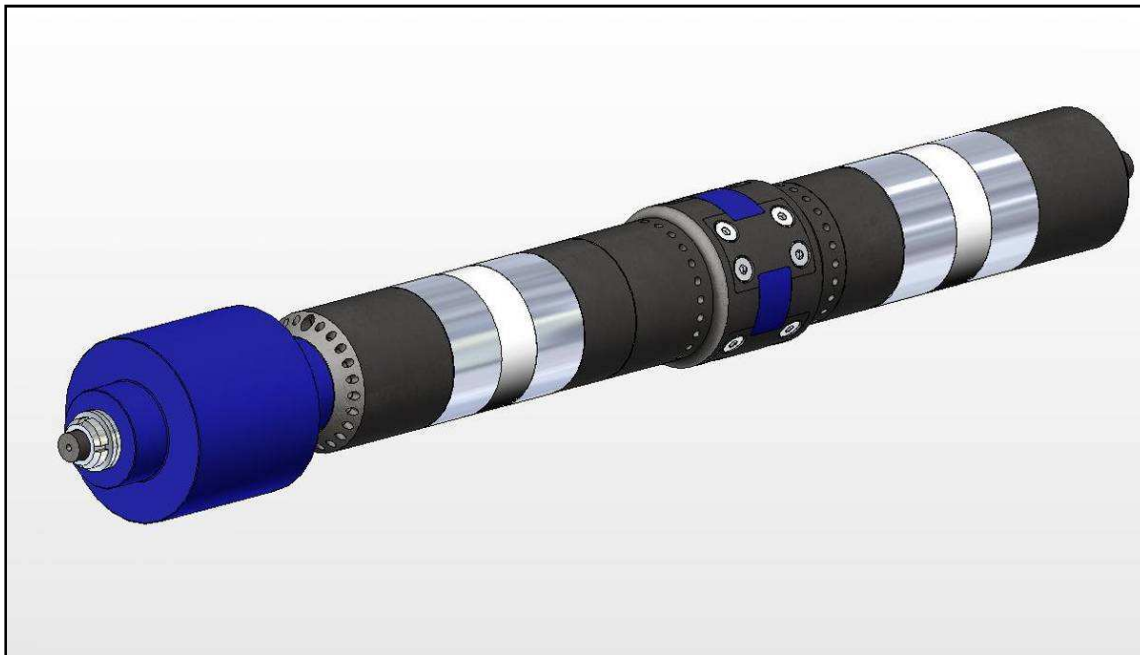


Figure 5-7 Solid model of the shaft

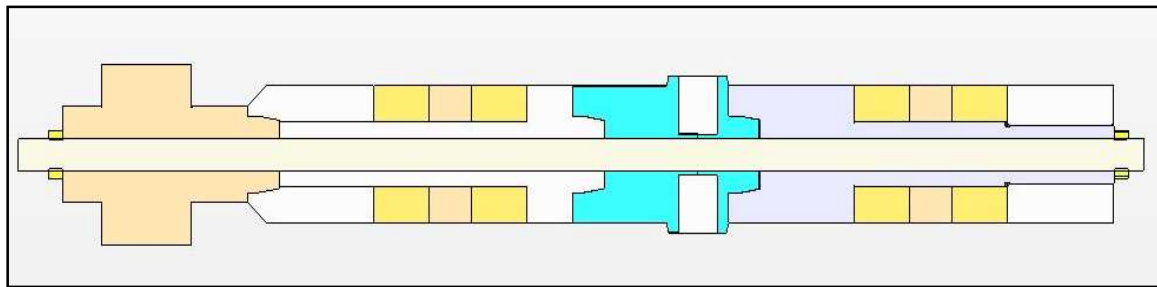


Figure 5-8 Cross-section of shaft assembly

5.4 Stress Analysis and Interference Fits

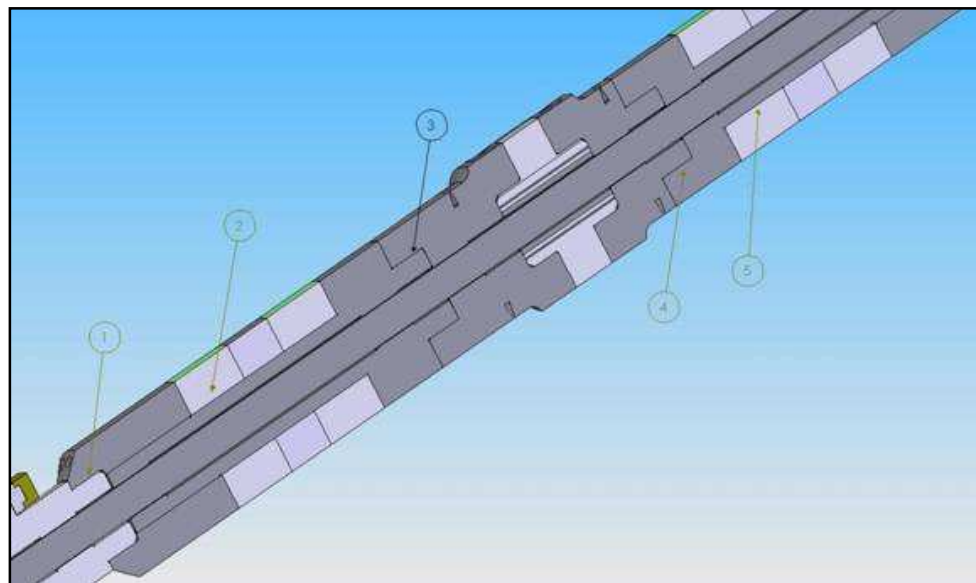


Figure 5-9 Locations with interference fits on shaft

Since the four shaft sections need to be put together and taken apart probably more than once, we needed to determine the lowest possible interference that should be

used (locations shown in Figure 5-9). The magnitude of the interference would decide the ease with which the shaft sections can be taken apart. But at the same time, this interference that would be applied at room temperature must not disappear at high temperature (1000 °F) and at high rotating speeds (20,000 rpm).

Although, the tie bolt holds the 4 shaft segments together, it is desirable to have some interference existing at full operating conditions at the sections shown in Figure 5-9. In order to do this kind of interference check, we needed material properties at high temperature, for the different shaft material, which are difficult to obtain.

With the best possible data set (Figure 5-10) for material properties a MATLAB code was executed to calculate the stress, slip forces, pressure, and interference. The results for one such analysis is shown below in Figure 5-11, Figure 5-12 and Figure 5-13.

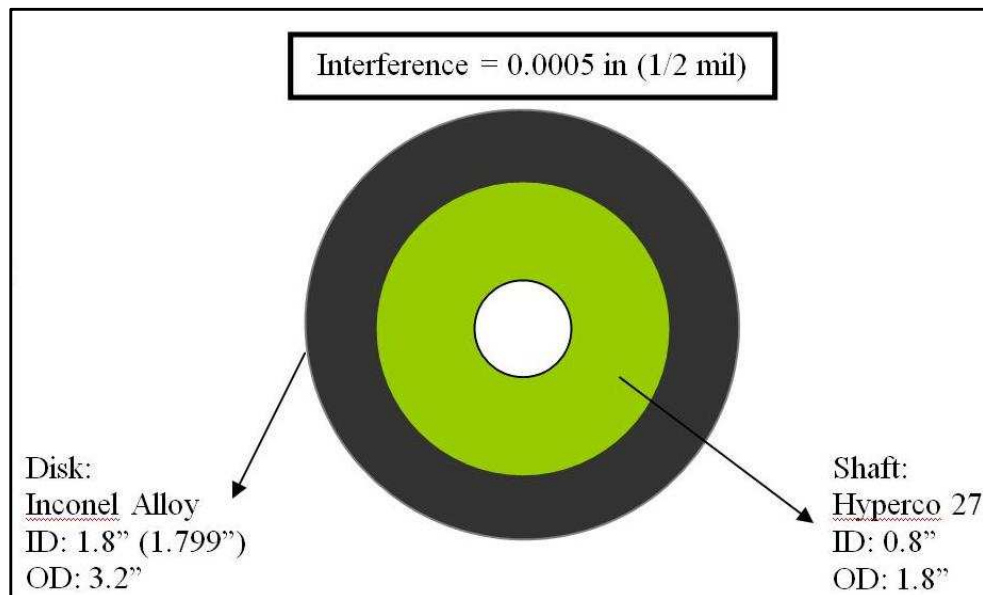


Figure 5-10 Schematic of the analysis

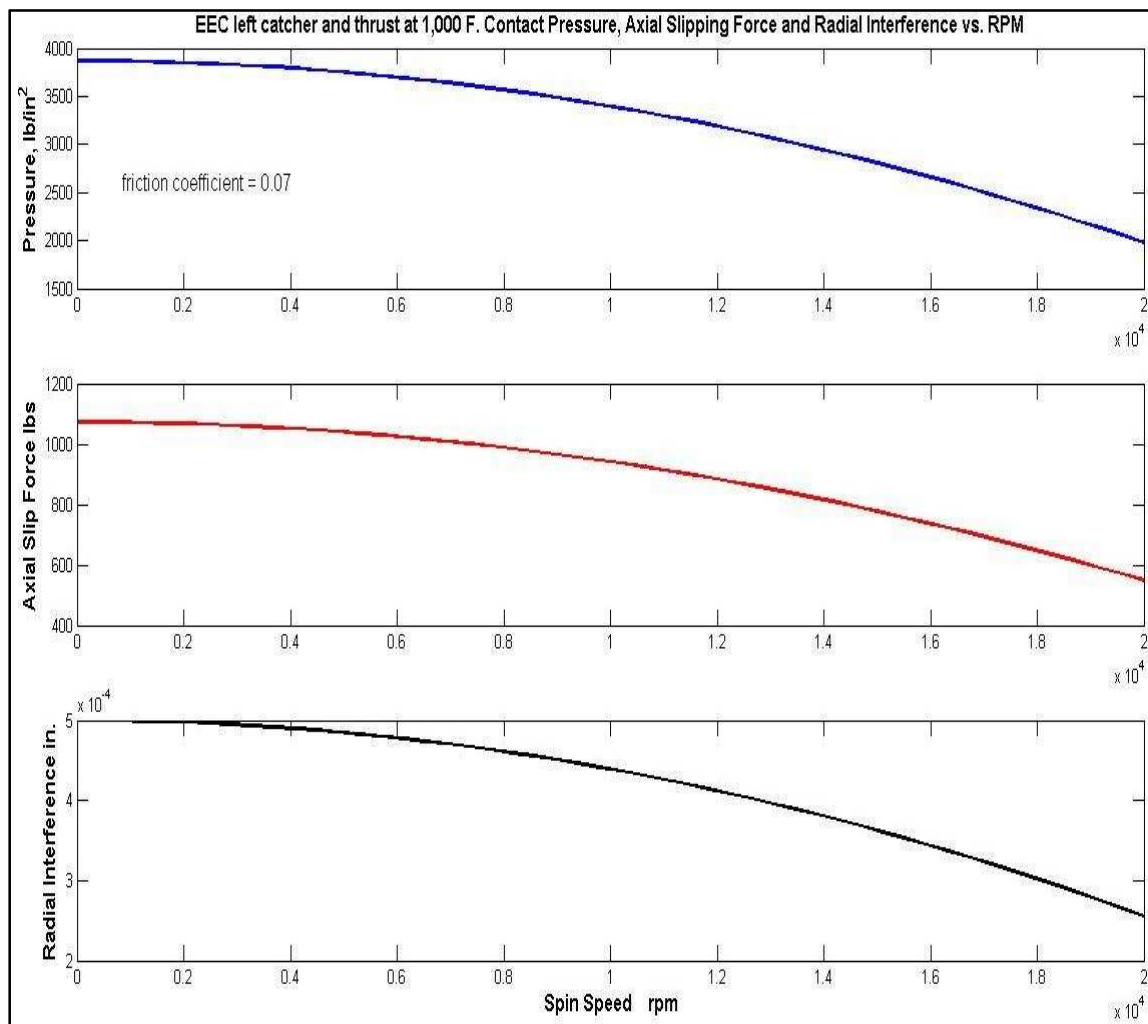


Figure 5-11 Radial interference vs. speed at 1000 °F

When the code was run for different values of interference we observed that interference between 0.5 – 1 mil was more than sufficient to sustain even at full operating conditions for this case. The 0.5 mil radial interference comes down to 0.25 mils only at 20,000 rpm. When the code was run for different values of interference we

observed that interference between 0.5 – 1 mil was more than sufficient to sustain even at full operating conditions for this case.

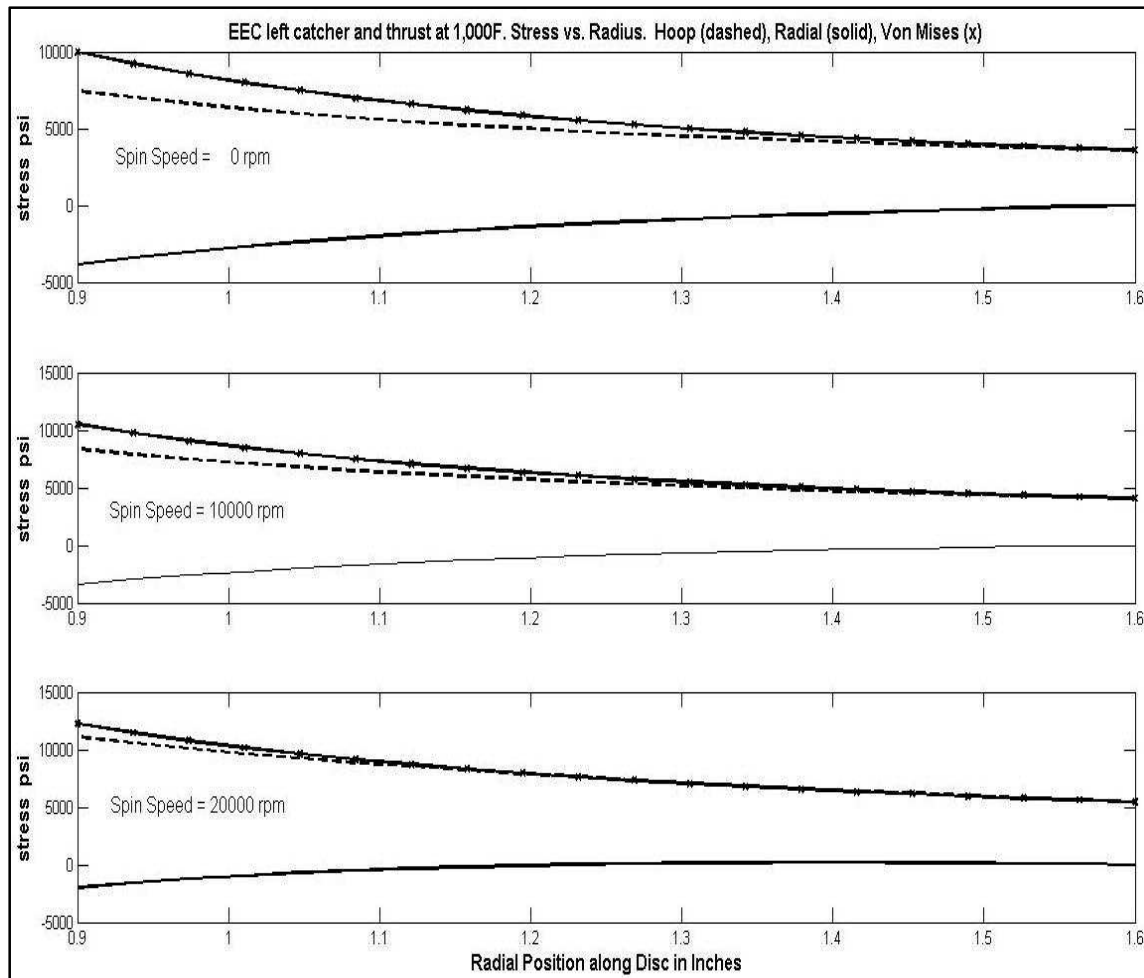


Figure 5-12 Stress vs. radial position for disk

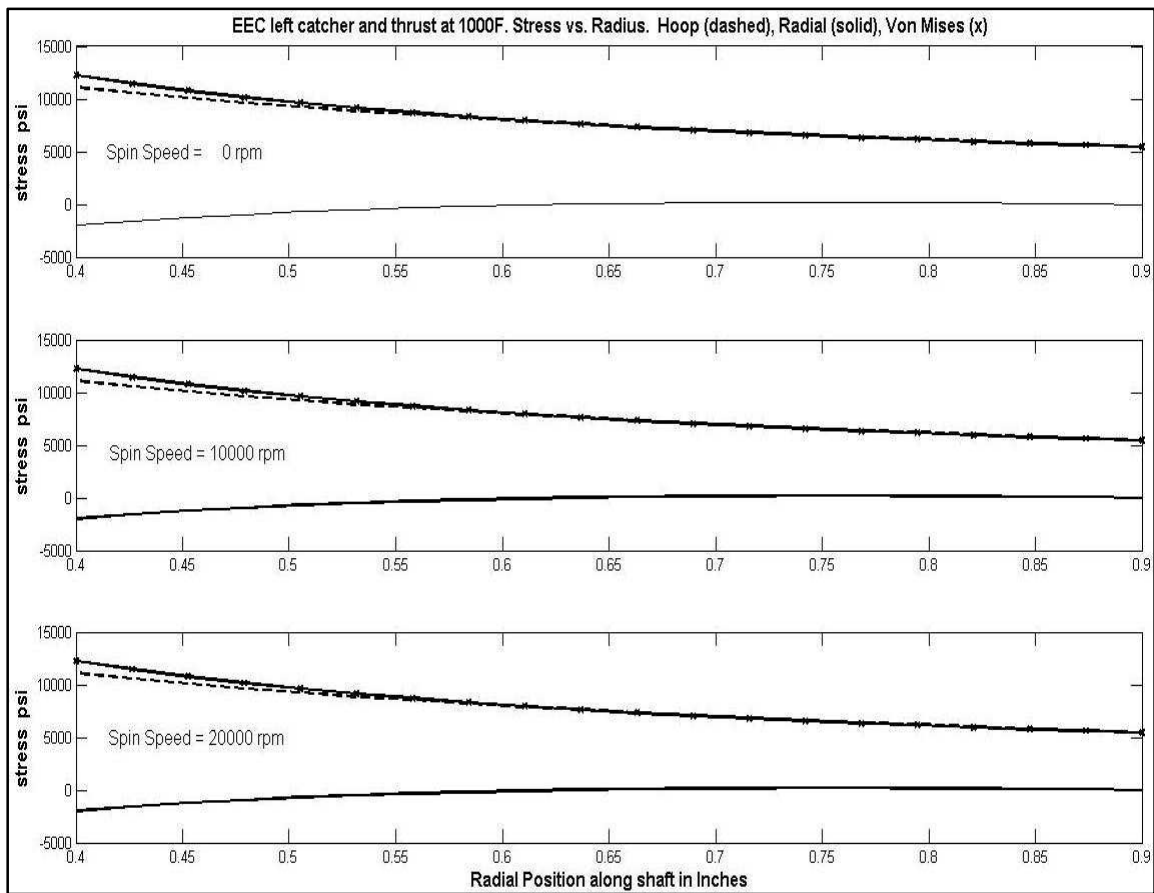


Figure 5-13 Stress vs. radial position for the shaft

The simulations were cross checked experimentally with a test setup. It consists of two mating members (see Figure 5-14) which are of actual shaft design size in terms of the diameter and made of the same material as the shaft (Inconel-718). The procedure to test the pieces was simple. The two pieces are put together at room temperature and then heated to a particular temperature and soaked for 2 hrs and then it is taken apart after cooling using a push out bolt.



Figure 5-14 Shaft test piece

Figure 5-15 shows the results of the test. It clearly shows the torque that is required to separate the shaft members almost exponentially rises with temperature. At 1000 °F the female part of the shaft had to be flash heated to separate the two members.

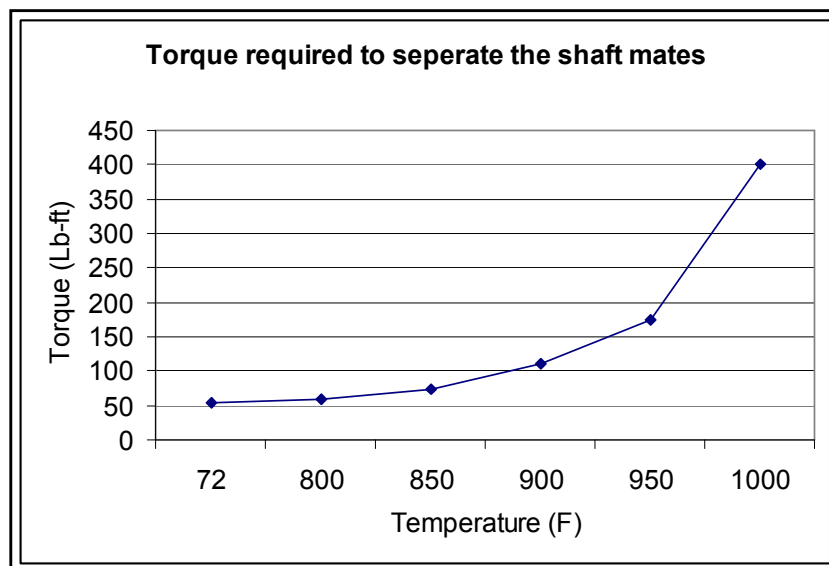


Figure 5-15 Torque vs. temperature

5.5 High Temperature Displacement Sensor Calibration

The testing was carried out using a test setup for mounting the sensor and also giving it fine vertical motion. First test results taken in the months of July and August 2007 with a 304-Stainless Steel target. The sensor is also checked with the actual shaft material as well, i.e. Inconel-718. Table 5-1 shows the sensor sets that were made.

The sensors have a sensitivity of 35-55 mV/mil. This sensitivity can be adjusted using the driver and changing the gain settings. There is also provision to bring the output out of the negative range to start at zero. All tests show a satisfactory amount of linearity at room temperature and at 1000 °F for the operating range (25-45 mils). The test setup and the sensor clamping mechanism in an oven are shown below in Figure 5-16 and Figure 5-17.

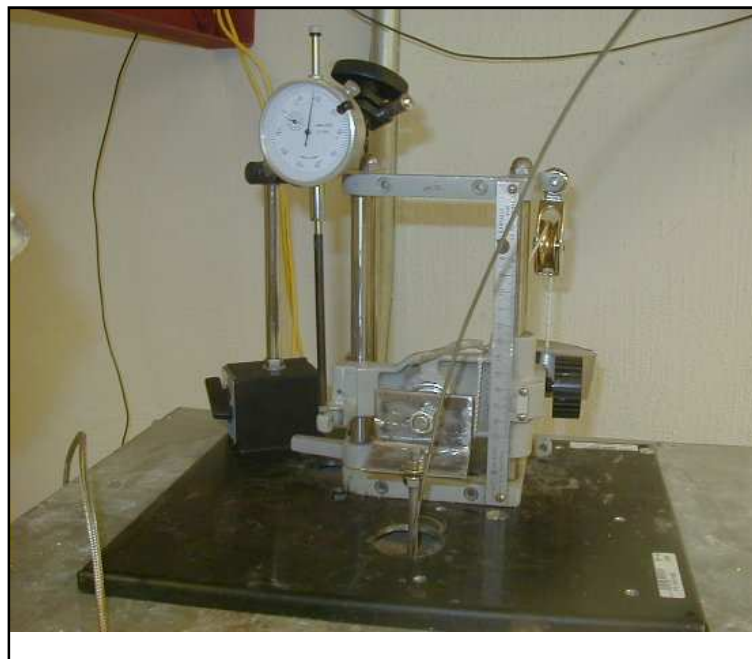


Figure 5-16 Test setup



Figure 5-17 Clamping mechanism for sensor



Figure 5-18 High temperature sensors after and before heat test

Table 5-1 Sensor channel sets

SET #	Sensor #	Cable #	Drive #	Drive Slot #	Rear Cable Connector #	Comments
1	S0121249-04-01	S0121249-01-04	9	1	1	Room Temp & High Temp
2	S0121249-04-02	S0121249-04-02	2	2	2	Room Temp & High Temp
3	S0121249-01-01	S0121249-01-02	3	3	3	Room Temp & High Temp
4	S0121249-01-02	S0121249-01-03	4	4	4	Room Temp & High Temp
5	S0121249-01-03	H0306162-01-01	5	5	5	Room Temp & High Temp
6	S0121249-01-04	H0306162-01-03	10	6	6	Full range within 40-45 mils
7	S0121249-01-05	S0121249-01-05	7	7	7	Room Temp & High Temp
8	S0121249-01-06	S0121249-01-06	6	8	8	Room Temp & High Temp
9	S0121249-01-08	S0121249-01-07	1	9	9	Room Temp & High Temp
10	S0121249-01-07	S0121249-01-08	8	10	10	Sensor Repaired and tested OK

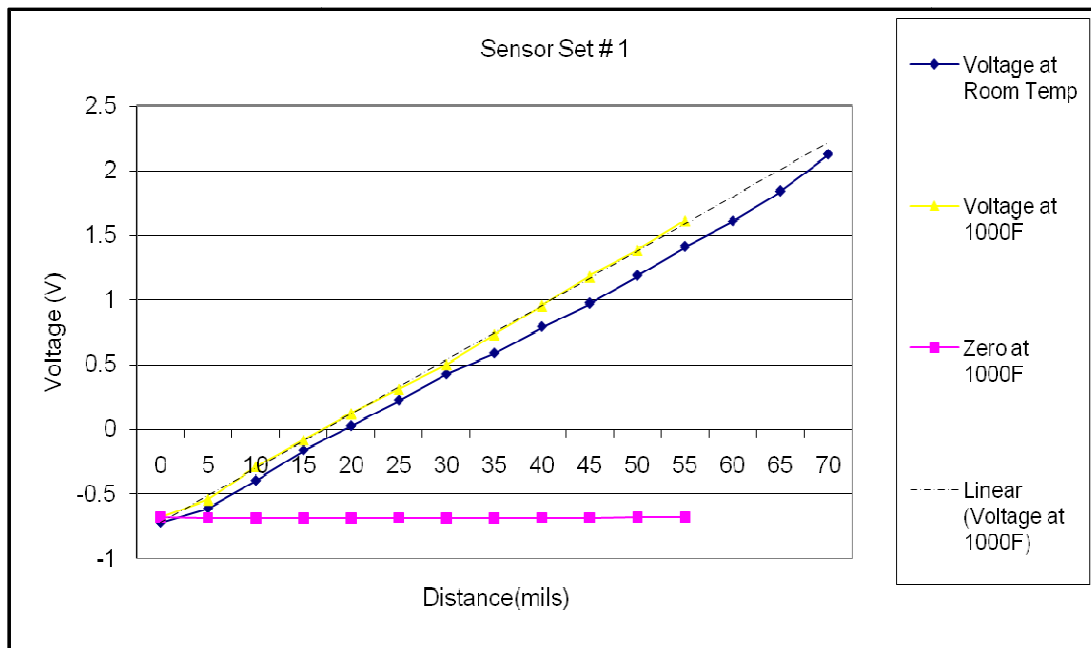


Figure 5-19 Channel 1

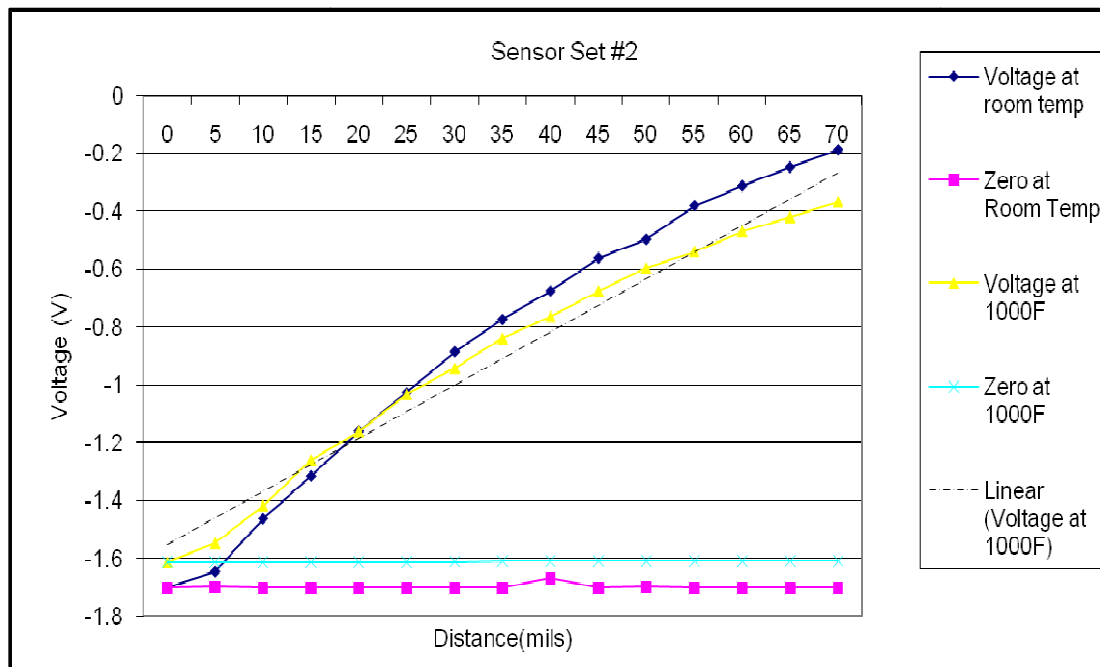


Figure 5-20 Channel 2

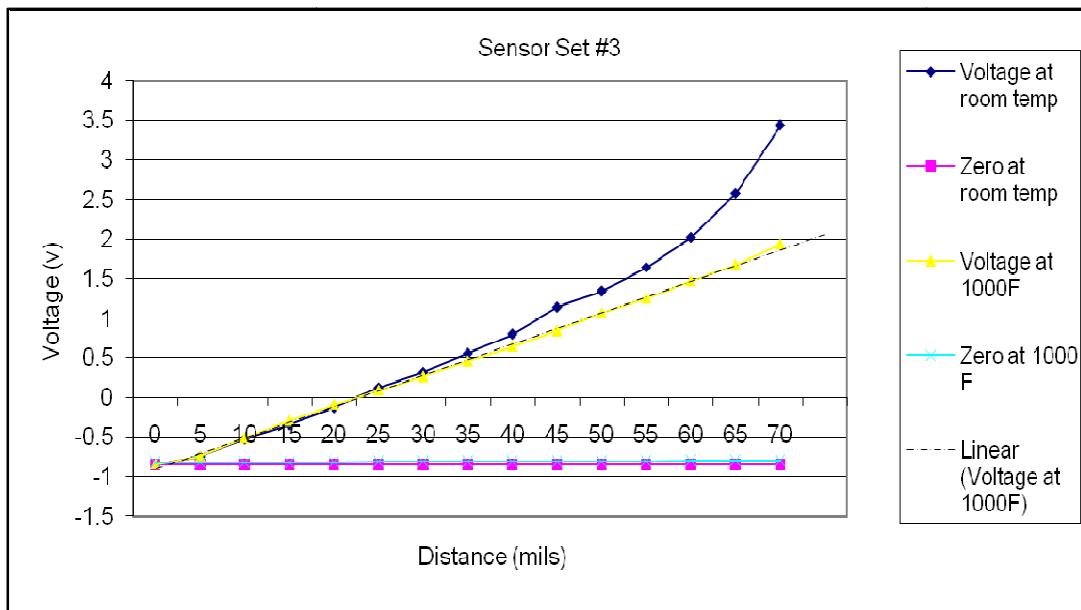


Figure 5-21 Channel 3

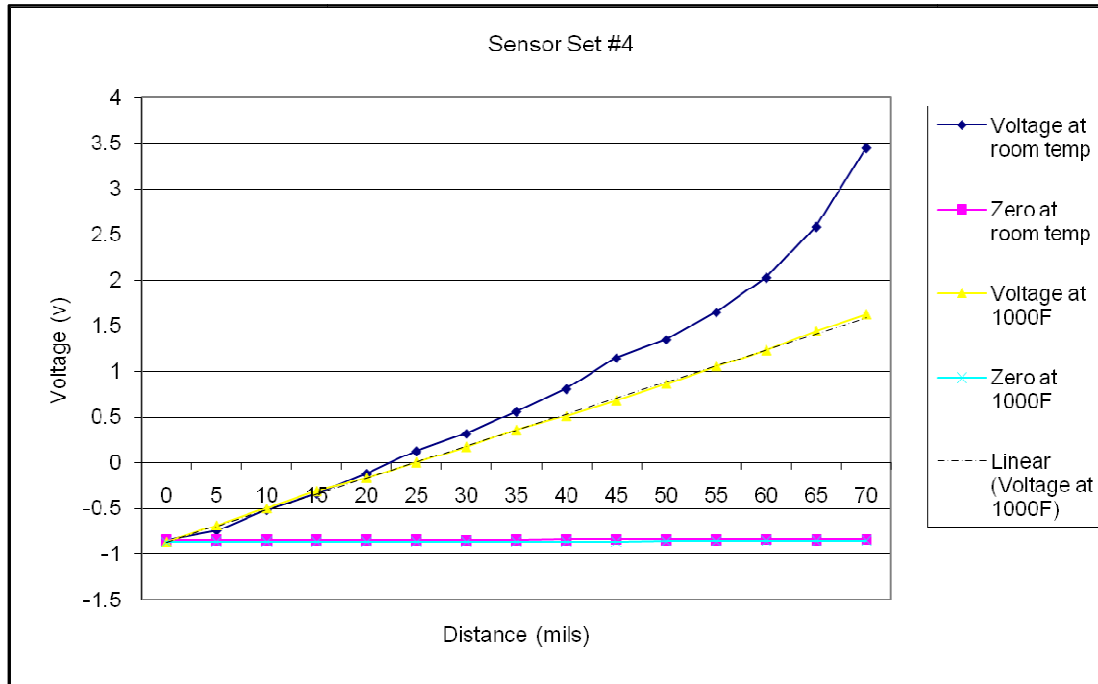


Figure 5-22 Channel 4

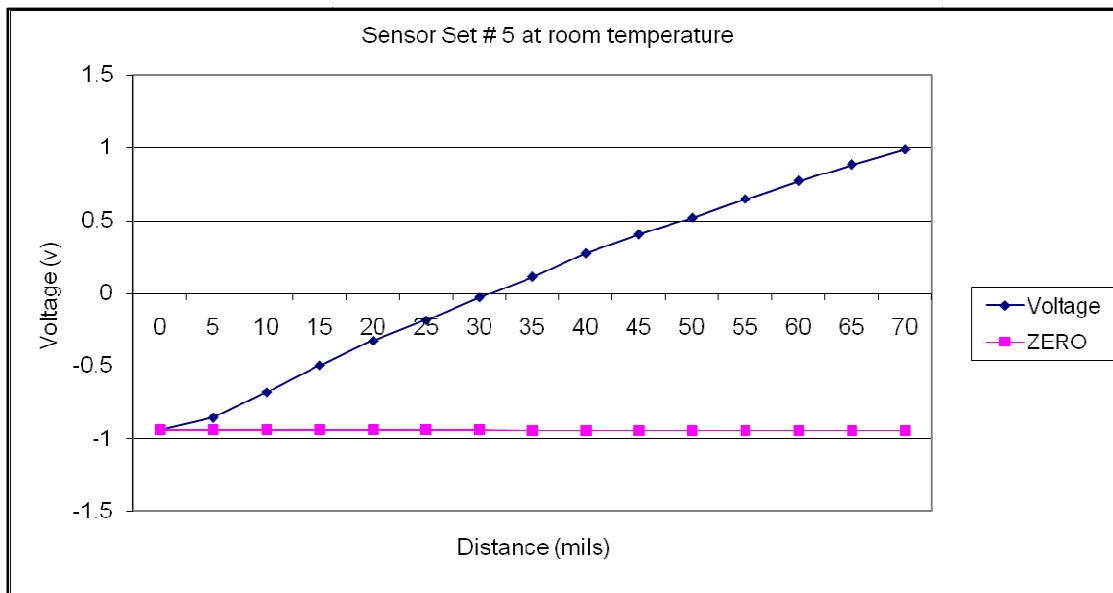


Figure 5-23 Channel 5

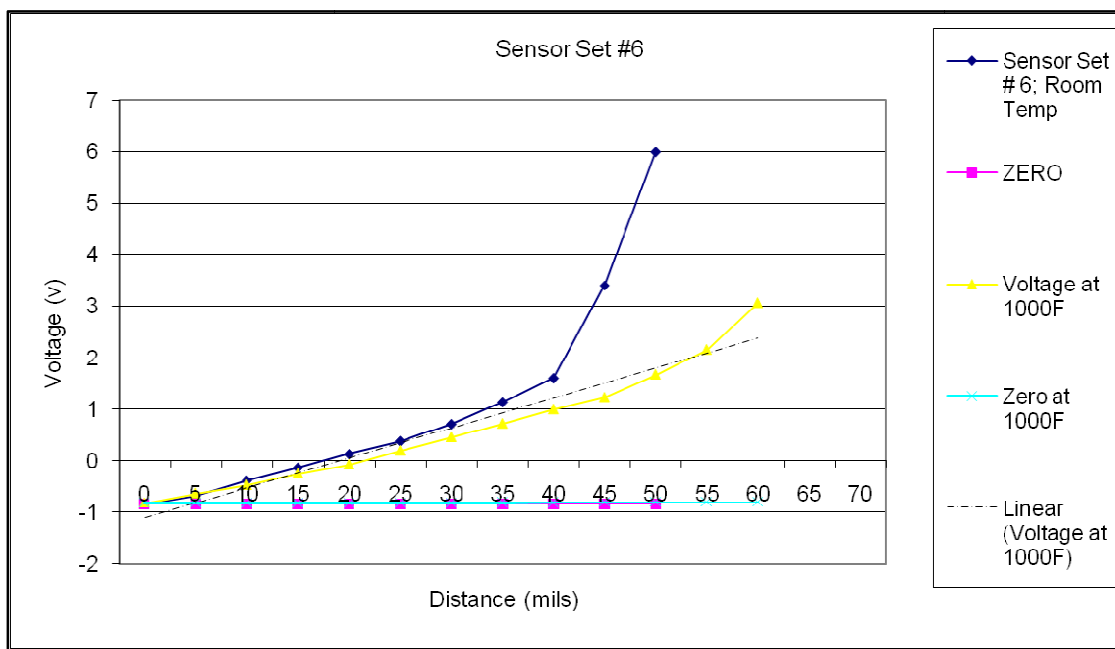


Figure 5-24 Channel 6

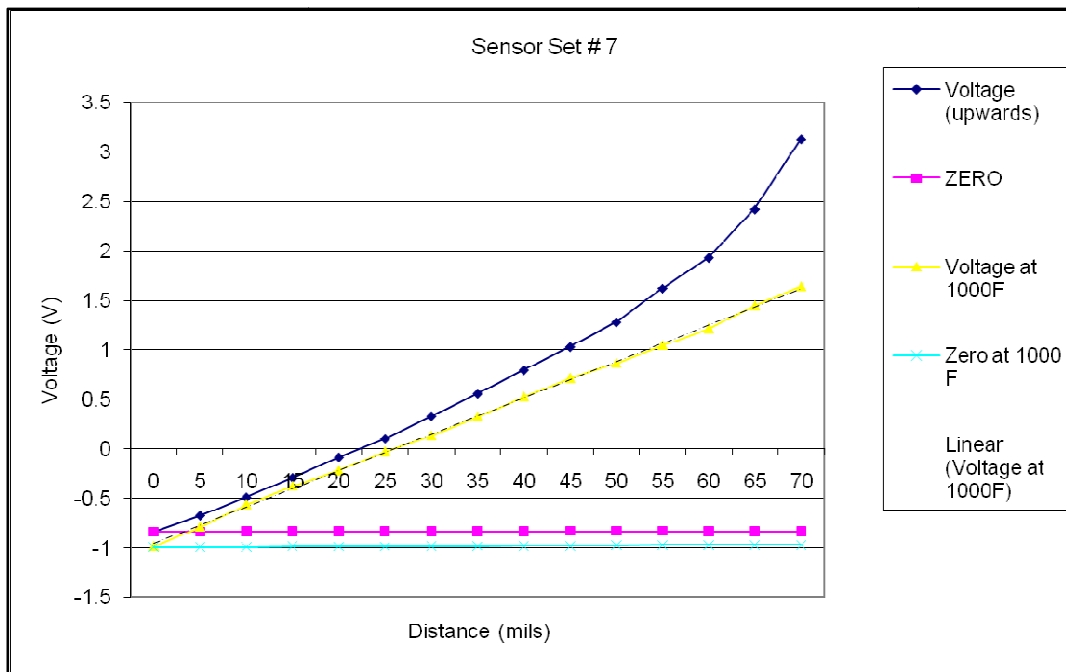


Figure 5-25 Channel 7

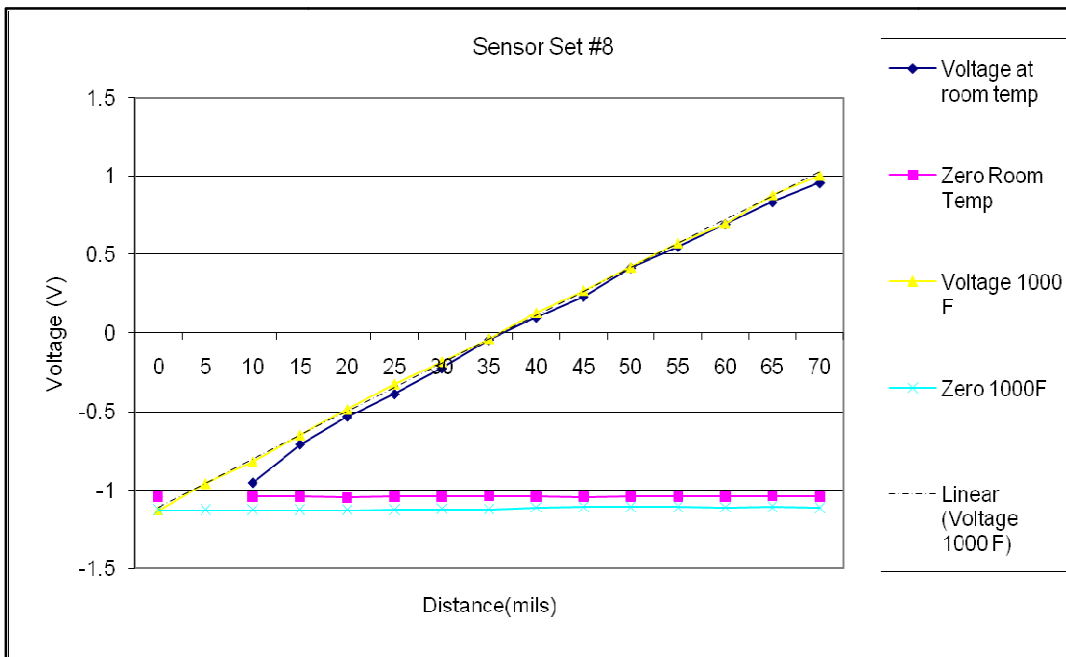


Figure 5-26 Channel 8

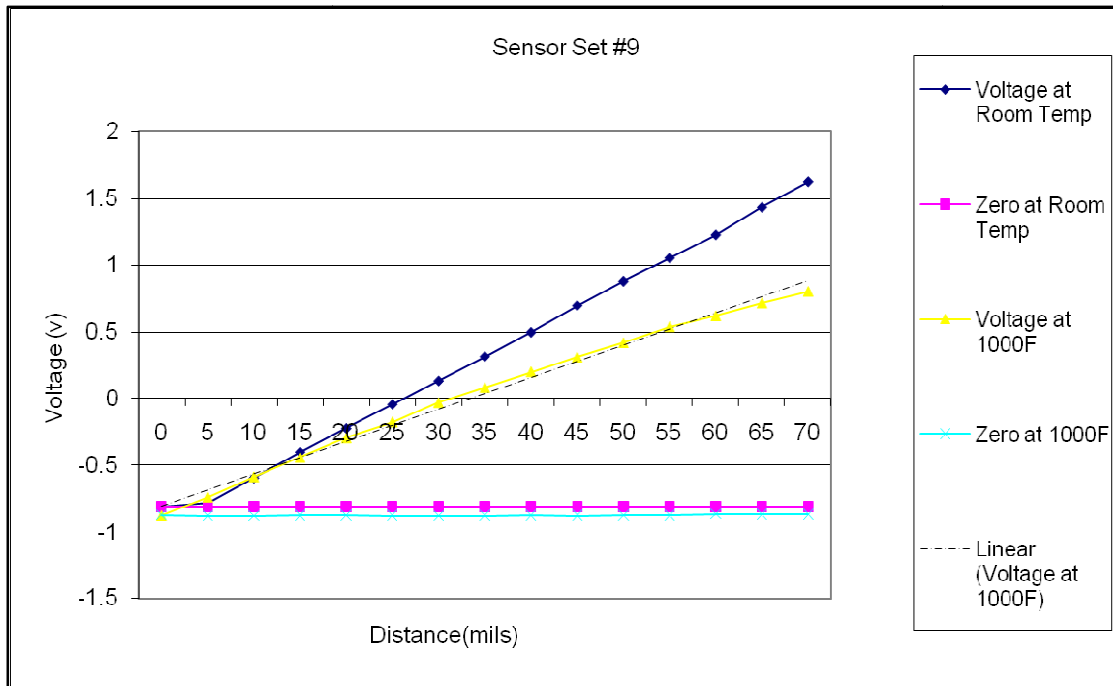


Figure 5-27 Channel 9

The results of the testing is shown in the above plots (Figure 5-19, Figure 5-20, Figure 5-21, Figure 5-22, Figure 5-23, Figure 5-24, Figure 5-25, Figure 5-26, Figure 5-27). From the results above we also plot a reduced set data that would be just in the operating range which is to be 25-45. Figure 5-28 and Figure 5-29 show that the sensors are fairly linear within the application operating range.

Further tests were done taking the actual shaft material as a target to check if changes in target material caused variations in the output. Inconel-718 was the target material sample that was used in these tests. The results (Figure 5-28 and Figure 5-29) show that the gain and linearity of the sensor output remained similar to that of the SS-304 target tests.

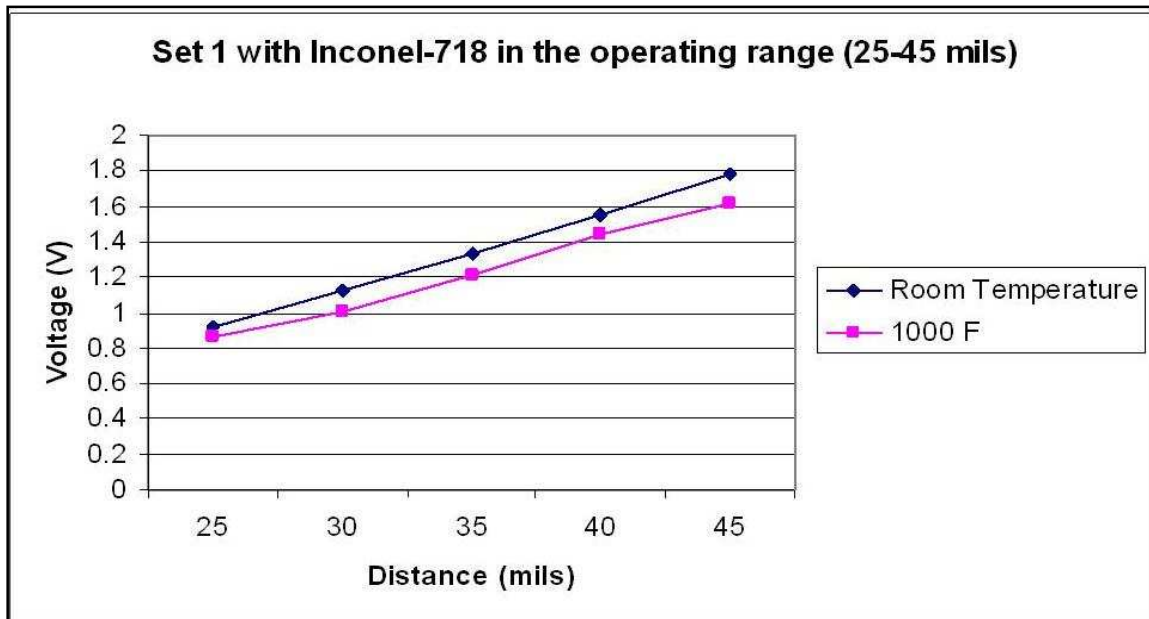


Figure 5-28 Channel 1 in operating range



Figure 5-29 Channel 1 in full range

5.6 Heating and Insulation Setup

In order to reach the desired temperature of 1000 °F as quickly as possible and at the same time provide uniform heating to the entire motor and bearing system, many different heating mechanisms were studied. A short calculation to determine the power required to heat the system was done in order to fix the wattage required on the heaters. The Calculations are shown below. We consider the heat required for raising the temperature of the system at start-up and the heat losses as the major governing factors to determine the total heat energy required to be supplied. The primary equation used is:

$$\text{Start-up Watts} = Qa + 2/3(Ql) + \text{Safety Factor}$$

Where, 'Qa' is the watts required to raise the temperature of the material and equipment to the operating point, within the time desired and 'Ql' is the watts lost from surfaces by conduction, convection and radiation. During start-up of a system the losses are zero, and rise to 100 percent at process temperature. A good approximation of actual losses is obtained when heat losses (Ql) are multiplied by 2/3 [14]. The *safety factor* was taken to be 25% for our purposes.

$$\text{Equation for 'Qa' (Absorbed watts): } Qa = \frac{W \times Cp \times \Delta T}{3.412 \times \text{Time}}$$

Where,

- W = Weight of the material (lb)
- Cp = Specific heat of the Material (BTU/lb. F)
- ΔT = Temperature Rise (°F)
- Time = Start-up or Cycle time (Hrs)

$$\text{Equation for 'Ql' (Lost watts):}$$

$$Ql = Ql1 + Ql2 = \frac{K \times A \times \Delta T}{3.412 \times L} + A \times 144 \times Fsl$$

Where,

- $Ql1$ = Surface Heat losses due to Conduction via the Insulation (W)
- $Ql2$ = Surface Heat losses due to combined Convection and Radiation (W)
- K = Thermal Conductivity of the Insulation Material (BTU.in/ft² . °F.hr)
- A = Surface Area of the Insulation (ft²)
- ΔT = Temperature Differential to Ambient (°F)
- L = Thickness of the Insulation (in)
- Fsl = Combined Convection and Radiation heat loss factors (W/in²)

Table 5-2 Parameters used to determine heat requirements

Weight of the material (W)	1075 lb	
Specific Heat (Cp) for SS – 304 and Inconel 718	0.11 BTU/lb.F	
Cycle Time Used	2.00 hrs	
Thermal Conductivity of the Insulation Material (K) Zircar Alumina-Silica Type ECO – 1200A	0.4 at 392 °F 0.85 at 1112 °F 1.4 at 1832 °F	BTU.in/ft ² . °F.hr
Surface Area (A)	29.45 in ² (4240.8 ft ²)	
Thickness of the Insulation (in)	1.00 in	
Combined Convection and Radiation heat loss factors for vertically mounted surfaces (Fsl)	1.08 at 1000 °F	

Taking conservative estimates of the parameters that were not exactly known such as weight and surface area the heat requirements are calculated. Table 5-2 shows the values of the parameters used to estimate the heat requirements.

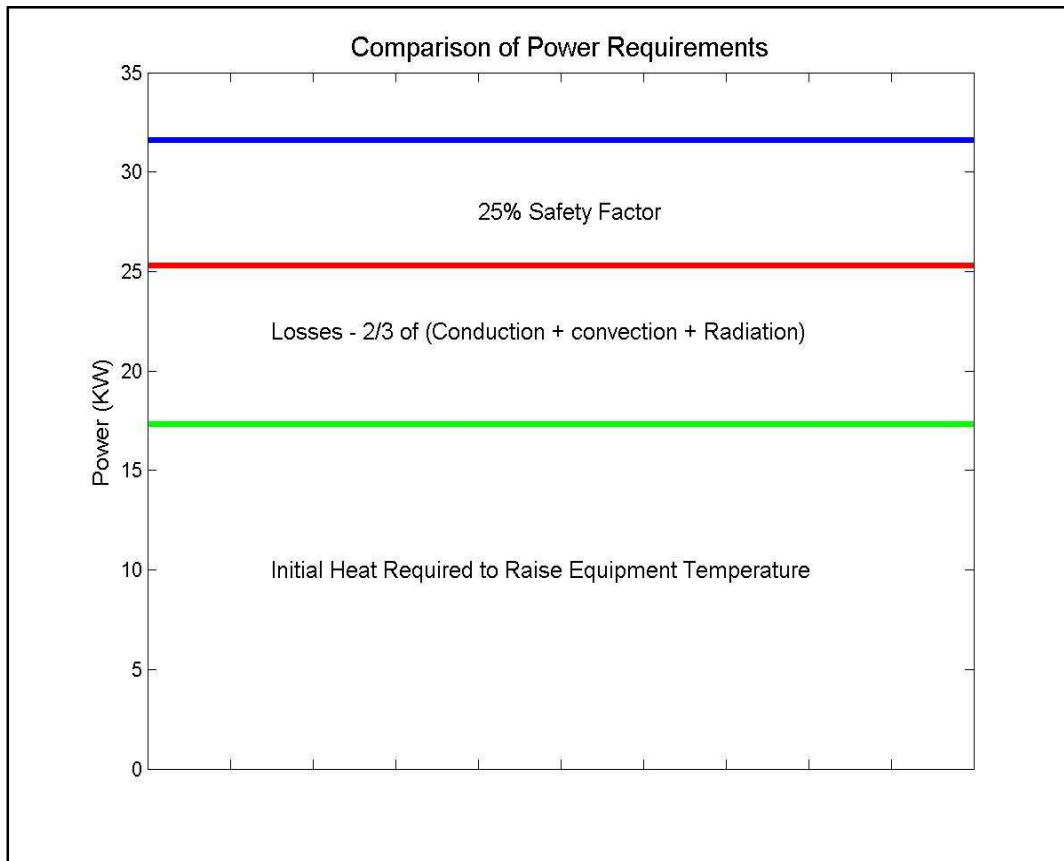


Figure 5-30 Estimates of power requirements for the system

Hence by calculation, we get the start-up watts to be roughly equal to 25.2 KW . Hence to supply this level of energy the following setup was finalized in order to heat the system. The heating setup is designed to give 33400W ($\sim 34\text{ KW}$). The three band heaters provide a total of 23.4KW which should be sufficient to provide for the heat

required in terms of watts. The 25% additional safety factor is provided by the four radiant heaters which together give out 10 KW . This system hence draws about 140A of current to generate the desired wattage. Figure 5-30 shows the power requirements estimated. Figure 5-31 and Figure 5-32 show the variation in power lost due to insulation surface conduction, convection and radiation.

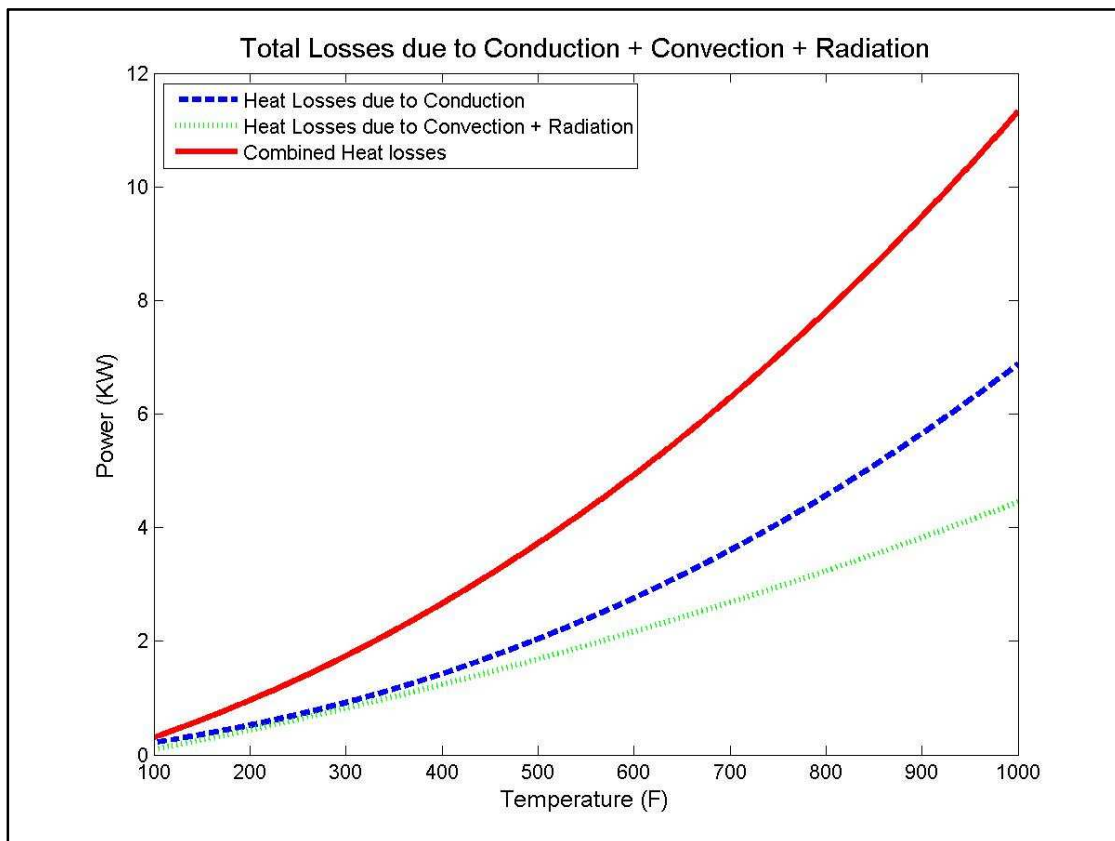


Figure 5-31 Estimation of heat loss

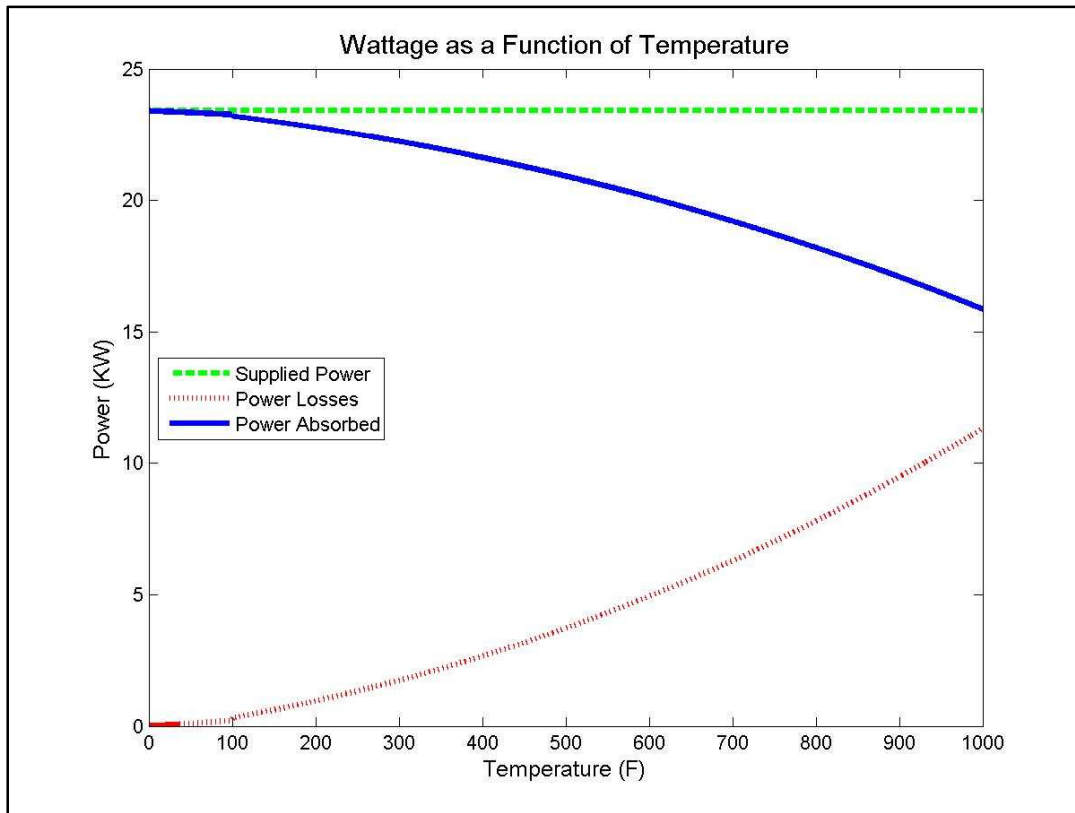


Figure 5-32 Power delivered with respect to temperature

Based on the above estimates the following heating system is used:

1. Three Watlow Mineral Insulated (M.I) Band Heaters

Specification: MI Band; 16.5in. ID x 4in. Width; 2 piece split.

240V/3900W Per Half; with a J type Thermocouple

96in. T/C and Heater Leads with loose braid

Spring loaded Tig Welded Barrel Nuts.

Maximum Temperatures: *1400F*

2. Four Watlow Ceramic Fiber Radiant Heaters

Standard configuration – VF606A24U – 24in.L x 10in.W x 2in.D

240V / 2500W per radiant heater

Maximum Temperature: *1800F*

3. Controller : Watlow CLS216 Multi-Loop Temperature Controller

Closed-loop PID control of up to 16 heat and cool loops (2 loops of Radiant

Heaters and 3 loops of the MI Band heaters

The three band heaters will be mounted onto the big outer cylinder along its length and the four radiant heaters will be placed on the periphery of the motor and its housing. The band heaters are used as the primary heating source. The radiant heaters are only a secondary or a backup to boost the temperature in case the temperatures do not rise quickly. The plot (Figure 5-33) shows that due to losses in the insulation the time taken to reach a 1000 °F temperature will be slightly longer than what was initially fixed. Calculations show that the time taken will be in the range of 2.00 to 2.50 hrs. Figure 5-34 shows the testing of the radiant heater so as to understand its functionality to better adapt it to our system. Figure 5-35 shows a model of the insulation panels along with the radiant heaters mounted onto the main support housing for the motor.

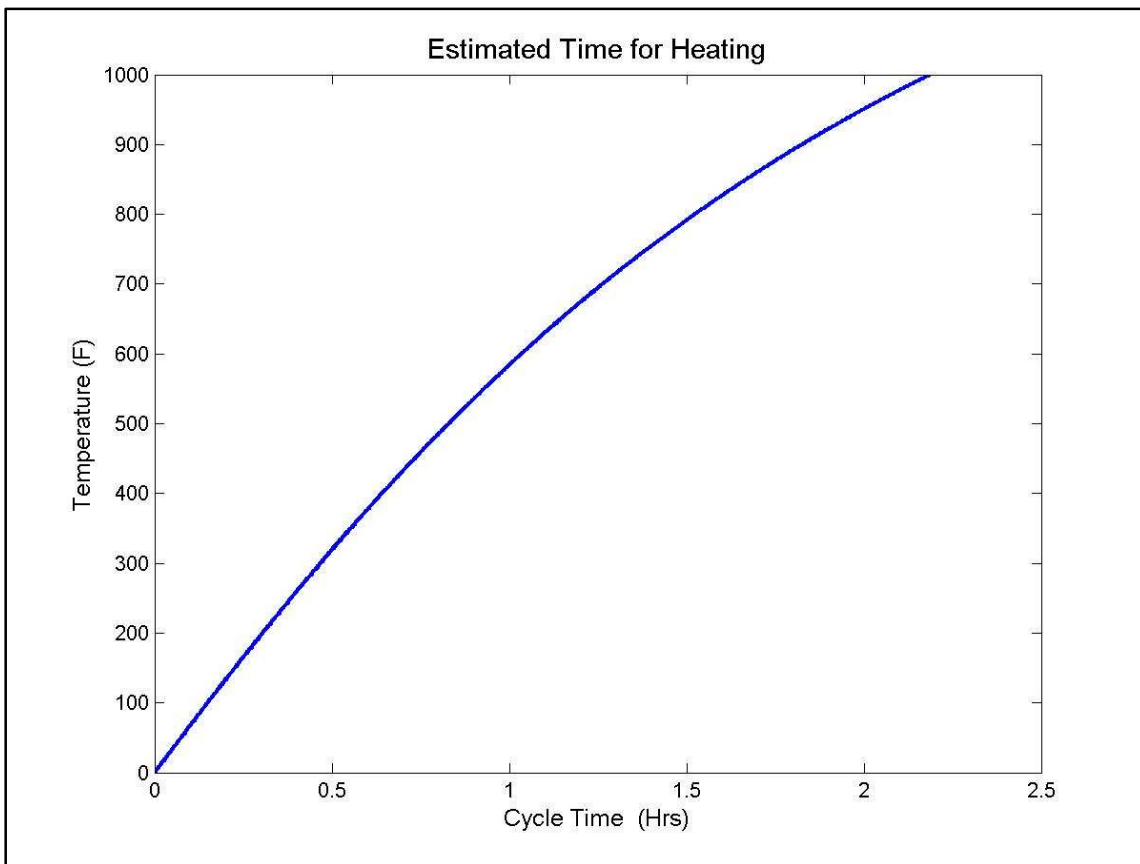


Figure 5-33 Estimated time taken to heat the system using only band heaters

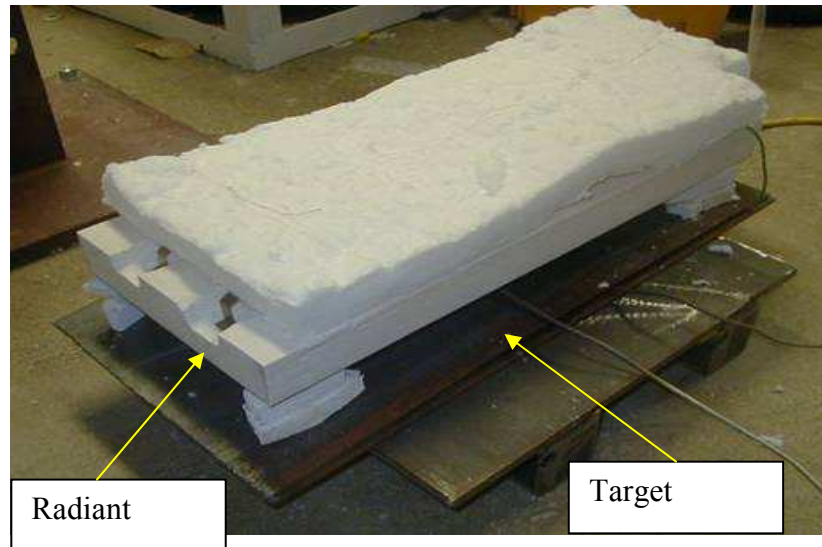


Figure 5-34 Radiant heater test

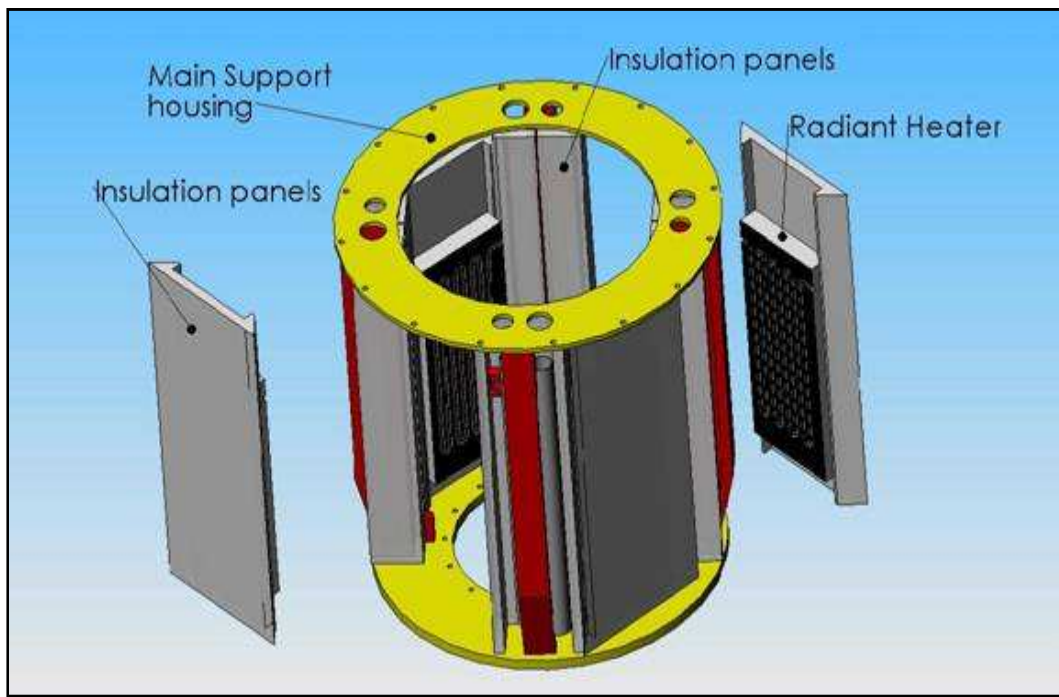


Figure 5-35 Model of the radiant heating setup

5.7 Principle of Fault Tolerant Control

The magnetic bearings used here are novel in nature because of the fact that they are Fault Tolerant, Permanent Magnet Biased, Homopolar magnetic bearings. This subsection talks about how what is fault tolerance and how it is achieved.

The aim is to achieve magnetic suspension that improves reliability via fault tolerant control (FTC). This is done using the concept of *Flux coupling* between poles of a homopolar magnetic bearing, where the coil current of one pole can drive flux through other poles [15]. FTC is used deliver desired forces even after termination of coil currents to a subset of “failed poles.” The use of fault tolerant control in active magnetic bearings is of great importance because of the high speeds involved in rotating machinery using magnetic suspension. Hence, fault tolerance is necessary to provide for stable continued operation of magnetic bearing in case of sudden failure of a coil or a power amplifier [15].

FTC is achieved using Current Distribution Matrices (CDM) which adjusts the currents and fluxes following a pole set failure. Fault tolerant approach causes a decrease in the load capacity as it redistributes the magnetic fluxes to compensate for the failed poles [15].

The EEC Universal test rig will employ a similar fault tolerant approach to control the magnetic bearings. Models have been derived for similar work performed by Li [15] and Na [16]. The EEC permanent magnet biased homopolar radial bearing consists of 6 independent pole pairs. The 6 currents in these poles are determined from 2 independent x and y control voltages. CDM matrices are required to determine the 6 currents from

the 2 voltages. The CDM's have been determined for the radial bearings. The CDM's correspond to a no-pole-failed and six different one-pole-failed states.

5.7.1 Decoupling choke design

Figure 5-36 depicts the HTRMB along with a decoupling choke. As with all fault tolerant (redundant) magnetic bearings a decoupling choke must be added into the circuit to prevent instability. The decoupling choke is used to eliminate mutual inductances and ensure that the inductance matrix is non-singular, which insures electric circuit stability.

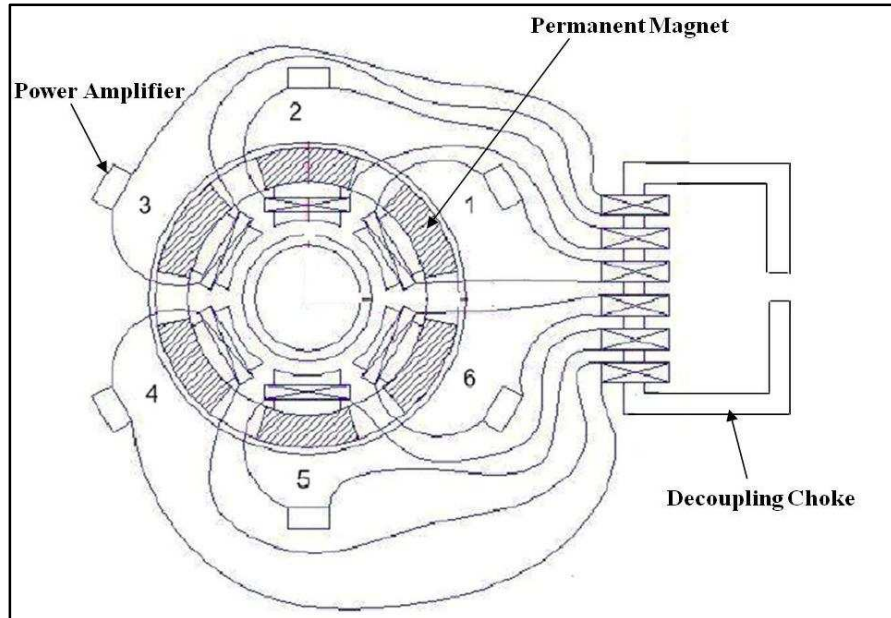


Figure 5-36 Radial bearing and decoupling choke

The inductance matrix of the isolated radial bearing is singular because flux conservation introduces a dependency relation between the fluxes. This produces a

potentially unstable operation state for the power amplifiers. By adjusting the parameters of the decoupling choke the inductance matrix becomes full rank and the mutual inductances become zero. Hence a single decoupling choke is added to the radial bearing.

5.7.2 Prediction of self inductance

After adjusting the parameters of the decoupling choke the full rank inductance matrix of the radial bearing is given below:

$$Lc = \begin{bmatrix} \frac{2 \times n^2}{R} & 0 & 0 & 0 & 0 & 0 \\ 0 & \frac{2 \times n^2}{R} & 0 & 0 & 0 & 0 \\ 0 & 0 & \frac{2 \times n^2}{R} & 0 & 0 & 0 \\ 0 & 0 & 0 & \frac{2 \times n^2}{R} & 0 & 0 \\ 0 & 0 & 0 & 0 & \frac{2 \times n^2}{R} & 0 \\ 0 & 0 & 0 & 0 & 0 & \frac{2 \times n^2}{R} \end{bmatrix}$$

Where,

- n = Number of turns of the coil on the Radial Bearing (36)
- R = Reluctance of the air gap given by:

$$R = \frac{go}{\mu_0 \times Ao}$$

- go = Air gap of the bearing (m^2)
- μ_0 = Permeability ($4\pi \times 10^7 H/m$)

- $Ao = \text{Area of the pole on the bearing (m}^2\text{)}$

For a perfectly centered shaft the air gap is designed to be 20 mil (0.000508 m) and the area of the pole is 1.764 in² (0.001138 m²). Using these parameters the inductance matrix for the magnetic bearing is equal to:

$$Lc = \begin{bmatrix} 7.29 & 0 & 0 & 0 & 0 & 0 \\ 0 & 7.29 & 0 & 0 & 0 & 0 \\ 0 & 0 & 7.29 & 0 & 0 & 0 \\ 0 & 0 & 0 & 7.29 & 0 & 0 \\ 0 & 0 & 0 & 0 & 7.29 & 0 \\ 0 & 0 & 0 & 0 & 0 & 7.29 \end{bmatrix} \text{ mH}$$

5.7.3 Testing of self and mutual inductance

A simple electrical model of the bearing is used to measure the inductances. Figure 5-37 shows the model of the bearing coils whose inductances are to be measured.

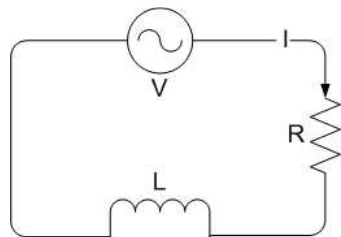


Figure 5-37 Equivalent electrical circuit of the bearing coils

By Ampere's law the voltage in the above shown circuit is given by:

$$V = L \times \frac{di}{dt} + i \times R$$

The same equation in phasor form is:

$$\tilde{V} = jL\tilde{\omega} + \tilde{R}$$

$$\frac{\tilde{V}}{\tilde{\omega}} = jL\omega + R$$

Taking the magnitude of the above equation:

$$\left| \frac{\tilde{V}}{\tilde{\omega}} \right| = \sqrt{R^2 + (\omega L)^2}$$

$$\log_{\omega \rightarrow 0} \left| \frac{\tilde{V}}{\tilde{\omega}} \right| = R$$

$$\log_{\omega \rightarrow \infty} \left| \frac{\tilde{V}}{\tilde{\omega}} \right| = L\omega$$

The equation above will give a plot similar to the one shown below in Figure 5-38. The slope of the line, when the frequency of the signal approaches infinity will yield the Inductance.

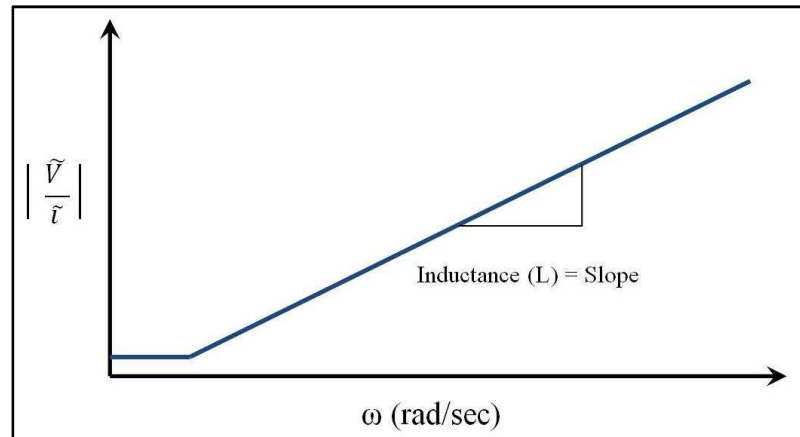


Figure 5-38 Expected output plot to determine the inductance

The experimental setup uses a function generator to provide a sinusoidal signal as input to the coils. A spectrum analyzer is used to plot the magnitude of voltage and currents in the coil. To measure mutual inductance of a particular coil the voltage across it is fed to the spectrum analyzer, while the function generator supplies the inducting coil. Figure 5-39 shows the schematic diagram of the experimental setup used to measure the inductance of the coils. Figure 5-40 and Figure 5-41 show the test setup and the decoupling choke.

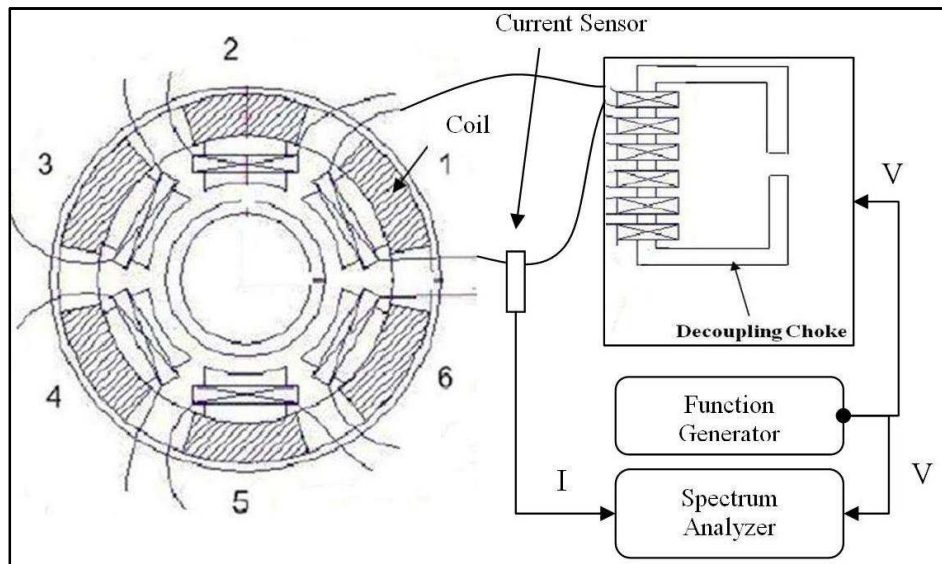


Figure 5-39 Schematic diagram of the experimental setup

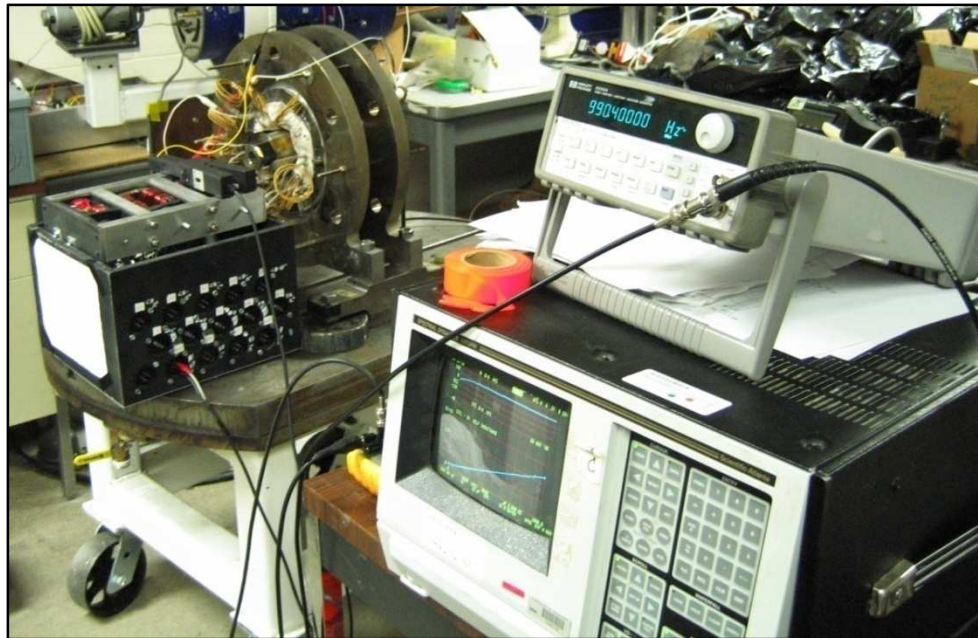


Figure 5-40 Test Setup to measure the inductance

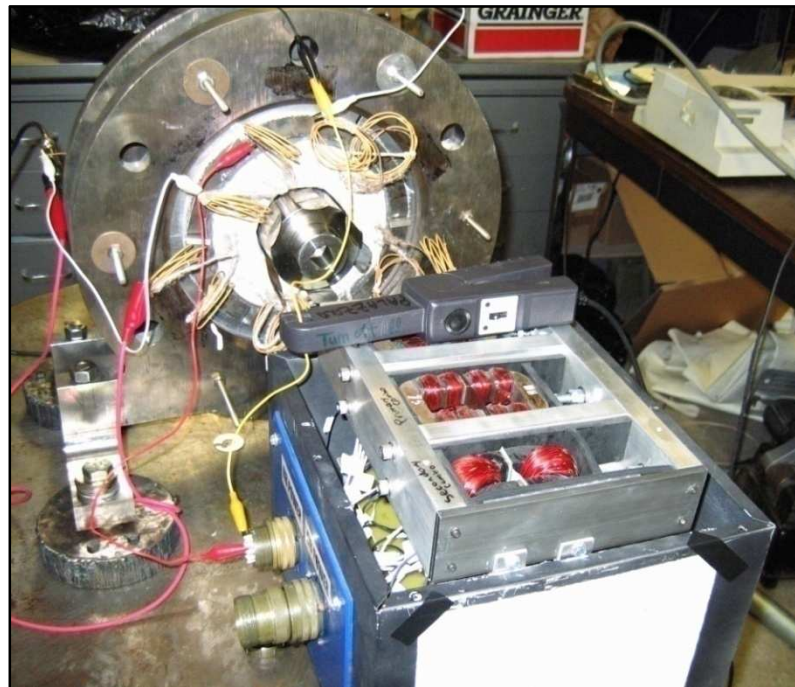


Figure 5-41 Decoupling choke along with the radial bearing

The mutual inductances are obtained with one coil supplied the voltage and the induced current measured in the other coils. Two sets of coils are taken to verify repeatability. Figure 5-42, Figure 5-43, Figure 5-44, Figure 5-45, Figure 5-46 and Figure 5-47 show the magnitude of V/I versus frequency plots for the two sets of measurements. Mutual inductances are calculated for coils 4, 5 and 6 due to coil 1 and coils 5, 6 and 1 due to the influence of coil 3. Due to the presence of a decoupling choke the mutual inductance of the coils should be nearing zero and hence called *decoupled*. The values in Table 5-3 show that the mutual inductance is almost zero and depends on the relative position of the activated and measured coils.

Table 5-3 Values of measured mutual inductance

Voltage applied to coil #	Inductance calculated for Coil #	Mutual Inductance (mH)
1	4	0.106
1	5	0.212
1	6	0.620
4	1	0.101
4	6	0.156
4	5	0.597

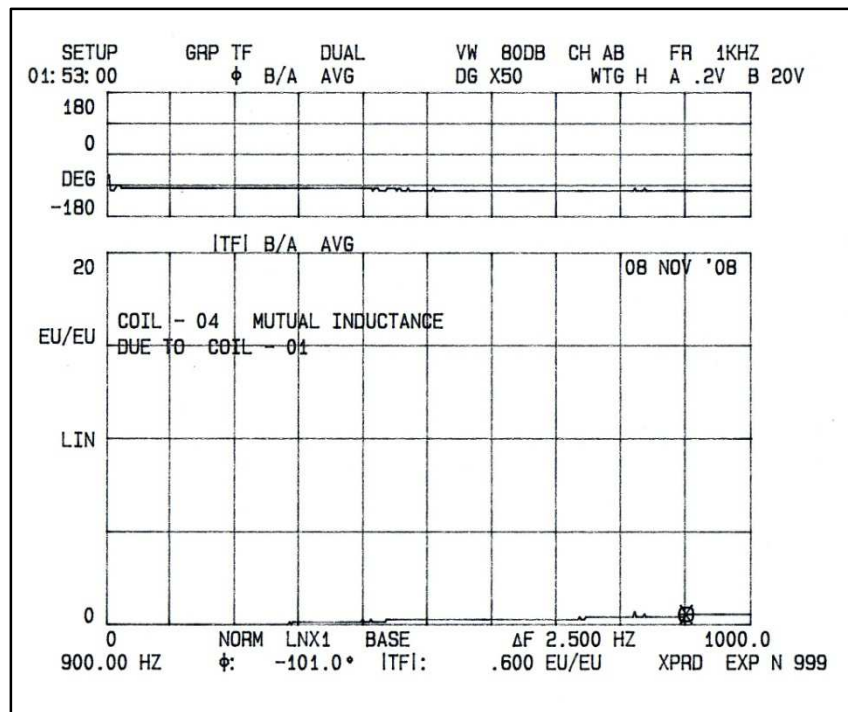


Figure 5-42 Mutual inductance in coil 4 due to coil 1

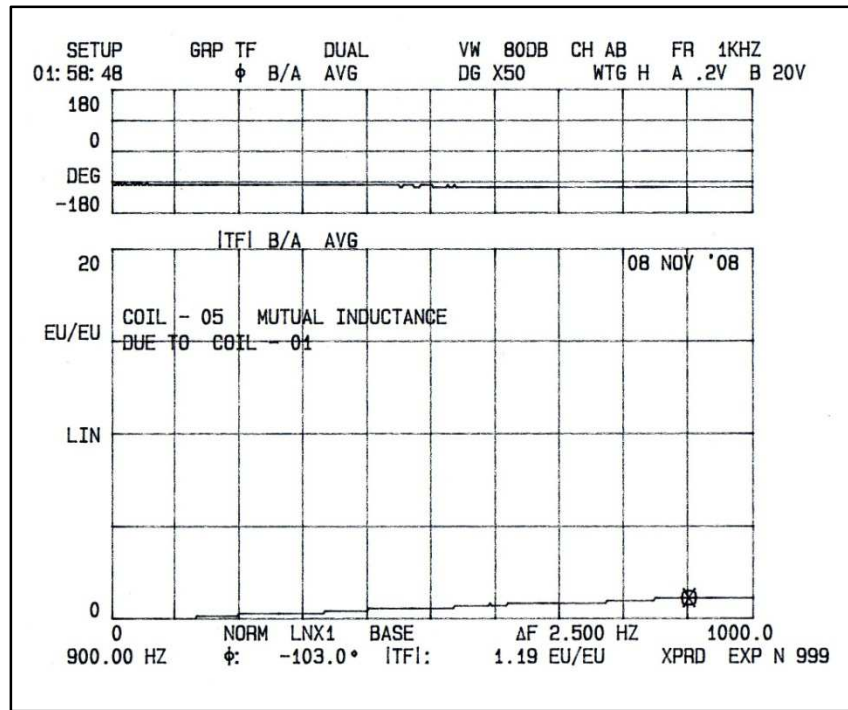


Figure 5-43 Mutual inductance in coil 5 due to coil 1

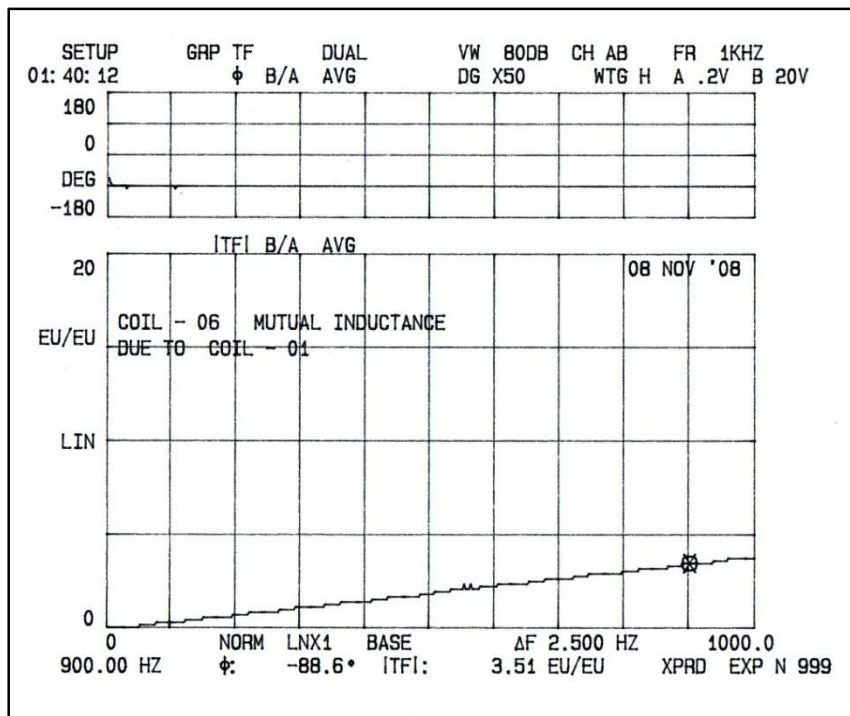


Figure 5-44 Mutual inductance in coil 6 due to coil 1

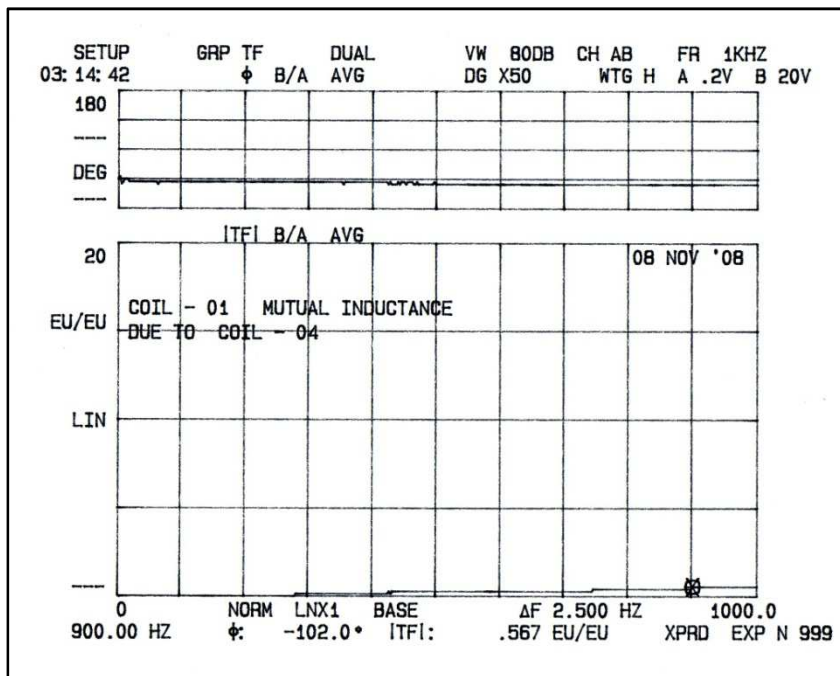


Figure 5-45 Mutual inductance in coil 1 due to coil 4

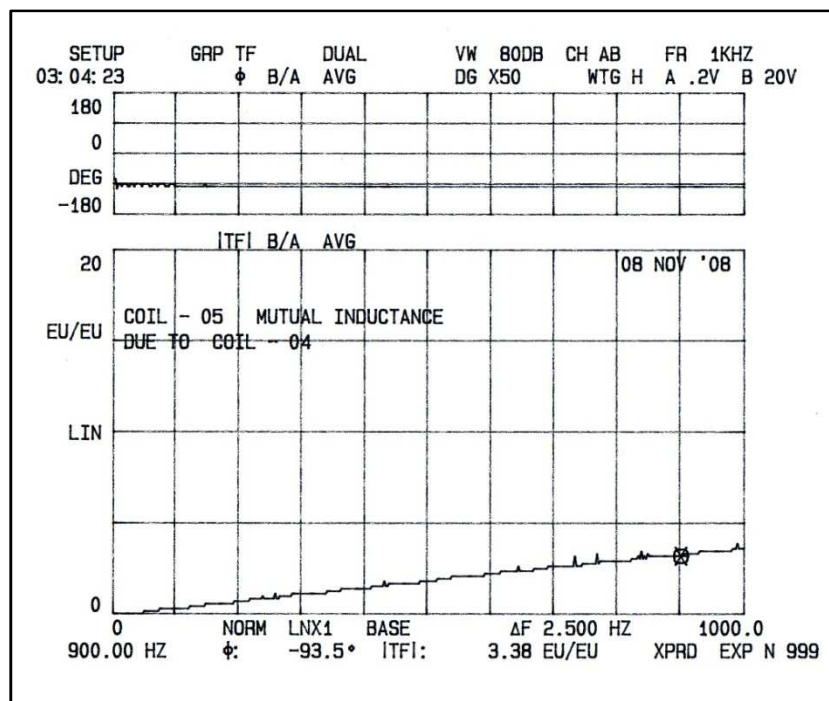


Figure 5-46 Mutual inductance in coil 5 due to coil 4

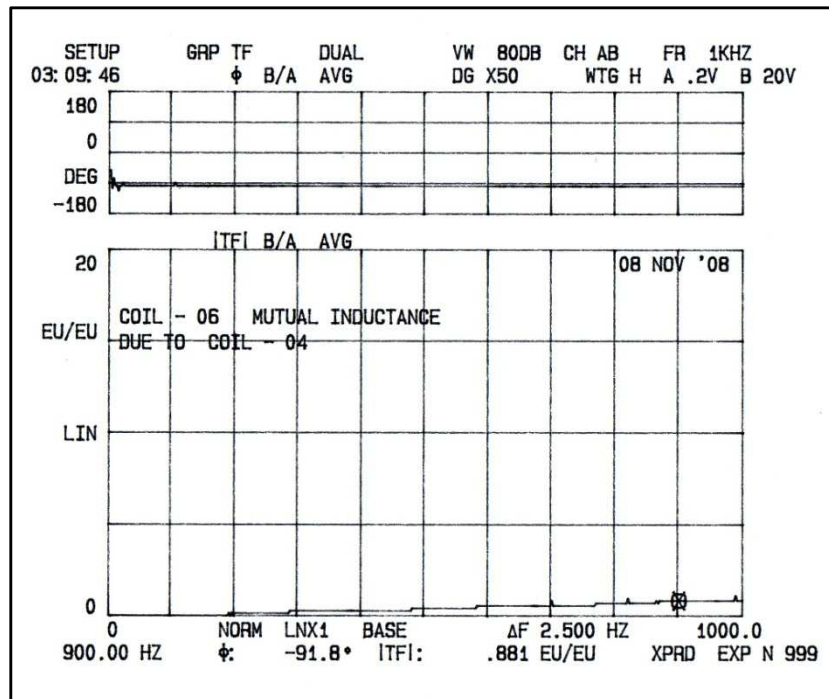


Figure 5-47 Mutual inductance in coil 6 due to coil 4

Similar to mutual inductance the self inductance can be calculated from the coils by taking the slopes of the magnitude plots. Figure 5-48, Figure 5-49, Figure 5-50, Figure 5-51, Figure 5-52 and Figure 5-53 Show the self inductance plots for coils one through six respectively. The measured values of the self inductance are shown below in Table 5-4.

Table 5-4 Values of self inductance

Pole Measured	Self Inductance (mH)
1	3.82
2	3.82
3	3.71
4	3.93
5	3.86
6	3.84

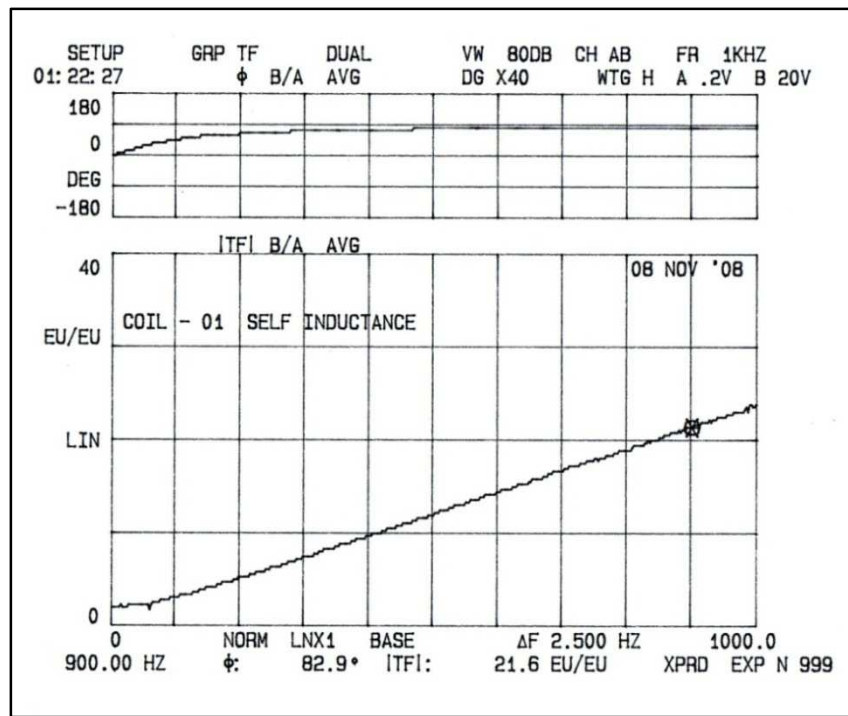


Figure 5-48 Self inductance of coil 1

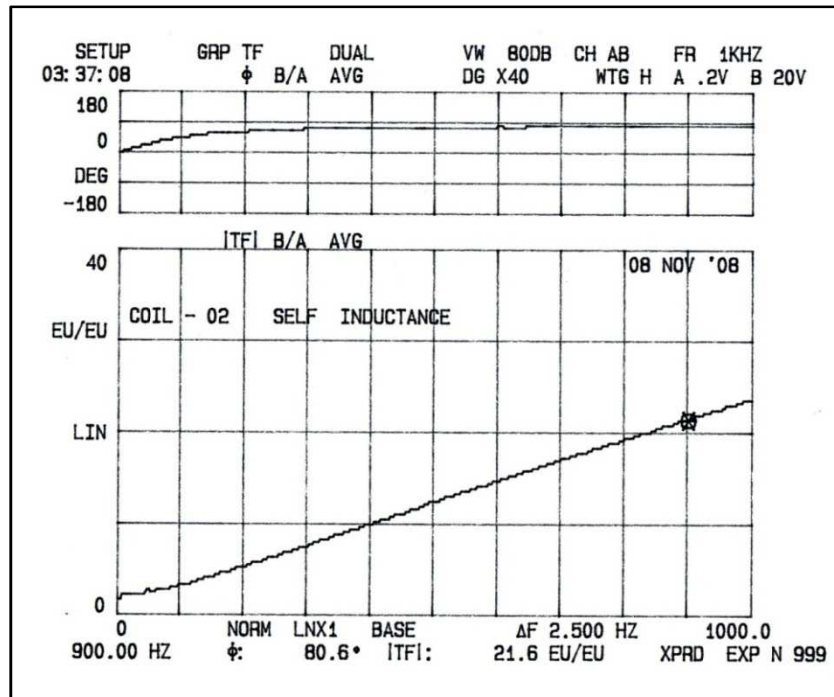


Figure 5-49 Self inductance of coil 2

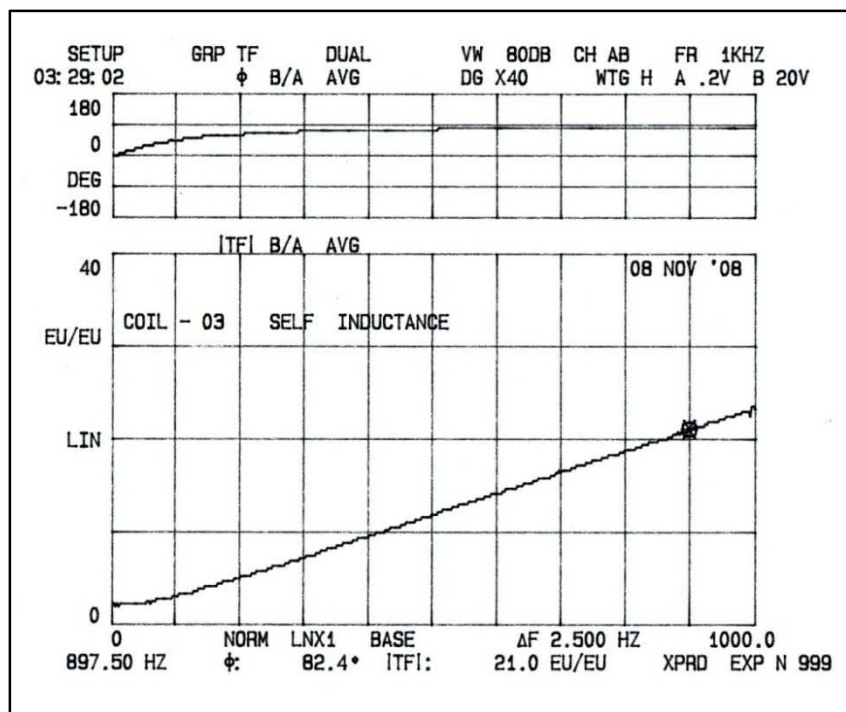


Figure 5-50 Self inductance of coil 3

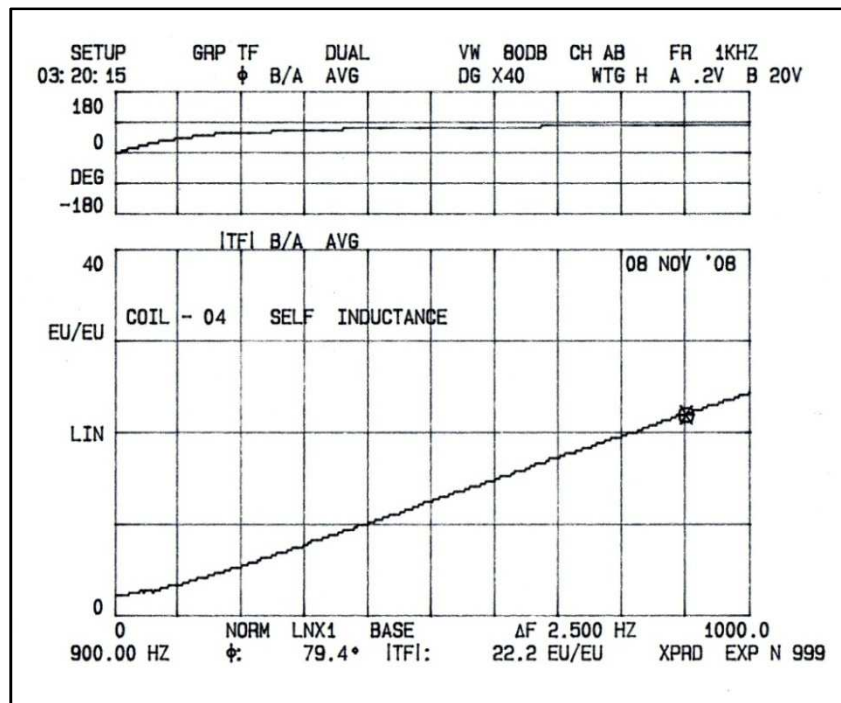


Figure 5-51 Self inductance of coil 4

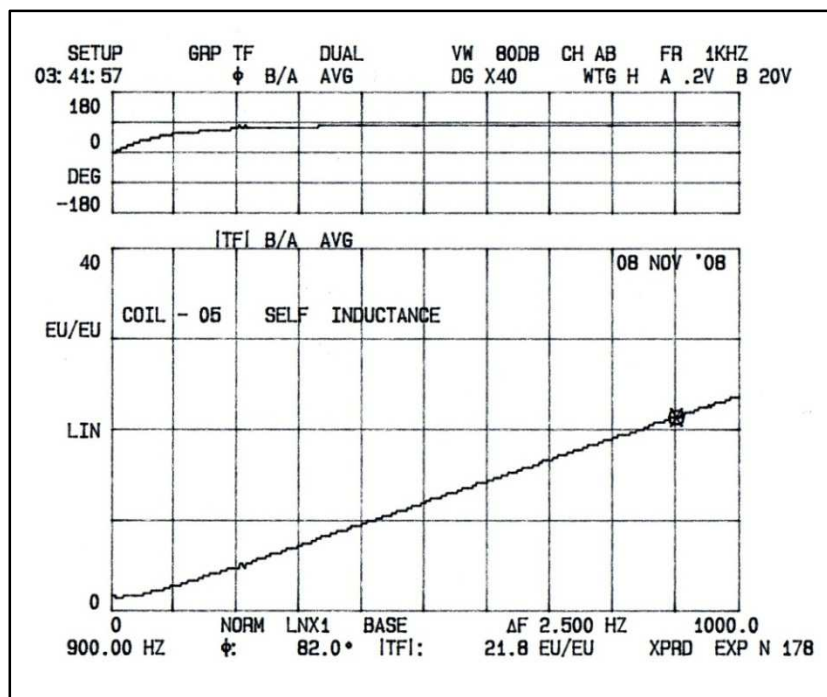


Figure 5-52 Self inductance of coil 5

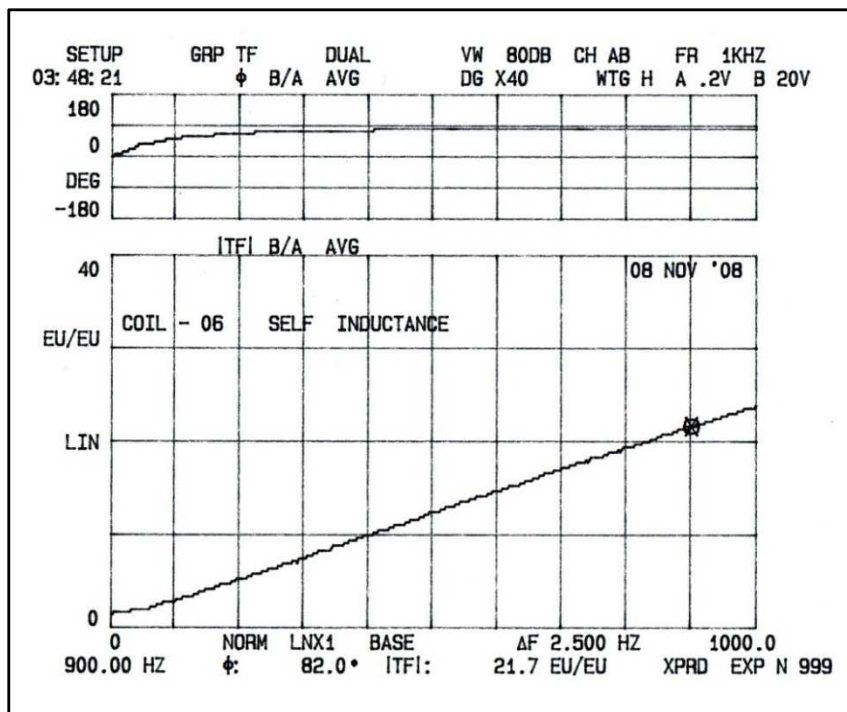


Figure 5-53 Self inductance of coil 6

The difference in the predicted values of self inductance and the actual measured values can be explained by the following two reasons:

- There is an uncertainty in the position of the shaft. The radial bearing shaft was independent of supports and the radial position may not be perfectly centered. Thus yielding different values as compared to the values measured if the shaft were to be in the perfect centre. The position of the shaft changes the air gap and hence affects the inductance value.
- The second important reason is that the prediction of the self inductance matrix does not take into account the reluctance of the path through which the flux travels. Since, for the magnetic material, $\mu_r \gg 1$, the reluctance of the magnetic material is often neglected. Although as shown in the equation below the predicted value of inductance would be smaller if the reluctance of the flux path would be considered.

$$Lc = \frac{\varphi}{Ni} = \left(\frac{2g}{\mu_0 A} + \frac{lm1}{\mu m1 A} + \frac{lm2}{\mu m2 A} \right)^{-1}$$

Where,

$lm1$ and $lm2$ are the lengths of the flux paths through the material.

$\mu m1$ and $\mu m2$ are the permeability of the materials.

6. INTEGRATION AND ASSEMBLY OF ALL COMPONENTS

The test rig is first mounted, assembled and operated on a floor mounted stand in the room as shown in Figure 6-1. The motor system will operate on slow speed and low temperature test conditions and on an assembly stand (covers, insulation, air handler lines, and cooling lines not shown in figure). The stand is mounted securely to the floor and will allow the slow speed at moderate temperature operation. For high speed operation at high temperatures the assembly will use the stand to transport the system to the spin pit. Access to Thermocouples, heaters, and displacement sensors are easily accommodated using the window ports in the outer housing.

The bearing electronics cabinet is placed in between the unit and the pit during the first phase of testing and will stay there as the rig is transferred into the pit for testing. The motor drive electronics will be housed beside the bearing electronics cabinet.

Design features have been incorporated that allow easy access to the most of the test rigs interior components. By designing the motor and bearings with larger clearances along with the methods to quickly access the interior the length of time necessary to make modifications should be reduced. The support structure is shown attached to the lid of the spin pit in Figure 6-2. This is how the motor will be operated at high temperature and speed.



Figure 6-1 Floor mounted housing

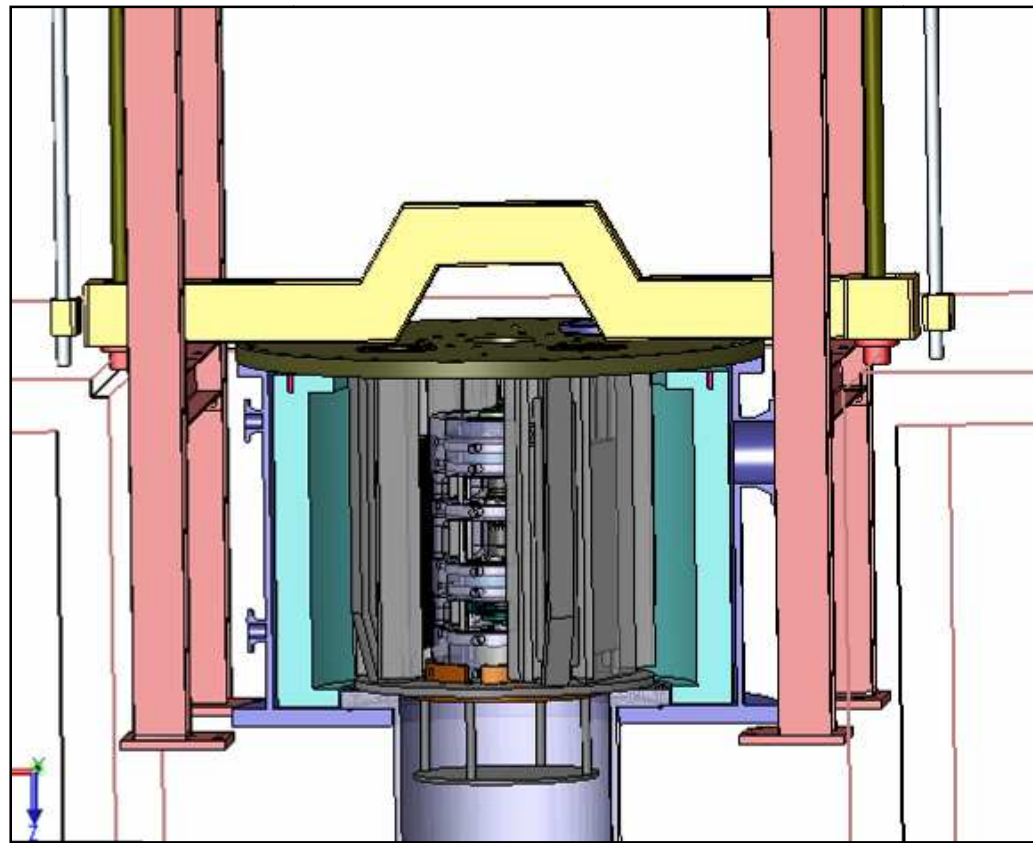


Figure 6-2 Support structure and spin pit lid

Once lowered into the spin pit the support structure occupies most of the available space. This will give us the ability to add soft supports and have a range of support stiffness's that can be used during balancing for vibration control. A small steady stream of air will be circulated while the hot system is operated this will remove explosive gasses that might normally accumulate. The spin pit's oversize vent line will prevent a potential hazard in case of an ignition of gasses causes a gas release. These gasses would be routed outside using the hot air handling system. The nitrogen system for the catcher bearings and for fire control will be used for emergencies. All of the

components below the lid will be installed with detail to prevent gassing that could be a fire hazard.

The high temperature bearing test rig and housing is shown in Figure 6-3. Sensors are to be mounted on the outside of the support housing. This will allow much easier access to make needed adjustments. The cables that exit the housing will be protected from the radiant heaters by heat shields. The ports are going to be covered at the high temperature operation and the radiant heaters will provide the extra heat necessary to assure the cavity will all reach steady state temperatures within a reasonable time as explained in the earlier section.

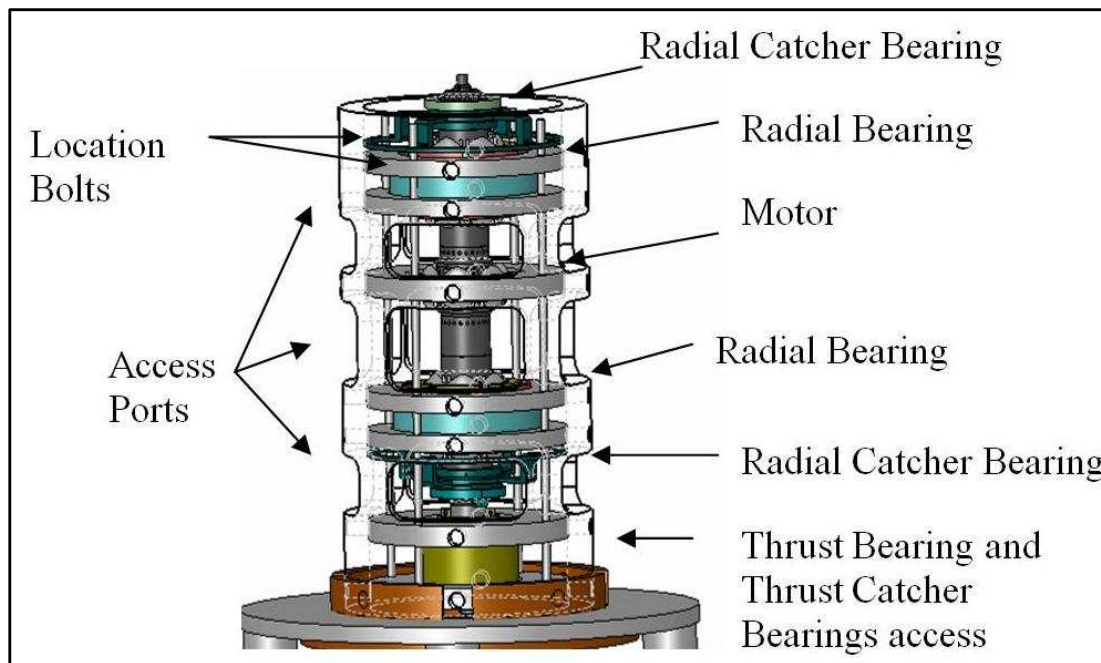


Figure 6-3 Motor system components

6.1 Assembly of Motor-Bearing System

The Motor-Bearing system will be assembled in four parts. Namely, the 2 radial bearings along with their shafts, the axial thrust bearing with its shaft and the high temperature motor with its shaft. These 4 subsystems will be coupled together using the interference fits explained earlier. Figure 6-4 and Figure 6-5 show the solid models of the full motor system.

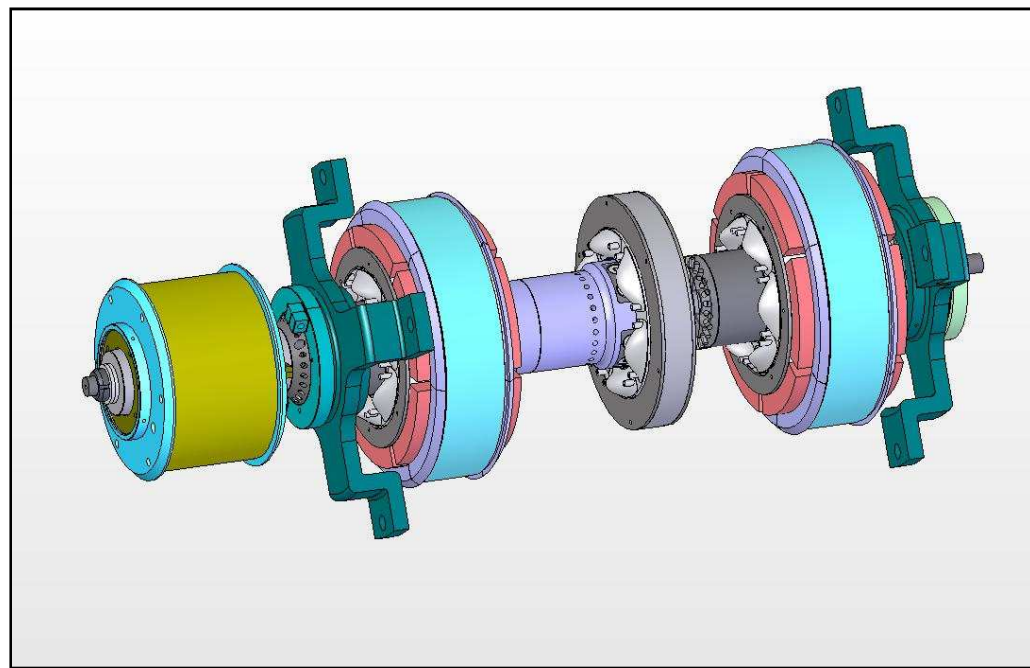


Figure 6-4 Full motor system

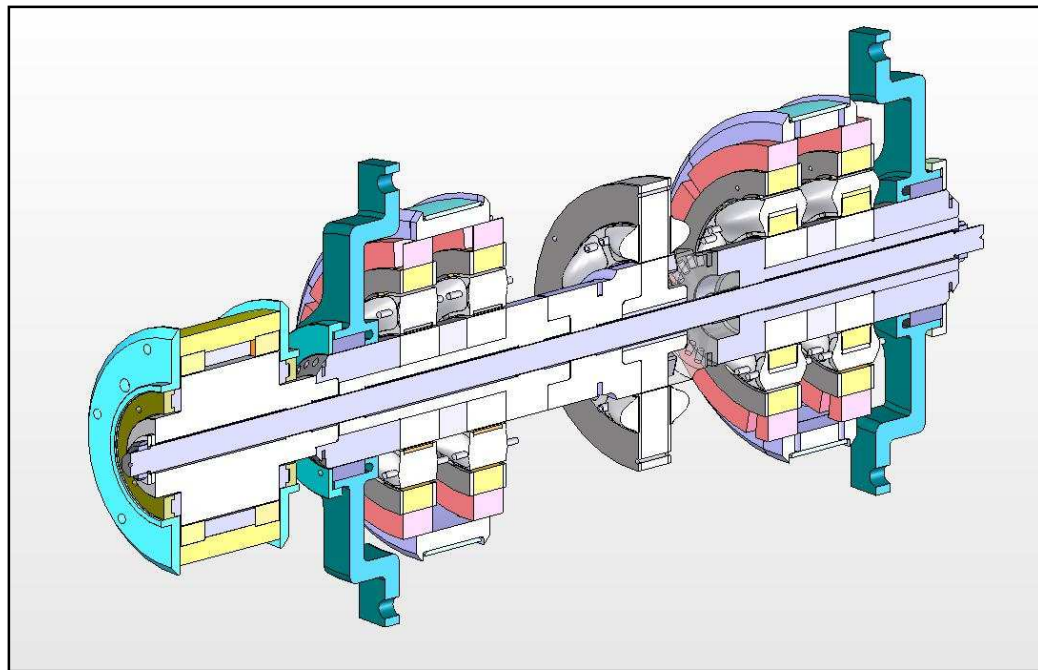


Figure 6-5 Section of motor system

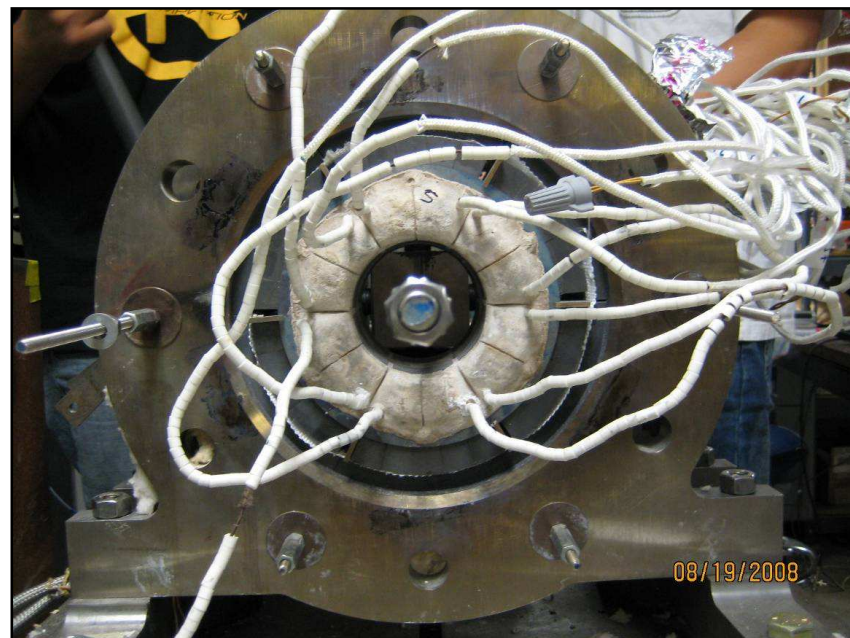


Figure 6-6 Side view radial bearing subsystem



Figure 6-7 Radial bearing subsystem

Figure 6-6 and Figure 6-7 show the radial bearing subcomponent just after its shaft was inserted. The heater system assembly is as shown below. The Figure 6-8 and Figure 6-9 show the band heaters and the main heater controller. The heater controller consists of the Watlow CLS-216 controller and a number of solid state relays to provide for the switching control of the band and radiant heaters.



Figure 6-8 Band heater mounted on the outer cylinder



Figure 6-9 Heater controller cabinet and the controller (inset)

The insulation to cover the entire test rig is made up of Zircar Alumina-Silica type ceramic (ECO-1200A). The system with the parts of the insulation panels and the radiant heaters can be seen in Figure 6-10.



Figure 6-10 Zircar insulation and radiant heaters mounted

7. CONCLUSION AND FUTURE WORK

The objective of this thesis was to test a new and improved design of a permanent magnet biased homopolar radial magnetic bearing that will operate reliably under the conditions set by the EEC sponsors, namely:

- Operating temperature of 1000°F
- 500 lb-f capacity of radial load

The simulations, design and tests that had been employed to answer this question included the following:

- 3-D magnetic field analysis. (conducted by Dr. A. Kenny)
- A test rig design and fabrication
- An experimental procedure was developed to test the load capacity and the position stiffness of the radial bearing.
- The testing also provided vital information about the behavior of the HT magnets and coils at room temperature and high temperatures.
- The test rig was capable to measure the actual load capacity of the bearing to near design values.

There were no formal tests conducted to check for repeatability. However, during the testing process a number of heating cycles were carried out and the test values were taken at each time. The forces measured during each test matched up very closely.

EEC also called for a Universal test rig system that utilizes Permanent magnet biased axial and radial bearings and a PM biased motor to operate as a unit in the test

system under the conditions of high temperature and speed. As explained in sections 5 and 6, various design considerations were made, tested and a finalized. The Universal test rig is almost finished and awaits assembly of the 4 main subsystems as mentioned earlier.

7.1 Future Work

The future work involves testing of the assembled radial magnetic bearing along with the other designed, manufactured and assembled components such as the motor and the thrust bearing. The shaft will be levitated in the new universal test rig. These tests will provide more vital data with the actual conditions of application closely simulated.

The testing process would involve:

- Developing the motor and magnetic bearing controllers.
- Levitating the shaft using the bearing system and the controllers.
- Rotating the shaft at room temperature at low speeds (~2000 rpm).
- Rotating the Shaft at similar speeds and at temperatures going up to 1000°F.
- Lowering the test rig into the spin pit system to test at higher speeds (~15000rpm).
- Life cycle testing of these bearings at high temperatures.
- Seeking opportunities to utilize this technology in industrial application.

REFERENCES

- [1] Mohiuddin, M., 2002, "Design of High Temperature High Speed Electromagnetic Axial Thrust Bearing," Master's Thesis, Texas A&M University, Department of Mechanical Engineering, College Station.
- [2] Hossain, M., 2006. "High Temperature, Permanent Magnet Biased, Homopolar Magnetic Bearing Actuator" Master's Thesis, Texas A&M University, Department of Mechanical Engineering, College Station.
- [3] Provenza, A., Montague, G., Jansen, M., Palazzolo, A. and Jansen, R., 2005, "High Temperature Characterization of a Radial Magnetic Nearing for Turbomachinery," Journal of Engineering for Gas Turbines and Power, **127**, pp.437-444.
- [4] Bornstein, K. R., 1990, "Dynamic Load Capabilities of Active Electromagnetic Bearings," Journal of Tribology, **90**-Trib-50, pp. 1-6.
- [5] Schweitzer, G., Bleuler, H. and Traxler, A., 1994, "Basics, Properties and Applications of Active Magnetic Bearings," Active Magnetic Bearings, **210**, pp. 1-112.
- [6] DeWeese, R.T., 1996, "A Comparison of Eddy Current Effects in a Single Sided Magnetic Thrust Bearing," Master's Thesis, Department of Mechanical Engineering, Texas A&M University, College Station.
- [7] Polajzer, B, 2003, "Design and Analysis of an Active Magnetic Bearing Experimental System", Ph. D. Dissertation, Department of Electrical Engineering and Computer Science, University of Maribor, Slovenia.

- [8] Meeks, C. R., DiRusso, E., and Brown, G. V., 1990, "Development of a Compact, Light Weight Magnetic Bearing," *Proc. of the 26th Joint Propulsion Conference* AIAA/SAE/ASME/ASEE, Orlando, pp. 3420 – 3427.
- [9] Sortore, C. K., Allaire, P. E., Maslen, E. H., Humphris, R. R., and Studer, P. A., 1990, "Permanent Magnetic Biased Bearings—Design, Construction, and Testing," *Proc. of the Second International Symposium on Magnetic Bearings*, Tokyo, pp. 175–182.
- [10] Lee, A., Hsio, F., and Ko, D., 1994, "Analysis and Testing of Magnetic Bearing With Permanent Magnets for Bias," *JSME Int. J., Ser. C*, **37**, pp. 774-782.
- [11] Imlach, J., Blair, B. J., and Allaire, P. E., 1990, "Measured and Predicted Force and Stiffness Characteristics of Industrial Magnetic Bearings," *Joint ASME/STLE Tribology Conference*, Toronto, **90-Trib-70**. 56.
- [12] Fittro, R. L., Baun, D. O., Maslen, E. H., and Allaire, P. E., 1997, "Calibration of an 8-Pole Planar Radial Magnetic Actuator," *Proc. of the 1997 International Gas Turbine & Aeroengine Congress & Exposition*, Orlando, 97-GT-18.
- [13] Kenny, A., Palazzolo, A., 2003, "Single Plane Radial, Magnetic Bearings Biased With Poles Containing Permanent Magnets," *Transactions of the ASME*, **125**, pp. 178-185.
- [14] Watlow's online heating solution manuals, www.watlow.com and <http://www.watlow.com/literature/catalogs/files/appguide.pdf>, accessed on 11/15/2008, pp. 15-18.

- [15] Li, M., 2004, "Fault Tolerant Control of Homopolar Magnetic Bearings and Circular Sensor Arrays", Ph.D Dissertation, Department of Mechanical Engineering, Texas A&M University, College Station.
- [16] Na, U., 1999, "Fault Tolerant Control of Heteropolar Magnetic Bearings", Ph.D Dissertation, Department of Mechanical Engineering, Texas A&M University, College Station.

Supplementary Sources Consulted

- Allaire, P. E., Mikula, A., Banerjee, B. B., Lewis, D. W. and Imlach, J., 1988, "Design and Test of a Magnetic Thrust Bearing", *NASA Conference on Magnetic Suspension Technology*, Langley Field, pp. 831-847.
- Palazzolo, A., Tucker, R., Kenny, A., Kang, K D., Gandhi, V., Liu, J., Choi, H. and Provenza, A., 2008, "High Temperature, Permanent Magnet Biased, Fault Tolerant, Homopolar Magnetic Bearing Development," *Proceedings of ASME Turbo EXPO 2008: Power for Land, Sea and Air*, Berlin, Germany, GT2008-50917.

VITA

Varun Rajesh Gandhi was born to Jaishree and Rajesh Gandhi in India. He pursued his primary education in Baldwins, Bangalore, India followed by Bishop Cotton, Bangalore, India. He obtained his Bachelor of Engineering degree in mechanical engineering from Rashtreeya Vidyalaya College of Engineering, Bangalore, India, with a first class and distinction, in the year 2005.

Varun Rajesh Gandhi was admitted into the master's program in Fall 2006, with the Mechanical Engineering Department, Dwight Look College of Engineering at Texas A&M University. He joined the Vibration Control and Electromechanics Laboratory with Dr. Alan Palazzolo as his research advisor in the spring semester. He joined The MathWorks Inc. as a Application Support Engineer Intern in January 2008.

He pursued his research in the field of Magnetic Bearings under the guidance of Dr. Alan Palazzolo and his committee members Dr. Bryan Rasmussen and Dr. Srinivas Vadali. He received his M.S. degree in Mechanical Engineering in May 2009.

Varun's permanent address and Email ID are:

3123 TAMU,
College Station, TX 77843- 3123, USA.
varunrgandhi@gmail.com